





Universitat Autònoma de Barcelona

ADVERTIMENT. L'accés als continguts d'aquesta tesi queda condicionat a l'acceptació de les condicions d'ús establertes per la següent llicència Creative Commons:  http://cat.creativecommons.org/?page_id=184

ADVERTENCIA. El acceso a los contenidos de esta tesis queda condicionado a la aceptación de las condiciones de uso establecidas por la siguiente licencia Creative Commons:  <http://es.creativecommons.org/blog/licencias/>

WARNING. The access to the contents of this doctoral thesis it is limited to the acceptance of the use conditions set by the following Creative Commons license:  <https://creativecommons.org/licenses/?lang=en>



**Molecular Details of Prostaglandin Synthesis
Catalyzed by Cyclooxygenase-2 and Its Inhibition
by Aspirin.**

Anna Cebrián Prats

PhD program in Chemistry

Supervisors:

José Maria Lluch López

Àngels González Lafont

DEPARTAMENT DE QUÍMICA
FACULTAD DE CIÈNCIAS

2020

This is an article-based PhD Thesis. This dissertation is composed of a short overview of the work, followed by a copy of the papers already published.

*“But nature is always more subtle, more intricate,
more elegant than what we are able to imagine.”*

Carl Sagan

II	Theoretical Background	29
2	Computational Methods	31
2.1	Molecular Mechanics	32
2.1.1	Mathematical expression: Forcefield	32
2.2	Quantum Mechanics	35
2.2.1	Time-independent Schrödinger Equation	35
2.2.2	Density Functional Theory	37
2.2.2.1	Kohn-Sham Method	39
2.2.2.2	Hybrid Exchange Functional	41
2.3	Hybrid QM/MM Method	42
2.3.1	QM/MM energy expression	43
2.3.1.1	Subtractive QM/MM scheme	44
2.3.1.2	Additive QM/MM scheme	45
2.3.2	QM-MM Boundary schemes	48
2.4	Chemshell Software	51
2.4.1	QM/MM Methodology	51
2.4.2	Geometry Optimization	52
2.5	Gaussian's ONIOM method	53
2.5.1	QM/MM Methodology	54
2.5.2	Geometry Optimization	56
2.6	Molecular Dynamics Simulations	57
2.6.1	MD algorithm	58
2.6.2	Protocol for the MD simulations	59
2.6.3	Periodic Boundary Conditions	60
III	Results and Discussion	61
3	COX-2:AA	63
3.1	Insight into the all-radical mechanism	64
3.2	Carbocation-Based Mechanism	70
3.3	Gly526Ser Mutation	71
3.4	Molecular Details of the Inhibition by Aspirin	74
	Appendices	81

A Radical Mechanism from HproS	83
A.1 QM/MM calculations	83
4 COX-2:EPA	89
4.1 Introduction	89
4.2 Methodology	92
4.3 Results and Discussion	93
IV General Conclusions	107
5 General Conclusions	109
Bibliography	113
Article I	137
Article II	159
Article III	185

List of Acronyms

EFAs	Essential Fatty Acids
PUFAs	Polyunsaturated Fatty Acids
FAs	Fatty Acids
SC-PUFAs	Short-Chain Polyunsaturated Fatty Acids
LC-PUFAs	Long-Chain Polyunsaturated Fatty Acids
ALA	α -linolenic acid
LA	Linoleic acid
AA	Arachidonic Acid
EPA	Eicosapentaenoic Acid
DHA	Docosahexaenoic Acid
ω_6	Omega-6
ω_3	Omega-3
PGHS	Prostaglandin Endoperoxide H Synthase
COXs	Cyclooxygenases
COX-2	Cyclooxygenase 2
COX-1	Cyclooxygenase 1
PGs	Prostaglandins
TXs	Thromboxanes
LOXs	Lipoxygenases
cPLA₂	cytosolic Phospholipase A ₂
EGF	Epidermal Growth Factor

MBD	Membrane Binding Domain
COX active site	Cyclooxygenase active site
POX active site	Peroxidase active site
PGH₂	Prostaglandin H ₂
PGG₂	Prostaglandin G ₂
NSAIDs	Nonsteroidal Anti-Inflammatory Drugs
ASA	Acetylsalicylic Acid
EPR	Electron paramagnetic resonance
HETE	Hydroxyeicosatetraenoic acid
HpETE	Hydroperoxy-eicosatetraenoic acid
G526S	Gly526Ser
IsoP	Isoprostane
RP-HPLC	Reverse phase High performance liquid chromatography
SP-HPLC	Straight-phase High performance liquid chromatography
FF	Forcefield
QM	Quantum Mechanics
MM	Molecular Mechanics
QM/MM	Quantum-Mechanics/Molecular-Mechanics
ONIOM	Our own N-layered Integrated molecular Orbital and molecular Mechanics
PES	Potential Energy Surface

MD	Molecular Dynamics
DFT	Density Functional Theory
HF	Hartree-Fock
ME	Mechanical Embedding
EE	Electrostatic Embedding
RMSD	Root Mean-Square Deviation
Antara	Antarafacial
Supra	Suprafacial
R	Reactant
TS	Transition State
P	Product
SPMs	Specialized Pro-resolving Mediators
LTA₄H	LTA ₄ hydrolase
RvE1	Resolvin E1
RvE2	Resolvin E2
HEPE	Hydroxyeicosapentaenoic acid
HpEPE	Hydroperoxy-eicosapentaenoic acid
pEPE	peroxy-eicosapentaenoic acid

Part I

Introduction

Chapter 1

Introduction

1.1 Biological Overview

Cyclooxygenase-2 (COX-2) is a membrane-associated homodimeric bi-functional hemoprotein enzyme that catalyzes the oxygenation of several Polyunsaturated Fatty Acids (PUFAs).¹ COX-2 leads to the formation of the eicosanoids Prostaglandins (PGs), whose production is associated with many human pathologies, including inflammation, cardiovascular diseases and cancer.² COX-2 has crucial relevance in pharmacology because it is a target of the nonsteroidal anti-inflammatory drugs such as, for instance, aspirin, ibuprofen, and diclofenac, producing the well-known analgesic, antipyretic, and anti-inflammatory effects.³⁻⁸

Before I proceed with the introduction of COX-2 enzyme, I would like to begin by introducing the biological background that surrounds its biosynthesis. In the first section a brief overview of Polyunsaturated Fatty acids and the relation of eicosanoids to inflammatory processes are expounded. Thereafter, the Prostaglandin Endoperoxide H Synthase (PGHS) enzyme is introduced and later its catalytic reaction is described in detail. Finally, in the last sections an specific mutation and the anti-inflammatory path catalyzed by aspirin are introduced to give a complete overview of the purpose of this thesis.

1.1.1 Polyunsaturated Fatty Acids (PUFAs)

Essential Fatty Acids (EFAs) are essential fats that our body cannot synthesize. It only has access to them via our diverse diet. At the beginning of '30s EFAs have been discovered by Burr and Burr research on rats.⁹ Nevertheless, several generations of scientists¹⁰ should pass before the EFAs were considered essential metabolites for biological processes in human health and diseases. Nowadays, it is known that in human body only two EFAs, namely Short-Chain Polyunsaturated Fatty Acids (SC-PUFAs), which have 16 or 18 carbon atoms exist: α -linolenic acid (ALA) and Linoleic acid (LA). These two SC-PUFAs were considered essential metabolites because humans lack the desaturase enzymes required for their production.¹¹

However, the human body also presents other polyunsaturated fatty acids, namely Long-Chain Polyunsaturated Fatty Acids (LC-PUFAs). LA and ALA are the main precursors of the two principal families of LC-PUFAs, called the Omega-6 (ω_6) and the Omega-3 (ω_3), respectively. These two families are also considered essential fatty acids, which have more than 18 carbon atoms, such as Arachidonic Acid (AA, ω_6), Eicosapentaenoic Acid (EPA, ω_3), Docosahexaenoic Acid (DHA, ω_3) etc. Fortunately, either the ω_3 or ω_6 LC-PUFAs can also be acquired¹² by food intake. Omega-3 fatty acids can be found¹³ in fish such salmon and tuna, algae and fish oil, whereas Omega-6 can be found¹² in red meat and chicken.

PUFAs are named unsaturated for their double bonds in their hydrocarbon chain. The hydrocarbon chain has a carboxyl group (-COOH) at the beginning and a methyl group (-CH₃) at the end. Since PUFAs can present different lengths, the last position is labelled as ' ω ', and a lipid number [X:Y] describes the total number of carbon atoms, X, and the total number of double bonds, Y, in the hydrocarbon chain (Fig.1.1). Moreover, the nomenclature refers to fatty acids as ω_Z , in which Z indicates the total number of carbon atoms before the first double bond from the methyl group (Fig.1.1). Then, the fatty acids ω_3 or ω_6 refer to all PUFAs that present 3 or 6 carbon atoms, respectively, before the first double bond from the methyl group.

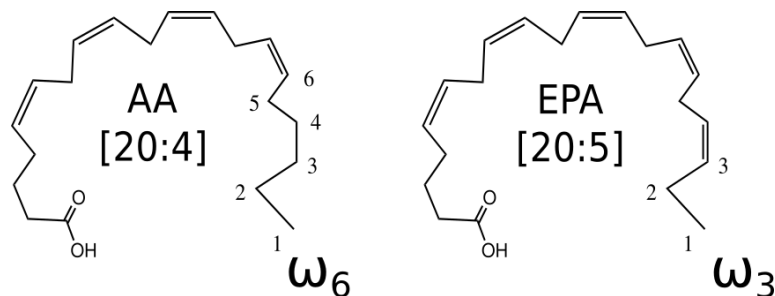


Figure 1.1: The Figure represents the LC-PUFAs named Arachidonic Acid (AA, ω_6), and Eicosapentanoic Acid (EPA, ω_3). The lipid number associated to each FA is [20:4] and [20:5] for AA and EPA, respectively. This labeling is for the sake to understand the origin of the omega nomenclature.

1.1.2 Eicosanoids

It is well-known that PUFAs serve as precursors for the most important classes of lipid mediators, the Eicosanoids family, involved not only into inflammatory processes but also in the biosynthesis of anti-inflammatory lipid mediators.^{14, 15} The eicosanoid family is constituted by a group of bioactive lipids that are generated through specific biosynthetic pathways. Eicosanoids encompass the subfamilies of leukotrienes, prostanoids, lipoxins and resolvins which are lipid signalling molecules formed by the enzymatic oxidation of ω_6 or ω_3 fatty acids.

If we go back in time before '60s the pro-inflammatory lipid mediators have been associated with cytokines and eicosanoids such as leukotrienes. Nevertheless, nowadays it has long been known that leukotrienes¹⁶ and prostaglandins¹⁷ govern the early events in host defence. Leukotrienes and prostaglandins are principally formed by the biosynthesis of AA through Lipoxygenases (LOXs) and Cyclooxygenases (COXs), respectively. Although both pro-inflammatory lipids participate in the inflammation process, in this thesis we will only focus on the formation of prostaglandins.

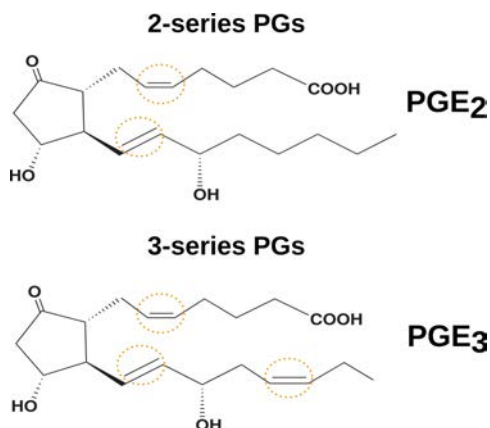


Figure 1.2: Two example of prostaglandins of 2-series on the top, and 3-series below. The cycles in orange indicate the double bond of the carbon chain, whose number determine the type of PGs series

1.1.3 Prostanoids

Prostaglandins are a subclass of eicosanoids, the prostanoids. The Prostanoids are cyclic oxygenated products of ω_6 and ω_3 PUFAs which are formed enzymatically via Prostaglandin Endoperoxide H Synthases (called COXs). Prostanoids are a family of lipid mediators involved in inflammatory response.¹⁷ Prostanoids are subdivided into three subclasses: i) prostaglandins (PGs), ii) prostacyclins and iii) thromboxanes (Tx). Each subclass presents a physiological function: *Prostaglandins* are the mediators of inflammatory reactions,¹⁸ *Prostacyclins* are effective vasodilators by the inhibition of platelet aggregation,¹⁹ and *Thromboxanes*²⁰ are vasoconstrictors and facilitate platelet aggregation.

The structures of prostaglandins were discovered by Hamberg and Samuelsson²¹ in '60s when it was also demonstrated that PGs are principally produced from an essential fatty acid, AA. PGs present a 20-/22-carbon atoms chain with a 5-member carbon ring, a hydroxyl group with the S-configuration on C₁₅, and a trans double bond at C₁₃. Prostaglandins are called using the prefix "PG" followed by a letter A to K depending on the nature and position of the substituent on the 5-member carbon ring.

Prostaglandins are classified by groups of "series" from 1 to 3 depending on the nature of the precursor fatty acid synthesized by COX of which depends the number of double bonds in PGs.²² Besides, a Greek subscript (α or β) is used especially in PGF to describe the stereochemistry of the hydroxyl group on C₉. This means that for example, the biosynthesis of PGD₂, PGE₂, PGF₂ α and PGI₂ (called 2-series PGs) is carried out by the action of COX on (AA, ω_6), and the biosynthesis of PGD₃, PGE₃, PGF₃ α and PGI₃ (called 3-series PGs) on (EPA, ω_3), see Figure 1.2.

1.1.4 Role of PUFAs into inflammatory processes

Inflammation is a biological response of body tissues caused by a tissue injury or infection. The inflammatory response is a harmful stimulus that appears to protect our body. This stimulus starts the biosynthesis cascade of eicosanoids to repair the tissue injury or eliminate the microbial invading agents. It has been known that PUFAs, in particular AA, play a crucial role in the initiation of the inflammatory response. The production of prostaglandins begins at the onset of the inflammatory response when Arachidonic Acid is released from the phospholipid membrane by cytosolic phospholipase A₂ enzyme (cPLA₂).²³ Then, Arachidonic Acid (AA) is converted to prostaglandin H₂ (PGH₂) by COX, in particular, the isoform COX-2. Thereafter, the transformation of PGH₂ by specific synthases produces prostaglandins (PGD₂, PGE₂ and PGF₂), prostacyclin (PGI₂) and thromboxane (TXA₂), see Figure 1.3.

However, if the inflammation response keeps uncontrolled it may lead to acute, chronic, and systemic inflammatory disorders. Indeed, some of the most common diseases that are difficult to treat are associated to excessive, or chronic inflammation, including the following: asthma, diabetes, rheumatoid arthritis, cardiovascular disease, as well as Alzheimer disease.^{14, 24} The common treatment involves the use of Nonsteroidal Anti-Inflammatory Drugs (NSAIDs), such as, for instance, aspirin, ibuprofen, naproxen and diclofenac, producing the well-known analgesic, antipyretic, and anti-inflammatory effects.³⁻⁸ Nevertheless, in many cases, this treatment is often not very effective.

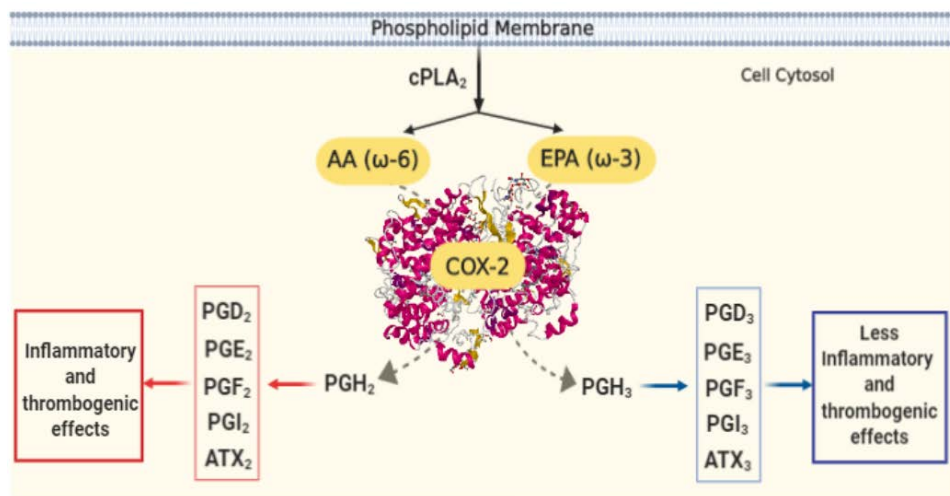


Figure 1.3: The role of Arachidonic acid (AA, ω_6) and Eicosapentaenoic acid (EPA, ω_3) into inflammatory response.

In modern western diets, ω_6 fatty acids are present in a higher ratio than ω_3 fatty acids. Unfortunately, these ratios increase the risk of cardiovascular diseases and cancer.^{12, 25} Nevertheless, the consumption of ω_3 has been shown to play a role in the prevention of many cancers in humans²⁵⁻²⁷ by reducing the pro-inflammatory lipid mediators^{14, 15}. The ω_3 diet is rich in EPA and DHA. These two ω_3 fatty acids are located and released from the phospholipid membrane by the cPLA₂, just as AA. However, as it is mentioned before, AA (ω_6) is not the only precursor of prostaglandins, EPA (ω_3) is as well. Then, EPA competes to be converted into prostaglandin H₃ by the biosynthesis of the COX-2 isoform, see Figure 1.3, to produce 3-series PGs with less inflammatory effects (PGE₃, PGF₃), thrombotic effects (TXA₃), and anti platelet aggregation (PGD₃, PGI₃).^{22, 28}

Apart from that, some recent findings by Serhan et al.¹⁴ have revealed that through the ω_3 diet new lipid mediators, such as resolvins, protectins and maresins, can act as anti-inflammatory and pro-resolving mediators of chronic inflammation. Concretely, in 2000 they observed that the resolvins derived from EPA could only be obtained by the cyclooxygenase enzyme in the presence of aspirin.²⁹

This shows that the balanced intake of ω_6 and ω_3 fatty acid is very important for the prevention of diseases with inflammatory disorders. What is more, the detailed molecular mechanism inside the COX-2 isoform, the understanding of the interaction of new drugs to inhibit inflammation, and the new alternative treatments based in the resolution of inflammation remain of great interest for scientists.

1.2 Prostaglandin Endoperoxide H Synthase

Prostaglandin Endoperoxide H Synthase (PGHS) is a membrane-associated heme-containing bifunctional homodimeric enzyme that catalyzes the first committed step in PGs biosynthesis. PGHS presents two different isoforms PGHS-1 and PGHS-2. The generic name for these two isozymes are cyclooxygenase-1 (COX-1) and cyclooxygenase-2 (COX-2). Chronologically the COX-1 isoform was first purified³⁰ in 1976 and cloned³¹ in 1988. At the time, the formation of PGs was assumed to involve only a single COX enzyme, but in 1991 several groups reported a gene with the same activity of COX enzyme.^{2, 32, 33} This new gene was referred to the second isoform of PGHS, called the inducible COX-2. The discovery of COX-2 stimulated many scientists along the '90s to investigate about: the physiological role of both isoforms, the pharmacologic agents to inhibit differentially COX-1 and COX-2, and the characterization of the prostanoid biosynthetic pathway.^{2, 34}

Nowadays, it is known that both isoforms show differences in some physiologic actions and present distinct prostanoid biosynthetic pathways.^{2, 22, 32} COX-1 is constitutively expressed in our cells and is required for the production of PGs involved in basic housekeeping functions throughout the body. In contrast, COX-2 is an inducible isoform, whose expression is activated in a variety of cells in response to inflammation, growth factors, tumour promoters or cytokines. COX-2 is the principal source of PGs that contribute to inflammation, but also those PGs are involved in several pathologies. However, COX-2 can act at two different steps: at the initiation and resolution of the inflammation.^{22, 29} For that reason, this thesis only focuses on the isoform that makes the greatest contribution to the inflammatory process, COX-2.

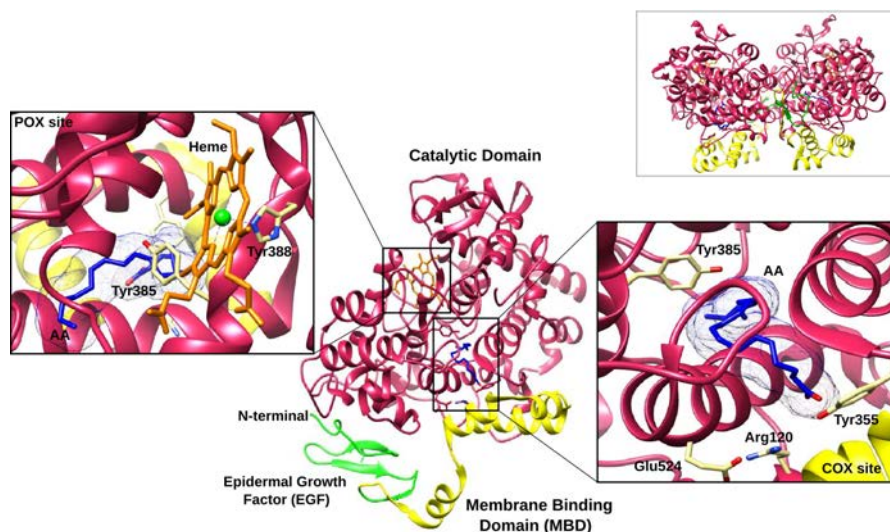


Figure 1.4: On the top right, the crystallographic structure of the heme-containing homodimer enzyme, COX-2 (3HS5 pdb)¹ is represented. In the middle, the three domains of each monomer are represented: the N-terminal Epidermal Growth Factor (EGF) domain (green), the Membrane Binding Domain (MBD) (yellow), and the C-terminal globular Catalytic Domain (pink). Box on the bottom right shows the COX active site interacting with AA. Box on the left shows the POX active site.

1.2.1 PGHS-2 structure

Prostaglandin Endoperoxide H Synthase 2 (or Cyclooxygenase-2) is a heme-containing bifunctional homodimer enzyme that oxygenates principally AA to generate PGH₂. The X-ray crystal structures of (murine or human) COX-2 filed in Protein Data Bank (PDB)^{1, 6} show that both monomers have an identical primary structure. Each monomer is made up of three domains (Fig.1.4): the N-terminal Epidermal Growth Factor (EGF) domain, the Membrane Binding Domain (MBD) and the C-terminal globular Catalytic Domain.

The *N-terminal EGF* domain is formed by 50 amino acids, whose potential role is to form part of a portion of the interface between the two monomers.^{2, 22} The neighbouring *MBD* is made up of four short

consecutive amphipathic α -helices, the last of which directly merges into the catalytic domain, called α -helix D. The amphipathic helices create a hydrophobic patch to interact with one face of the underlying bilipid layer. This patch provides fatty acid substrates and NSAIDs a direct entrance to the cyclooxygenase active site.² Finally, the *C-terminal Catalytic Domain* is the largest domain that encompasses about 460 residues. The catalytic Domain has two mechanistically coupled, spatially distinct active sites:²² the cyclooxygenase active site (called COX active site) and the peroxidase active site (called POX active site). The cyclooxygenase active site is made up of one hydrophobic channel, which begins before the Arg-120 residue, and extends 25 Å from the MBD to Gly-533 residue. In contrast, the POX active site is located on the surface of the protein and contains a Fe⁺³-protoporphyrin IX group,^{33, 35} called the heme cofactor, coordinated with the axial histidine His388 (Fig.1.4).

1.2.2 Substrates binding to COX active site

As I mentioned before, the catalytic domain of COX-2 has two active sites, POX and COX, in both monomers (Fig.1.4). Even so, only the COX active site has a hydrophobic channel to bind the fatty acid and allow it to interact with the enzyme to initiate the catalytic reaction.

In the mid-90s, two main questions remain open: first, the the lack of knowledge of which COX active site the substrate prefers to join, and second, the arrangement of the substrate in the cavity. Then in the late '90s, the first model of how AA interacts with COX active site was proposed by an experimental group.³⁶ Nevertheless, it was not until the beginning of the 2000 when scientists began to find out the best arrangement of the substrate inside the hydrophobic channel.^{37, 38} Years later the cross-talk between COX-2 monomers and the binding of fatty acids at both COX active sites were demonstrated by two publications of Yuan C. et al.^{39, 40}. These studies showed that only one monomer can catalyze the formation of prostaglandin and the non-catalytic monomer functions as an allosteric regulator of the catalytic monomer.

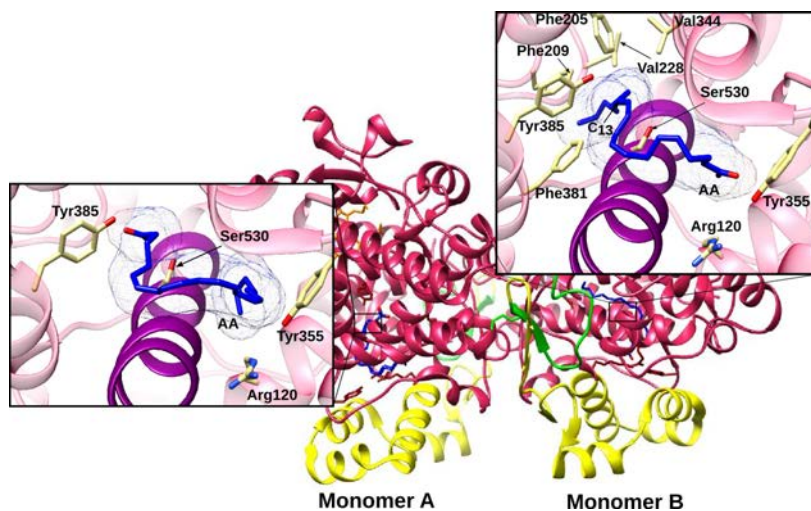


Figure 1.5: The X-ray structures of COX-2:AA. Box on the right shows the hydrophobic channel of monomer B, interacting with the "L-shaped" productive AA conformation. Box on the left shows the hydrophobic channel of monomer A, interacting with the nonproductive AA conformation.

Even though AA is the preferred substrate for COX-2, the enzyme also tends to bind to fatty acids substrates with different chain lengths, such as EPA or DHA.⁴¹ In 2010 an experimental study by Vecchio A.J. et.al¹ was performed, in which the X-ray structures of COX-2:AA, COX-2:EPA and COX-2:DHA complexes were determined. In this study, they observed that AA and EPA in monomer A exhibits a non-productive binding mode (unable to react), and in monomer B exhibits an "L-shaped" productive binding conformation (Fig.1.5). Conversely with DHA no difference between monomers was observed.

The understanding of the catalytic reaction inside COX involved knowing the difference between productive and non-productive binding of the fatty acid in the hydrophobic cavity, see Figure 1.5. The fatty acid substrate is bound to COX active site in a productive binding mode when it adopts an extended "L-shaped" conformation with two or more kinks in the centre (depending of the FA). The substrate carboxylate lies near the side chains of Arg120, Tyr355 at the opening of the channel. The middle portion of the substrate adopts an S shape

that meanders around the side chain of the residue Ser530, positioning C₁₁ above a small pocket into which O₂ could migrate from the lipid bilayer.³⁷ The S shape also places C₁₃ below the phenolic oxygen of Tyr385, ready to start the cyclooxygenase reaction by a hydrogen abstraction from C₁₃. Finally, the substrate ω -end is encased by residues Phe205, Phe209, Val228, Val344, Phe381, and Leu534 that form a hydrophobic groove above Ser530, and where the terminal carbon lies adjacent to Gly533. Conversely, in a non-productive conformation the fatty acid carboxylate bound to Tyr385 and Ser350 at the apex of the end of the channel instead of near the opening.¹

To describe in detail the catalytic reaction, in the following section the reaction mechanism is explained by taking the conversion of AA to PGH₂ as a reference for the other fatty acids.

1.3 Catalytic Reaction

As explained in section 1.2, the biosynthesis of prostaglandins takes place in the catalytic domain. The catalytic reaction involves the conversion of AA to PGH₂. This reaction occurs in two stages, which are catalyzed in COX and POX active sites. The COX active site catalyzes the dioxygenation of AA to yield prostaglandin G₂ (PGG₂). PGG₂ is then released to the heme-containing POX active site located near the protein surface, where its 15-hydroperoxide group is reduced to give PGH₂. The peroxidase activity can work independently of the cyclooxygenase one.³⁵ Conversely, cyclooxygenase activity is peroxide-dependent.² This results from the fact that in the resting state of COX-2, the active peroxidase site contains the heme cofactor, which has to be activated in order to start the reaction in COX active site.⁴² To do so, an alkyl hydroperoxide (ROOH) activates the heme group by means of a two-electron oxidation, yielding the corresponding alcohol (ROH) and an oxy-ferryl protoporphyrin IX radical cation, which, in turn, is reduced by an intramolecular electron transfer from Tyr385 placed in the COX active site.^{33, 35} This indicates that the two active sites are close in space, and an interaction between them is required to convert Tyr385 to its active radical form. The so-formed tyrosyl radical ini-

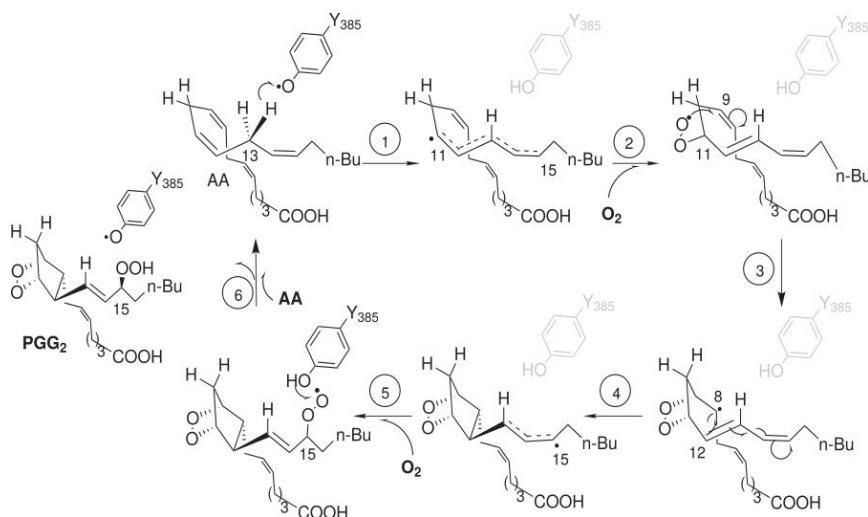


Figure 1.6: All-Radical Mechanism

tiates the catalytic cycle in the COX active site when the substrate AA occupies this site. Electron paramagnetic resonance (EPR) spectroscopy^{43–45} shows the formation of Tyr385 radical after the addition of an alkyl hydroperoxide and the appearance of an arachidonate radical following the addition of AA.

So far, the COX activity of COX-2 remains the focus of much attention for being also the site of the anti-inflammatory inhibition of NSAIDs.

1.3.1 Reaction Mechanism in the COX active site

There is a general agreement^{32, 33, 46–49} about the mechanism that rules such an important enzyme reaction in the COX active site. Although its molecular details have not been entirely clarified yet. For that reason, the resolution of the molecular details of the reaction mechanism in the COX active site is the main focus of this thesis.

The classical six-step all-radical mechanism (Fig.1.6) derives from proposals by Hamberg and Samuelsson more than 50 years ago.²¹ After a C₁₃ H-proS abstraction from AA by a tyrosyl radical, a delocalized C₁₁–C₁₅ pentadienyl radical is generated (step 1). An antarafacial O₂

addition at C₁₁ yields a 11R peroxy radical (step 2), which yields a C₈-radical cyclic endoperoxide by means of a 9,11-cyclization (step 3). Step 4 consists of an 8,12-cyclization leading to a bicyclo endoperoxide and a C₁₃–C₁₅ allyl radical. Thereafter, a second O₂ addition at the 15S position (step 5) and a back hydrogen transfer from Tyr385 to the peroxy radical at C₁₅ (step 6) finally give PGG₂.

However, Dean and Dean⁵⁰ proposed later an alternative 10-step carbocation-based mechanism. After C₁₃ hydrogen abstraction from AA, a sigmatropic hydrogen transfer from C₁₀ to C₁₃ takes place, forming a delocalized C₈–C₁₂ pentadienyl radical, followed by an electron transfer from C₁₀ to the heme group, thus producing a carbocation at C₁₀, see Figure 1.7. Then, an 8,12-cyclization, a back electron transfer from the heme group to C₁₁, an O₂ addition at C₁₁, a 9,11-cyclization, a hydrogen transfer from C₁₃ to C₁₀, a second O₂ addition at C₁₅, and finally a back hydrogen transfer from Tyr385 to the peroxy radical at C₁₅ lead to PGG₂.

Several important points that Dean and Dean argued in favor of their carbocation-based mechanism were:

- Autoxidative cyclization of polyunsaturated fatty acid hydroperoxides in solution to form prostaglandin-like bicyclo endoperoxides through an all-radical mechanism highly favors *cis*-disubstituted cyclopentane isomers,⁵¹ in clear opposition to the *trans* isomers corresponding to the natural prostaglandins generated by COX-2.
- If 10,10-difluoroarachidonic acid is the substrate, COX enzymes do not generate any cyclic prostaglandin-like products, but a cyclic alcohols such as 10,10-difluoro-11*S*-hydroxyeicosatetraenoic acid.⁵² Thus, it seems that the existence of hydrogen atoms at C₁₀ would be required for the formation of prostaglandins.
- Chirality at C₁₅ is supposed to be better explained when the C₁₀–C₁₃ hydrogen shift occurs.

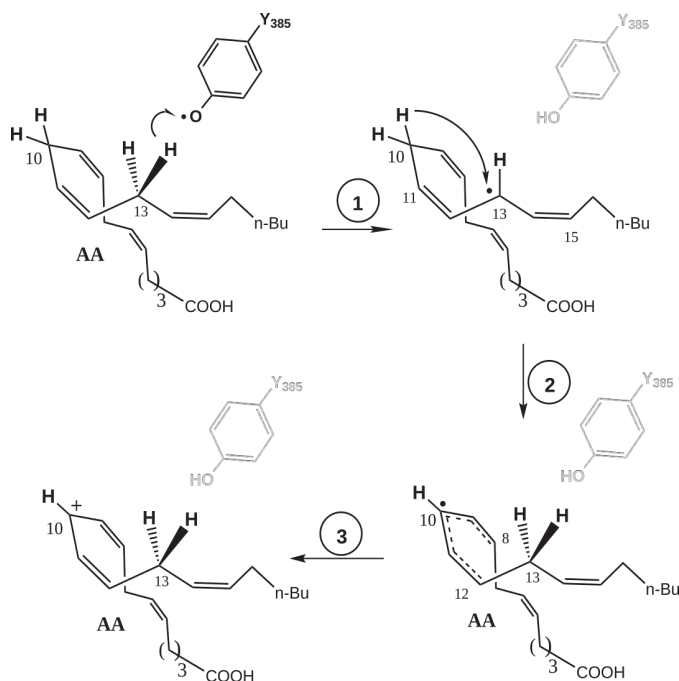


Figure 1.7: Formation of the carbocation at C₁₀ according to the Carbocation-Based Mechanism

Very recently, Navratil et al.⁵³ have studied the ex vivo deuterium isotope effect for the enzymatic oxidation (by cyclooxygenases and lipoxygenases) of AA by macrophages. They have found that deuteration of C₁₀ promotes the formation of Lipoxin B₄, likely by interfering with AA cyclization and shunting AA to the lipoxygenase pathway under physiological conditions.

To compare at a detailed molecular level the two different mechanisms explained above, in this thesis the first theoretical study of the complete mechanism of reaction corresponding to the conversion of AA to PGG₂ catalyzed by the enzyme COX-2 is presented.

1.3.2 Regioselectivity and Stereoselectivity

PGH₂ is the principal product generated by COX-2 upon dioxygenation of AA, as it is described above. The all-radical mechanism requires

a very selective stereochemistry for the formation of PGG₂. The reaction generates five independent chiral centres, giving rise to the possibility of the formation of ten different stereoisomers capable of forming the PGG₂. This experimental analysis was carried out by O'Connor et al.⁵¹ in 1984. The study demonstrated that there exists several stable intermediate isomers along the all-radical mechanism in solution. Even so, there is only one isomer that can reach enzymatically to the PGG₂ structure.

Alternatively, in a minor amount, the mechanism has been shown to produce 11(R)-hydroperoxy-eicosatetraenoic acid (11R-HpETE) and 15-hydroperoxy-eicosatetraenoic acid (15-HpETE), see Figure 1.8. Subsequently, both HpETEs are reduced by the POX active site to form 11(R)-hydroxyeicosatetraenoic acid (11R-HETE) and 15-hydroxyeicosatetraenoic acid (15-HETE), being the former the major secondary product of the biosynthesis⁵⁴ (Fig.1.8). Nevertheless, in the '80s, it was not clear neither the stereochemistry of the O₂ addition at C₁₅ to obtain 15-HpETE, nor how COX achieves such a regio/stereo-selectivity to form PGG₂.

Then, many studies^{32, 33, 36} began to be conducted on the stereochemistry of the reaction mechanism in COX-2 by the discovery of the COX-2 isoform, and the subsequent knowledge of the "L-shaped" conformation of the AA inside the hydrophobic cavity.

However, the production of HETE as a product was revealed by the discovery of the anti-inflammatory effect of aspirin (a NSAID) inside COX-2,^{6, 55} allowing the inhibition of PGG₂ and the production of 15R-HETE (see section 1.5). In light of recent discoveries, scientists wondered if 15R-HETE could be obtained by COX-2 or otherwise presents the same stereochemistry as the natural 15S-PGG₂. Over the past 30 years, different hypothesis about the correct stereochemistry of 15-HETE for COX-2 and aspirin-acetylated COX-2 have been proposed by several experimental⁵⁵⁻⁵⁷ and computational⁸ studies. However, most attention has been focused on the formation of 15R-HETE in the aspirin-acetylated COX-2 (see section 1.5.1). For that reason, the stereochemistry of 15-HETE in COX-2 has not yet reached an agreement (Fig.1.8).

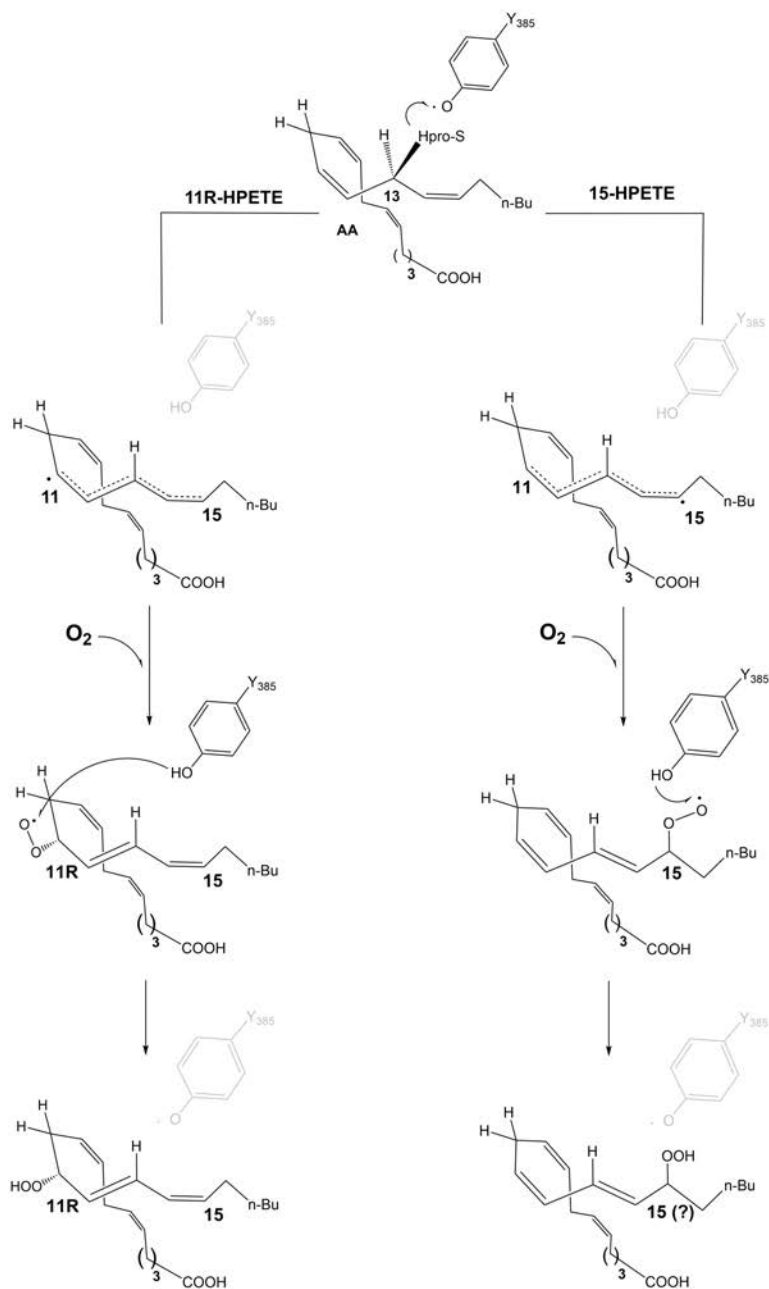


Figure 1.8: Secondary products of the all-radical mechanism. The left path represents the production of the 11R-HpETE. The right path represents the production of the 15-HpETE.

1.4 Gly526Ser Mutation in COX-2:AA

Another way to understand experimentally the amazing features of the six-step all-radical mechanism is by mutagenesis. Scientists, helped by mutagenesis experiments, understood how COX-2 manages to control the stereochemistry and regioselectivity of the reactions it catalyzes. In these experiments, the identification of the residues of the active site that have potential contact with the substrate is crucial.

A number of mutagenesis experiments have been performed to better understand the way those residues act along the biosynthesis of prostaglandins.⁵⁸⁻⁶⁰ Particularly interesting is the case of the Gly526Ser (G526S) mutant of human COX-2.⁶⁰ This mutation does not appear to interfere with the three first reaction steps of the mechanism (Fig.1.6). However, no formation of prostaglandins was detected and the 11R-HETE becomes the main product. Nevertheless, the results of the Reverse phase High performance liquid chromatography (RP-HPLC) analyzes of the products formed by G526S COX-2 mutant also reveal three minor products. Surprisingly, these secondary products never were formed by COX-2. For that reason, Schneider et al.⁶⁰ proposed that the 8,12-cyclization in the G526S mutant is sterically hindered by misalignment of the substrate carbon chain. So, instead of prostaglandins they found novel products that were identified as 8,9-11,12-diepoxy-13R-(or 15R)-hydroperoxy derivatives of arachidonic acid. The corresponding reaction mechanism is presented in Figure 1.9.

As a final conclusion, in that paper the Gly526 residue is considered by Schneider et al.⁶⁰ an important active site residue for the synthesis of PGG₂. For that, its mutation to Ser526 inhibits PGG₂ formation and leads to the three diepoxy products mentioned before.

In this thesis a computational study has been performed, in order to complement these experimental evidences and contribute to the understanding of the catalytic function of COX-2. The study provides the molecular details of the way how that apparently an significant mutation is able to fully arrest the PGG₂ biosynthesis, instead yielding diepoxy products.

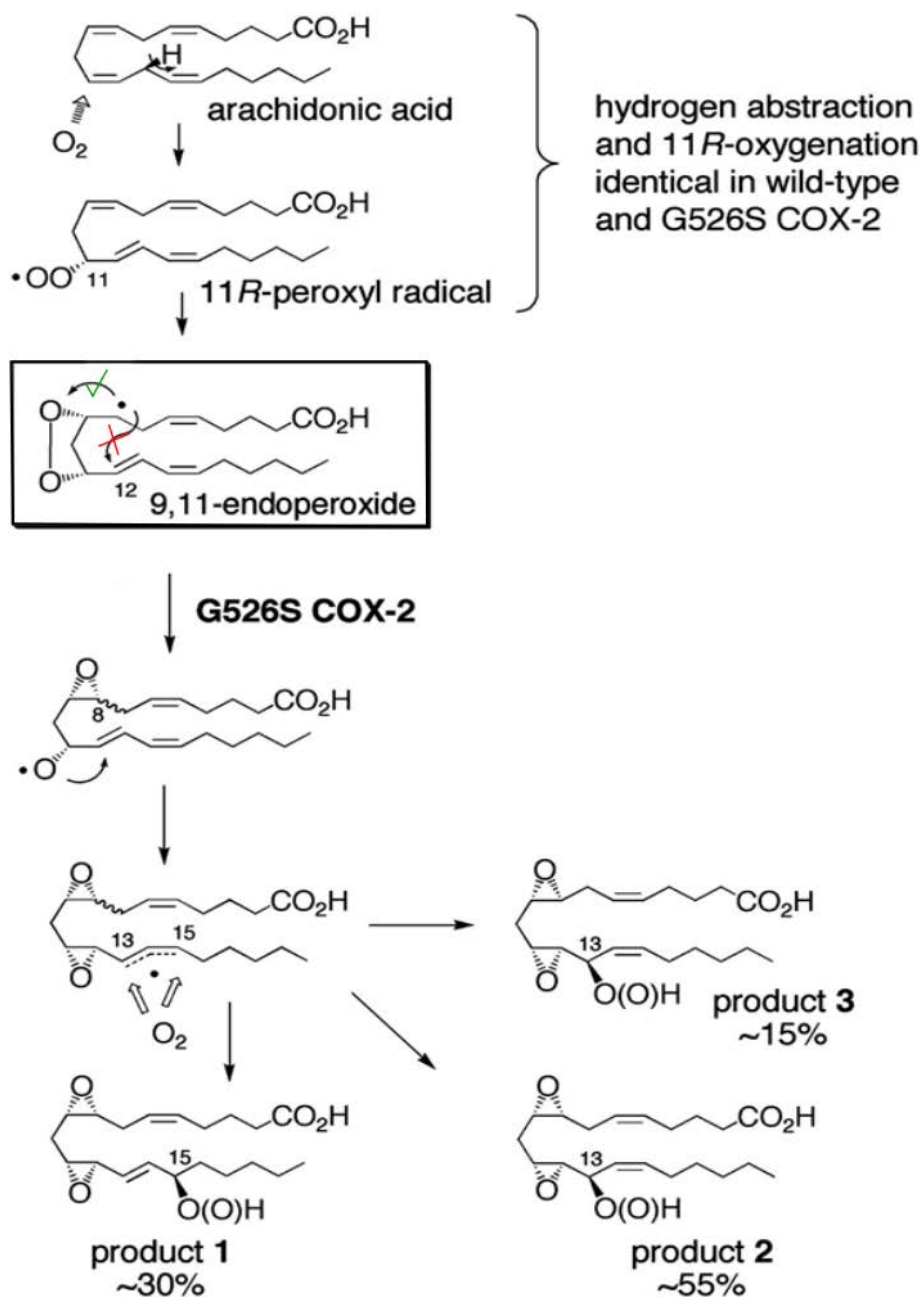


Figure 1.9: Reaction mechanism proposed by Schneider et al. to obtain the new novel products in the Gly526Ser COX-2 mutant.⁶⁰

1.5 Anti-inflammatory path of COX-2:AA

Nonselective blockage of PG biosynthesis by NSAIDs results in anti-inflammatory, analgesic and antipyretic effects, as well as undesirable gastrointestinal (GI) and renal toxicities.³⁻⁸ Nowadays, the NSAIDs are among of the most highly prescribed drugs, such as, for instance, aspirin, ibuprofen, naproxen and diclofenac. NSAIDs exert their action by inhibiting both PGHS isoforms: COX-1 and COX-2.⁶¹

Nevertheless, COX-1 inhibition depresses the prostaglandin production, involved in gastroprotection.¹⁸ In contrast, COX-2 inhibition is the true molecular target for the anti-inflammatory effects of NSAIDs.⁵⁵ For that reason, side effects associated with nonselective NSAIDs prompt scientists to synthesize new molecules, selective COX-2 inhibitors, to reduce GI and renal side effects. In 1999, the Coxibs family was introduced, as the first selective COX-2 inhibitors.⁶² Since then, NSAIDs are classified, generally, in non-selective or selective for COX-2, as well as reversible or irreversible inhibitors.

Aspirin, one of the oldest and most common anti-inflammatory NSAIDs, is the only irreversible inhibitor. Aspirin inhibits both PGHS isoforms. For that reason, its inhibition is related to a well-known benefit in the prevention and treatment of cardiovascular diseases. A recent study⁶³ has demonstrated how the prediagnostic use of NSAIDs, such as aspirin, and selective COX-2 inhibitors was associated with a reduced rate of breast cancer recurrence.

However, a complete molecular understanding of aspirin action is still lacking, just as the formation of the highly controlled stereochemical products is still presenting contradictory experimental explanations (section 1.5.1). For that, in this thesis a theoretical study is performed, in order to contribute to the understanding of the biological effects of aspirin.

In the following subsections, first the irreversible inhibition of aspirin is described, followed by a brief explanation of the experimental contradictions about how the enzyme controls the stereochemistry of the products.

1.5.1 Inhibition by Aspirin

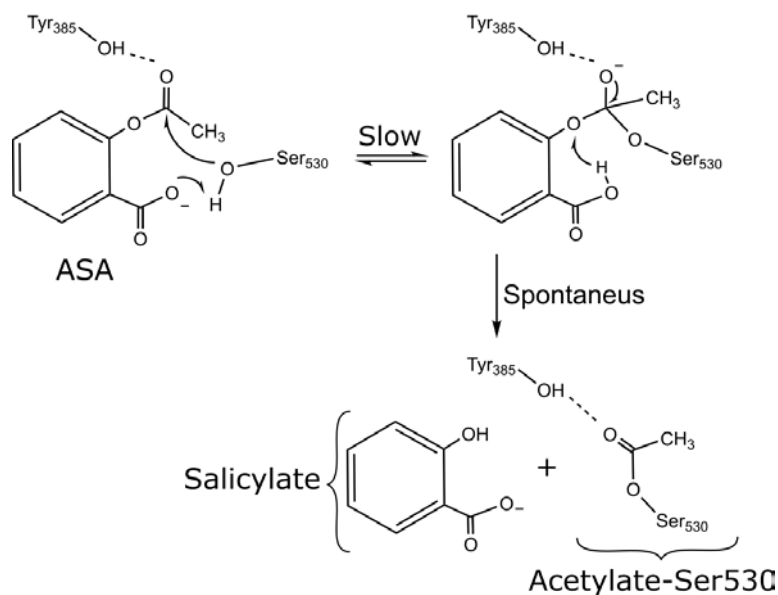


Figure 1.10: Reaction mechanism of Acetylsalicylic Acid (ASA) (called aspirin) acetylating Ser530 of COX-2.⁴

Aspirin (acetylsalicylic acid), so named for its ingredients acetyl and spiralic (salicylic) acid, is one of the most popular and commonly used therapeutic drugs in the world. For the sake of example, it can relieve pain, fever, and inflammation,^{64, 65} as well as it reduces the rate of breast cancer recurrence.⁶³ The main pharmacological molecular target of Aspirin, as a NSAID, is the enzyme COX-2.^{66, 67}

Aspirin is the only NSAID that covalently transforms COX-2, so acting as an irreversible inhibitor. This occurs through the transfer of the acetyl group of aspirin to the hydroxyl group of residue Ser530 of COX-2,^{4, 55, 68-71} see Figure 1.10, obtaining the aspirin-acetylated COX-2 enzyme.

1.5.1.1 Reaction Mechanism in aspirin-acetylated COX-2

Concerning to the cyclooxygenase reaction, it has been widely accepted so far⁴⁹ that the acetylation hinders PGG₂ formation from AA, but

it is still able to produce HpETEs that subsequently are reduced to the respective HETEs, see Figure 1.11. What it is the same, aspirin-acetylated COX-2 no longer behaves as a cyclooxygenase but like a lipoxygenase enzyme. Xiao et al.⁵⁶ showed that both human wild-type COX-2 and aspirin-acetylated COX-2 produced only the 11R- and 15R-HETE lipoxygenation products from AA, in the case of COX-2 just as side products of PGG₂. This stereochemistry at C₁₅ turns out to be opposite to that in PGG₂, see Figure 1.11.

However, even knowing that Ser530 becomes acetylated (Fig.1.10), the way aspirin-acetylated COX-2 manages to block PGG₂ formation and, in spite of that, to produce 15R-HETE as the main product remains quite uncertain.

Schneider and Brash⁵⁷ proposed that the bulky acetyl group in Ser530 forces the rotation of the ω -chain of AA around the C₁₃-C₁₄ bond, in such a way that the methyl end comes close to the carboxylate end. This AA realignment causes a reversed oxygenation stereochemistry at C₁₅ leading to 15R-HETE as the exclusive enzymatic product and probably shields the access of molecular oxygen to C₁₁, so hindering PGG₂ formation. In contradiction to that realignment, almost simultaneously, site mutagenesis experiments⁵⁹ by Rowlinson et al. indicated that AA maintains in aspirin-acetylated COX-2 the same "L-shaped" binding conformation as in wild-type COX-2, with the AA ω -end in an alternate conformation in the same region (hydrophobic groove) above Ser530. Those authors found that murine aspirin-acetylated COX-2 produced 15R-HETE as the major product and a small amount of 11R-HETE. Small quantities of prostaglandins, which were attributed to the presence of residual uninhibited COX-2, were also detected. Sharma et al.⁷² have also reported that 15R-HETE is the main product of the aspirin-acetylated COX-2 with AA.

The formation of 15R-HETE, as the main product of the aspirin-acetylated COX-2, is a very physiologically relevant fact because 15R-HETE can be further oxidized to aspirin-triggered lipoxins. These bioactive compounds called lipoxins have a well-known anti-inflammatory activity,^{73, 74} thus contributing to the therapeutic effects of aspirin. Conversely, the 15S-hydroxyl group of prostaglandins is essential for their bioactivity.^{75, 76}

On the other hand, EPR studies have shown the same characteristics for the peroxy-induced Tyr385 radical in human COX-2 than in aspirin-acetylated COX-2, a 29–30-G wide singlet.^{56, 77} As stated in section 1.3, hydrogen abstraction at C₁₃ of AA by the Tyr385 radical in COX-2 leads to a planar delocalized C₁₁–C₁₅ pentadienyl radical that will react then with molecular oxygen. Tsai et al.⁷⁷ have found that the Tyr385 radical in aspirin-acetylated COX-2 is able to oxidize AA to three possible carbon-centered radical intermediates: a planar delocalized C₁₁–C₁₅ pentadienyl radical and two twisted allyl radicals delocalized over either C₁₁–C₁₃ or C₁₃–C₁₅, these last radicals leading to either 11R-HETE or 15R-HETE, respectively, by addition of molecular oxygen. The acetylation of Ser530 would restrict the conformational space accessible to the AA radical intermediate, so forcing the formation of an allyl radical rather than a planar pentadienyl radical. Note that an allyl radical would not preserve the planarity of carbons C₁₁–C₁₅.

Recently, Lucido et al.⁶ have resolved the X-ray crystal structures of human aspirin-acetylated COX-2 and human COX-2 in complex with the aspirin precursor salicylic acid to 2.04 and 2.38 Å resolution, respectively, using synchrotron radiation and molecular replacement methods. No significant differences were found between the two monomers of each homodimer, not even with the monomers in the crystal structure⁷² of murine COX-2 complexed with AA.

The crystal structure of human aspirin-acetylated COX-2 indicates that both monomers are acetylated. In addition, the spatial arrangement of the acetylated Ser530 side chain at the top of the cyclooxygenase channel fully blocks the access to the hydrophobic groove: a hydrogen bonding network is formed among the carbonyl oxygen of the acetyl group and the phenolic oxygens of Tyr385 and Tyr348. However, binding of AA in an "L-shaped" conformation,⁶ with insertion of its ω -end into the hydrophobic groove is required to produce 15R-HETE.

Given that the crystal structure of AA bound to the aspirin-acetylated COX-2 could not be determined so far, Lucido et al.,⁶ following a previous suggestion by Tosco,⁸ assume that a suitable rotation of the acetylated side chain toward the constriction site of the cyclooxygenase channel must happen to open the access of the AA ω -end into the hydrophobic groove. This rotated disposition would force AA into

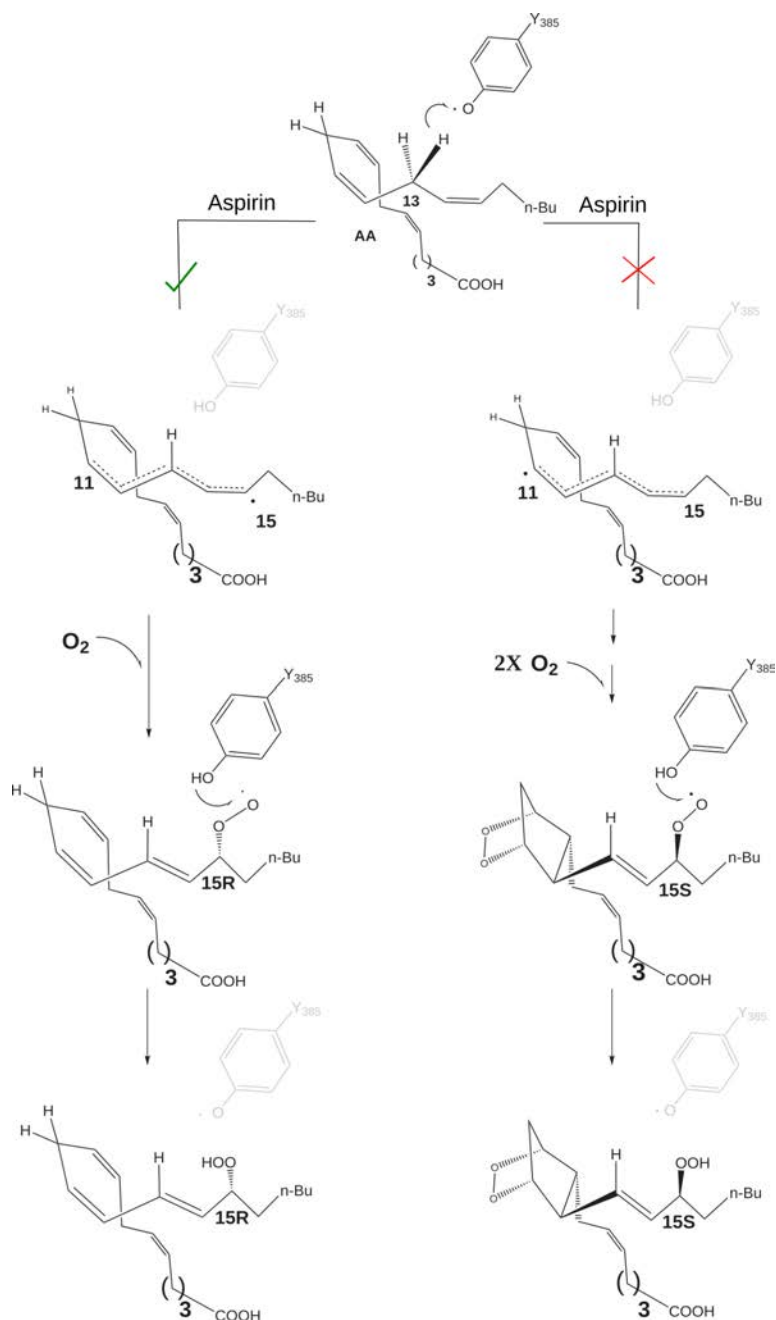


Figure 1.11: Reaction mechanism observed in COX active site of aspirin-acetylated COX-2. The left path represents the formation of the major product, 15R-HpETE. The right path represents the blockage of PGG₂ biosynthesis.

a more extended AA conformation (that is, with a larger distance between C₈ and C₁₂), thus preventing cyclizations,^{6, 8} and straining the C₁₁–C₁₅ pentadienyl radical in such a way that the allyl radical on C₁₃–C₁₅ would be trapped.⁶ Moreover, that rotation would increase the steric shielding of the AA side opposite to Tyr385,⁸ thus changing the molecular oxygen attack at C₁₅ from antarafacial to suprafacial and leading to the 15R stereochemistry. For that rotamer to be possible, the side chain of the close Leu531 should flip away from the constriction site at the channel entrance.⁶ The relevance of the rotation of the side chain of Leu531 has been also remarked very recently by Dong et al.⁷⁸

Checking the literature, the above-mentioned work by Tosco⁸ is the only computational study existing so far on the oxygenation of AA by aspirin-acetylated COX-2. In that paper, Tosco carried out 10 ns molecular dynamics simulations of the complexes murine COX-2:AA C₁₁–C₁₅ pentadienyl radical and aspirin-acetylated murine COX-2:AA C₁₁–C₁₅ pentadienyl radical. The analysis of the last 5 ns showed that the average distance C₈–C₁₂ increases from 4.16 to 4.55 Å under acetylation. According to the author, this result indicates that AA is bound in an extended conformation that would prevent the 8,12-cyclization needed to yield the bicyclo endoperoxide of PGG₂.

At the beginning of 2019, Giménez-Bastida et al.,⁷⁹ using RP-HPLC with a radioactive flow detector, have identified PGE₂ (a stable prostaglandin generated by rearrangement of the highly unstable PGH₂) as the major product formed from AA by recombinant human COX-2, as expected. In the case of aspirin-acetylated COX-2, 15-HETE has been the major product, again as expected. However, early eluting radioactive material at the retention time of prostaglandins was also detected in aspirin-acetylated COX-2, accounting for about 15% of all enzymatic products generated. Analysis of that material using Straight-phase High performance liquid chromatography (SP-HPLC) with radiodetection very surprisingly has shown the formation of PGE₂ in a 70/30 ratio of the 15R/15S epimers. Kinetic analysis indicated that the formation of that mixture of PGE₂ C₁₅ epimers by aspirin-acetylated COX-2 is almost 25-fold less than for PGE₂ by COX-2 and about 8-fold less than for 15R-HETE. To explain their results, the authors conclude that AA binds in the aspirin-acetylated COX-2 with its AA ω-end in the hydrophobic groove above Ser530, as it is in COX-2.

With this conformation, COX catalysis would proceed normally up to the final oxygenation at C₁₅, which leads now to an R-configuration. So, an unstable 15R-PGH₂ would be formed, which was detected as its stable 15R-PGE₂ and 15R-PGD₂ transformation products.

After the brief explanation of the topic along the last 25 years, it becomes clear that the understanding of how aspirin-acetylated COX-2 controls the stereochemistry of the oxygenation reaction of AA still poses challenging questions nowadays. Besides, some of the available experimental results seem to be contradictory to each other. In other words, although it might be sound quite surprising, some very relevant molecular details of aspirin action (and, therefore, the full comprehension of its beneficial physiological effects) remain unidentified so far.

For that reason, as mentioned before in this thesis a computational study has been performed to contribute for a better understanding of the biological effects of aspirin.

Part II

Theoretical Background

Chapter 2

Computational Methods

Theoretical chemistry arose as a discipline of chemistry at the time in which both mathematical algorithms and physics laws met together to explain certain processes of chemical interest.⁸⁰ Nowadays, theoretical chemistry has quickly become a large scientific area. It supports an explanation of the behavior of nature from a chemical, physical, mathematical, biological, medical and pharmacological perspective. Thence, theoretical chemistry puts all the effort to validate the computational methods and bolster the experimental results.

Nature presents plenty of different molecules (small and large) whose energies are extremely difficult to calculate. From a chemical point of view and assuming the Born Oppenheimer approximation, the movements of the nuclei and the electrons in a molecule are treated separately, allowing the Potential Energy Surface (PES) description by classical or quantum methods.⁸¹ Therefore, theoretical chemistry presents different levels of theory: Molecular Mechanics (MM), Quantum Mechanics (QM) and Quantum-Mechanics/Molecular-Mechanics (QM/MM), to describe the potential energy function of each system.

In this chapter, how MM describes molecular systems is introduced. Then, the QM method used in this thesis is briefly explained. Continuously, the hybrid QM/MM method is explained, followed by the explanation of two different approaches used in this thesis for QM/MM calculations. Finally, the Molecular Dynamics method is introduced.

2.1 Molecular Mechanics

Molecular Mechanics uses classical mechanics to describe the potential energy of a molecule. This means that each atom is treated as a classical particle with a determined mass, net charge and radius. Thus, the potential energy of a system is calculated as a function of the nuclear positions ignoring the electron motion. Hence, MM cannot describe neither bond breaking nor bond forming processes. However, for example, the changes in torsional conformations and non bonded interactions are the kind of chemical processes that MM was designed to model.

Historically, Molecular Mechanics was formulated in 1946 by Westheimer,⁸² Hill,⁸³ and Mayer,⁸⁴ as a general method for studying the variation of the energy of small organic molecules as a function of their molecular conformation. Over the years several scientific contributions to the development of MM have allowed this method to be also used to simulate the geometry and energy of large biological molecules.

2.1.1 Mathematical expression: Forcefield

The principle behind MM is the mathematical expression of the potential energy of a molecule which is a function of the position of N atoms. This mathematical equation is called the Forcefield (FF). The FF can be written as:

$$\begin{aligned} \mathbf{E}_{MM} = & \sum_{bonds} \mathbf{E}_{Stretching} + \sum_{angles} \mathbf{E}_{Bending} \\ & + \sum_{torsions} \mathbf{E}_{Torsional} + \sum_{Non-Bonded} \mathbf{E}_{Interactions} \end{aligned} \quad (2.1)$$

where \mathbf{E}_{MM} expresses the potential energy of the N atoms of a molecule. The potential energy is composed of the sum of two types of contributions: the bonded and non-bonded terms given in equation 2.1. The *bonded* term is defined as the sum of the following contributions: (i) the stretching energy that accounts for bond stretches between pair of

bonded atoms ($\mathbf{E}_{Stretching}$); (ii) the bending energy of the valence angles between three atoms ($\mathbf{E}_{Bending}$), and (iii) the torsional energy of the dihedral angles between four atoms sequentially bonded ($\mathbf{E}_{Torsional}$). The *non-bonded* term is defined as the sum of the non-bonded interactions ($\mathbf{E}_{Interactions}$) between all pair of atoms (i and j) that are not directly bonded and are separated at least by three bonds or that are in different molecules.

In most forcefields the commonly used functional form for each one of the energy contributions indicated in equation 2.1 is given in the following mathematical expression:

$$\begin{aligned} \mathbf{E}_{MM} = & \sum_{\text{bonds}} k_b (l_i - l_0)^2 + \sum_{\text{angles}} k_\theta (\theta_i - \theta_0)^2 \\ & + \sum_{\text{torsions}} k_\phi [1 + \cos(n\phi - \delta)] \\ & + \sum_{\text{Non-bonded pairs}} \left\{ \frac{q_i q_j}{4\pi\epsilon_0 r_{ij}} + \epsilon_{ij} \left[\left(\frac{\sigma_{ij}}{r_{ij}} \right)^{12} - \left(\frac{\sigma_{ij}}{r_{ij}} \right)^6 \right] \right\} \end{aligned} \quad (2.2)$$

where the *Stretching energy* ($\mathbf{E}_{Stretching} = k_b (l_i - l_0)^2$) represents the energy needed to change the bond length of the bond i from the reference bond length, l_0 to the current bond length l_i . This is modelled by the harmonic approximation (Hooke's law). k_b is considered to be the force constant associated to the bond.

The *Bending energy* ($\mathbf{E}_{Bending} = k_\theta (\theta_i - \theta_0)^2$) represents the energy needed to change the valence angle i from the reference valence angle θ_0 to the current value θ_i . This is modelled using Hooke's law or harmonic potential. k_θ is considered to be the force constant of an angle.

The *Torsional energy* ($\mathbf{E}_{Torsional} = k_\phi [1 + \cos(n\phi - \delta)]$) considers four atoms sequentially bonded (A-B-C-D), expressing the rotation of the dihedral angle between A, D atoms. k_ϕ represents the rotational barrier of the bond B-C, n is the multiplicity (number of minimum energy points in the function over a 360° rotation), ϕ is the dihedral angle, and δ is the phase factor, which determines where the dihedral has its minimum value.

Finally, the *Non-Bonded terms* (Eq.2.2) represent the contribution of two different non-bonded interactions: (i) the electrostatic interactions and (ii) the van der Waals interactions. The *electrostatic interactions* can be modeled by the Coulomb's law; where q_i and q_j are the net atomic charges of atoms i , j , and ϵ_0 is the dielectric constant. The *van der Waals interactions* described by Lennard-Jones 12-6 potential; where r_{ij} is the distance between two atoms, ϵ_{ij} is four times the potential well depth and σ_{ij} defines the collision diameter at which the energy becomes zero. Moreover, the attractive and repulsive energy contributions are well characterized by this Lennard-Jones potential with an attractive part that varies as r^{-6} and a repulsive part that varies as r^{-12} .

Once a functional form for each energy contribution has been chosen, the values of all the different parameters involved (force constant, reference values etc) must be specified. The parameterization of a forcefield is not a trivial task, in which modelling a new class of molecules can be a complicated and time-consuming procedure. It is important to keep in mind that a forcefield always should try to reproduce the molecular properties in the correct environment. To do so, experimental data is needed but sometimes it is difficult to obtain it for particular classes of molecules. *Ab initio*⁸⁵ and *DFT*⁸⁵ calculations reproduced accurately the experimental results. For that reason, Quantum Mechanics (QM) calculations are usually used to reproduce the data for the parameterisation of FF.

Apart from these contributions, it is important to define the concept of *Atom Type* in a forcefield. The atom type term defines: the atomic number of an atom, its hybridization state and the type of chemical bond that presents with other atoms.⁸¹ Thus, *Atom Type* term is a distinctive trait of each FF. This means that the atom type reflects the neighbouring environment of an atom inside a molecule.

Different forcefields exist depending on the functional form of the energy contributions, the set of parameters, the atom types and their scope of applicability. For example MM2⁸⁶, MM3⁸⁷ and MM4⁸⁸ forcefields are widely used for calculations on organic molecules. On the other hand, AMBER⁸⁹, CHARMM⁹⁰ and GROMOS⁹¹ forcefields are commonly used for calculations on biomolecules in which the atom types can be classified considering the protonation state of the residues.

However, transferability is a very important feature of a forcefield. Transferability refers to the ability to transfer the same set of parameters of a molecule to a series of related molecules, rather than to calculate new parameters for each molecule.⁹²

2.2 Quantum Mechanics

The origin of the **Quantum Mechanics** (QM) term comes from Latin in which '*quantum*' means 'How much' and '*mechanics*' means (in physics) the study of the behaviour of bodies under the action of forces. However, in a chemical context Quantum Mechanics treats molecules. Molecules are constituted by atoms which are made of nuclei (protons and neutrons) and electrons. Quantum mechanics explicitly represents the electrons, making possible to define molecular properties that depend upon the electronic distribution. This means that Quantum Chemistry deals with the motion of electrons under the influence of the electromagnetic force exerted by the nuclear charge and the rest electrons. In particular, QM allows to study chemical reactions in which the bond-making and bond-breaking are involved.

2.2.1 Time-independent Schrödinger Equation

This thesis is focused on the solution of the non-relativistic, time-independent Schrödinger equation (Eq.2.3) where E is the total energy of the state described by the wavefunction Ψ and \hat{H} is the Hamiltonian.

$$\hat{H}\Psi = E\Psi \quad (2.3)$$

The mathematical expression of the time-independent Hamiltonian operator is expressed by the contribution of the kinetic energy of the electrons and nuclei, the attractive interactions between electrons and nuclei, and the inter-electronic and inter-nuclear repulsions (Eq.2.4).

$$\begin{aligned} \hat{H} = & -\sum_i \frac{\hbar^2}{2m_e} \nabla_i^2 - \sum_k \frac{\hbar^2}{2m_k} \nabla_k^2 \\ & - \sum_i \sum_k \frac{e^2 Z_k}{r_{ik}} + \sum_{i < j} \frac{e^2}{r_{ij}} + \sum_{k < l} \frac{e^2 Z_k Z_l}{r_{kl}} \end{aligned} \quad (2.4)$$

where i and j represent the electrons, k and l represent the nuclei, \hbar is the Planck constant divided by 2π , m_e and m_k represent the mass of the electron and the nucleus k , respectively, ∇^2 is the Laplace operator, e represents the electron charge, Z_k and Z_l represent the corresponding atomic number and r_{ij} , r_{ik} , and r_{kl} represent the distance between the corresponding particles.

However, the equation 2.3 is very complex to be solved for systems of M nuclei and N electrons. Then, the Born-Oppenheimer approximation has to be applied. This means that the electron motion can be treated independently of the movement of the nuclei, due to the fact that the electrons are much lighter than the nuclei. Maintaining the nuclei fixed and keeping apart the inter-nuclear repulsion (V_{NN}) the electronic Schrödinger equation is obtained (Eq.2.5).

$$\hat{H}_e \Psi_e = E_e \Psi_e \quad (2.5)$$

where \hat{H}_e is expressed following equation 2.6.

$$\hat{H}_e = -\sum_i \frac{\hbar^2}{2m_e} \nabla_i^2 - \sum_i \sum_k \frac{e^2 Z_k}{r_{ik}} + \sum_{i < j} \frac{e^2}{r_{ij}} \quad (2.6)$$

It is important to emphasize that for a given nuclei configuration the V_{NN} can be recovered according to equation 2.7, where U is the potential energy surface.

$$E_e + V_{NN} = U \quad (2.7)$$

Even so, the electronic Schrödinger equation for a N electron system is still very complex. For that reason, some approximations are

commonly assumed to solve the equation 2.5 for polyelectronic systems. The first of those approximations presented here is the Hartree-Fock (HF) method.

In HF approach each electron is described by a spin-orbital. Since the electrons are particles with a spin of $1/2$, the total wavefunction is expressed as an anti-symmetric product of spin-orbitals organized in a Slater determinant (Eq.2.8).

$$\Psi(1, 2, \dots, N) = (N!)^{-\frac{1}{2}} \sum_{q=1}^{N!} (-1)^{p_q} \hat{P}_q \{ \chi_i(1) \chi_j(2) \dots \chi_k(N) \} \quad (2.8)$$

where N represents the number of electrons, χ_i corresponds to the spin-orbitals, \hat{P}_q is the permutation operator, and p_q is the number of transpositions needed for the permutation. Nevertheless, the HF method presents a limitation for polyelectronic systems. The electron correlation (E_{corr}) between the electrons of different spin is not considered due to the fact that each electron perceives the rest of the electrons as an average electric field. For that reason a lot of *post*-HF methods have been created to include the E_{corr} , for example: Configuration Interaction, Moller-Plesset Perturbation Theory and Coupled Cluster methods.⁸⁵ However, all these *ab initio* methods are computationally expensive for systems with a certain number of atoms (i.e biomolecules). An alternative method to treat systems with many atoms, is based on Density Functional Theory (DFT), which also is focused on including the E_{corr} .

2.2.2 Density Functional Theory

Density Functional Theory (DFT) is an alternative approach to *ab initio* methods that has been used over the past decades to perform calculations with systems of hundreds or more atoms. DFT requires less computational time than the *ab initio* methods to perform the calculations in large systems, but also takes into account electron correlation. The principle behind DFT is based on writing the electronic

energy in terms of electron density ρ . Therefore, the electronic energy, that in this section is called E , is associated to a functional of the electron density $E[\rho]$, and each ρ corresponds to a single energy value.

For a better understanding of the DFT approach, we have to go back to the '90s. In that decade the concept of the relation between the electronic energy and the electron density became popular. This relation was in turn based on the model developed by Thomas-Fermi^{93, 94} in the late '20s. However, the real breakthrough underpinning DFT was developed by Hohenberg and Kohn in 1964⁹⁵ based on two theorems:

FIRST THEOREM: *Any observable of a non-degenerate ground electronic state can be calculated, exactly in theory, from the electron density of the ground state. Expressed differently, energy is a functional of the electron density of the ground state.*

The theorem concretely underpins that the electrons are under the effect of an external potential. This external potential in a molecule is created by the nuclear attraction. Therefore, the first theorem establishes that for a particular external potential $V_{Ne}(\vec{r})$, the properties of the ground state of a polyelectronic system are defined by $\rho(\vec{r})$. Thereby, the electronic energy of the ground state can be expressed following the equation 2.9.

$$E_o[\rho] = \int \rho(\vec{r})V_{Ne}(\vec{r})dr + F_{HK}[\rho(\vec{r})] \quad (2.9)$$

where $V_{Ne}(\vec{r})$ is the external potential corresponding to the attractive interactions between electron-nucleus, and $F_{HK}[\rho(\vec{r})]$ is the Hohenberg-Kohn functional. The functional represents the terms non-dependent of the external potential, see equation 2.10

$$F_{HK}[\rho(\vec{r})] = T[\rho(\vec{r})] + V_{ee}[\rho(\vec{r})] \quad (2.10)$$

where $T[\rho(\vec{r})]$ represents the kinetic energy contributions, and $V_{ee}[\rho(\vec{r})]$ is the summation of the classical and non-classical electron-electron interaction contributions.

The $V_{ee}[\rho(\vec{r})]$ contributions are expressed in equation 2.11.

$$V_{ee}[\rho(\vec{r})] = J[\rho(\vec{r})] + K[\rho(\vec{r})] + J'[\rho(\vec{r})] \quad (2.11)$$

where $J[\rho(\vec{r})]$ represents the classical Coulomb interaction, $K[\rho(\vec{r})]$ is the exchange energy and $J'[\rho(\vec{r})]$ is the potential correlation energy. However, only the expression of $J[\rho(\vec{r})]$ is known, whereas $T[\rho(\vec{r})]$, $K[\rho(\vec{r})]$ and $J'[\rho(\vec{r})]$ are unknown.

SECOND THEOREM: *The electron density of a non-degenerate electronic ground state can be calculated determining the density that minimizes the energy of the ground state.*

The second theorem underpins that for any positive definite trial density ρ_t , the energy would be always bigger than the exact ground state energy, see equation 2.12.

$$E_o[\rho_o] \leq E_v[\rho_t] \quad (2.12)$$

In spite of the breakthrough of Hohenberg and Kohn theorems, a functional expression for $T[\rho(\vec{r})]$, $K[\rho(\vec{r})]$ and $J'[\rho(\vec{r})]$ terms could not be determined. The first solution of this problem appeared in 1965.

2.2.2.1 Kohn-Sham Method

Kohn-Sham proposed⁹⁶ in 1965 the first approach to solve the lack of knowledge about the $T[\rho(\vec{r})]$, $K[\rho(\vec{r})]$ and $J'[\rho(\vec{r})]$ functionals. The principal progress was to discover a simple way to define the Hamiltonian operator, considering a system of non-interacting electrons. This approach introduces a fictitious system of N non-interacting electrons to be described by a set of mono-electronic wavefunctions ϕ_i , assuming that the density of its ground state is the same as the density of an interacting electron system. So, the kinetic functional $T_s[\rho]$, and the electronic density can be obtained following equations 2.13 and 2.14.

$$T_s[\rho] = -\frac{1}{2} \sum_{i=1}^N \langle \phi_i | \nabla_i^2 | \phi_i \rangle \quad (2.13)$$

$$\rho(\vec{r}) = \sum_{i=1}^N |\phi_i(\vec{r})|^2 \quad (2.14)$$

In the equation 2.13 the suffix s , indicates that this is not the real kinetic energy, but the kinetic energy of a non-interacting electron system.

Thereby, the electronic energy expression of the ground state can be rearranged as indicated by equation 2.15, being the general DFT energy expression.

$$E_{DFT}[\rho(\vec{r})] = T_s[\rho(\vec{r})] + \int \rho(\vec{r}) V_{ne}(r) dr + J[\rho(\vec{r})] + E_{xc}[\rho(\vec{r})] \quad (2.15)$$

where the new term introduced is the exchange-correlation functional $E_{xc}[\rho(\vec{r})]$, see equation 2.16.

$$E_{xc}[\rho(\vec{r})] = (T[\rho(\vec{r})] - T_s[\rho(\vec{r})]) + (V_{ee}[\rho(\vec{r})] - J[\rho(\vec{r})]) \quad (2.16)$$

which is a sum of the kinetic correlation energy and the error made in treating the electron-electron interaction classically. The fundamental aspect underpinning DFT theory is to find the best expression for the exchange-correlation functional, for which the exact form is unknown. Nevertheless, several DFT methods have been developed to obtain an approximated expression for the exchange-correlation functional,⁸¹ such as the Local Density Approximation (LDA), the Local Spin Density Approximation (LSDA), the Non-local Corrections or Generalized Gradient Approximations (GGA), the Meta-GGA approximations and the hybrid exchange functional (used in this thesis).

2.2.2.2 Hybrid Exchange Functional

The principle behind the hybrid exchange method is based on combining Hartree-Fock corrections with the exchange-correlation functional $E_{xc}[\rho]$. The way to include the exact exchange derived from a HF calculation is obtained from the so-called *Adiabatic Connection Formula* (ACF).⁸⁵ The ACF connects the non-interacting and the fully interacting states (Eq.2.17).

$$E_{xc}[\rho] = \int_0^1 W_{xc}[\lambda] d\lambda \quad (2.17)$$

where $W_{xc}[\lambda]$ represents the exchange-correlation energy of the electronic part of a interacting polyelectron system, and λ is the coupling constant (which takes values from 0 to 1). At the limit of $\lambda = 0$ the electrons of the system do not interact with each other, resulting in an exact exchange at the HF level. However, in the $\lambda = 1$ limit the electrons of the system interact, contributing to the exchange-correlation energy. Then, on the basis of equation 2.17 an approximation can be applied. In 1993 Becke⁹⁷ proposed an approximation to calculate the exchange-correlation energy, in which $W_{xc}[\lambda]$ presents a linear dependency on λ leading to equation 2.18.

$$E_{xc}[\rho] = \frac{1}{2} E_{xc}^{DFT} + \frac{1}{2} E_x^{HF} \quad (2.18)$$

where $E_{xc}^{DFT} = W_{xc}^{\lambda=1}[\lambda]$ represents the exchange-correlation energy calculated by a DFT method, and $E_x^{HF} = W_{xc}^{\lambda=0}[\lambda]$ represents the exact exchange energy calculated by the HF method.

One of the better known hybrid functionals is B3LYP.⁹⁸ This functional was created by Becke, and Lee, Yang and Parr. *B3* makes reference to the development of Becke's 3-parameter exchange correlation functional⁹⁹ (Eq.2.19). *LYP* makes reference to the development

of Lee, Yang and Parr's correlation functional¹⁰⁰ that recovers dynamic electron correlation (Eq.2.19).

$$E_{xc}^{\text{B3LYP}} = (1 - a_0)E_x^{\text{LSDA}} + a_0E_x^{\text{HF}} + a_x\Delta E_x^{\text{B88}} + a_cE_c^{\text{LYP}} + (1 - a_c)E_c^{\text{VWN}} \quad (2.19)$$

where the values $a_0 = 0.2$, $a_x = 0.72$ and $a_c = 0.81$ are suggested by Becke, E_x^{LSDA} is the standard local exchange functional, E_x^{HF} is the exact (Hartree-Fock) exchange functional, ΔE_x^{B88} is the Becke's gradient correction to the exchange functional but uses LYP for the correlation functional. Since LYP does not have an easily separable local component, the (E_c^{VWN}) expression, called the local correlation functional of Vosko, Wilk and Nusair (VWN),¹⁰¹ has been used to provide the different coefficients of local and gradient corrected correlation functionals. It is also important to emphasize that other relevant hybrid functionals exist, such as B3PW91, MPW1K and PBE0.⁸⁵

2.3 Hybrid QM/MM Method

The hybrid Quantum-Mechanics/Molecular-Mechanics (QM/MM) method is a theoretical approach that combines Quantum Mechanics (QM) methods and Molecular Mechanics (MM) methods, enabling the description of catalytic reactions in very large enzymes with a reasonable computational effort and accuracy. In 1976¹⁰² Warhsel and Levitt presented the first QM/MM calculation of an enzymatic reaction. However, the QM/MM approach was not widespread accepted until 1990 with the paper published¹⁰³ by Field, Bash and Karplus, describing in detail the coupling of QM methods with MM methods. In the same paper an evaluation of the accuracy and effectiveness of the method against *ab initio* calculations and experimental data was

shown. Over twenty years of research, the QM/MM methods have been used to model hundreds of systems taking the environment into account to achieve a better understanding of their molecular and chemical properties. Numerous reviews and articles have been published validating the QM/MM approach not only in biomolecular^{104, 105} systems, but also in organometallic^{106, 107}, solid-state¹⁰⁸ systems and in processes with explicit solvent¹⁰⁹. For that reason, in 2013 the Nobel Prize in chemistry was awarded to Martin Karplus¹¹⁰, Michael Levitt¹¹¹ and Arieh Warshel¹⁰² for the development of multiscale models for complex chemical systems.

2.3.1 QM/MM energy expression

To begin with, it is important to know how the QM/MM methods treat the complete system (**S**). The system is divided into two regions: the QM region or inner region (**I**) and the MM region or outer region (**O**) (Fig.2.1). The QM method is applied to accurately model the electronic-structure of the inner region, while the MM method is employed to model the surrounding region without an explicit representation of electrons. Owing to the fact that the complete system is considered as a whole, the potential energy of the entire system cannot be simply written as the sum of the energies of the QM and MM contributions. Therefore, QM-MM interactions have to be considered.

The coupling terms are defined by the boundary region, where a special caution is needed with the covalent bonds between the subsystems (see section 2.3.2). QM/MM schemes (Fig.2.1) can be classified into two different approaches according to their total energy expression: the Subtractive and the Additive QM/MM schemes.

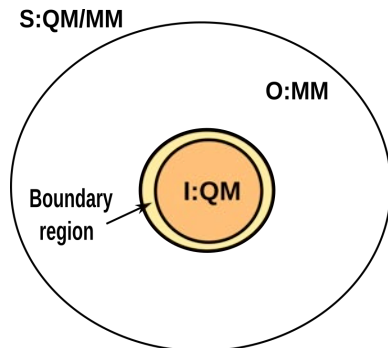


Figure 2.1: Segmentation of the entire system (**S**) into the inner (**I**) and the outer (**O**) regions, considering the yellow ring around the inner region as the boundary region.

2.3.1.1 Subtractive QM/MM scheme

In the subtractive scheme, the QM/MM potential energy expression is the sum of the MM energy of the total system ($E_{\text{MM}}(\mathbf{S})$) and the QM energy of the inner subsystem ($E_{\text{QM}}(\mathbf{I})$), subtracting the MM energy of the inner subsystem ($E_{\text{MM}}(\mathbf{I})$) to avoid double counting. The final expression is given in equation 2.20.

$$E_{\text{QM/MM}}^{\text{sub}}(\mathbf{S}) = E_{\text{MM}}(\mathbf{S}) + E_{\text{QM}}(\mathbf{I} + \mathbf{L}) - E_{\text{MM}}(\mathbf{I} + \mathbf{L}) \quad (2.20)$$

As it is formulated in equation 2.20 all the calculations on the inner region are performed including the link atoms (**L**) to become a capped inner system (**I+L**). Theoretically, the subtractive scheme can be considered an MM approach in which a small part of the system is treated at the QM level and no explicit QM-MM coupling terms are needed. This simplicity makes the implementation relatively straightforward and it is considered the main advantage of the subtractive approach. Moreover, the link atom artifacts are corrected by the subtraction, as long as the MM energy terms involving the link atoms reproduce the

QM potential reasonably well. However, the coupling between the QM and MM subsystems is treated entirely at the MM level, producing special problems with the electrostatic interactions which are represented by the Coulomb interaction between fixed atomic charges in the QM and MM regions. This also means that the inner region must have a complete set of MM parameters to perform the MM calculation of the total system and the inner subsystem. An example of this scheme is the ONIOM (*Our N-layered Integrated Molecular Orbital and Molecular mechanics*) approach^{112, 113} (see section 2.5).

2.3.1.2 Additive QM/MM scheme

In the additive scheme, the QM/MM total energy expression of the entire system is the sum of the MM calculation of the outer subsystem, $E_{\text{MM}}(\mathbf{O})$, the QM calculation of the inner subsystem, $E_{\text{MM}}(\mathbf{I})$, and the explicit QM-MM interactions, $E_{\text{QM-MM}}(\mathbf{I}, \mathbf{O})$, which gives equation 2.21.

$$E_{\text{QM/MM}}^{\text{add}}(\mathbf{S}) = E_{\text{MM}}(\mathbf{O}) + E_{\text{QM}}(\mathbf{I} + \mathbf{L}) + E_{\text{QM-MM}}(\mathbf{I}, \mathbf{O}) \quad (2.21)$$

As it is formulated in equation 2.21 the QM calculation on the inner region is performed including the link atoms (\mathbf{L}) to become a capped inner system ($\mathbf{I} + \mathbf{L}$). As opposed to the subtractive scheme, in the additive scheme the outer subsystem is the only region calculated at the MM level. The explicit coupling term¹⁰⁴, $E_{\text{QM-MM}}(\mathbf{I}, \mathbf{O})$, is the sum of the bonded (when present), van der Waals, and electrostatic interactions terms between the QM and MM atoms, see equation 2.22.

$$E_{\text{QM-MM}}(\mathbf{I}, \mathbf{O}) = E_{\text{QM-MM}}^{\text{b}} + E_{\text{QM-MM}}^{\text{vdW}} + E_{\text{QM-MM}}^{\text{elect}} \quad (2.22)$$

where $E_{\text{QM-MM}}^{\text{b}}$ represents the energy of the bonded interactions, $E_{\text{QM-MM}}^{\text{vdW}}$ the energy of the van der Waals interactions and $E_{\text{QM-MM}}^{\text{elect}}$ the energy of the electrostatic interactions.

The *bonded interactions* represent the bond stretching, angle bending and torsional interactions between the QM atoms and MM atoms and are described using the standard MM parameters.

The *van der Waals interactions* account for the coupling between all atoms of the QM region and every atom of the MM region. In particular, the $E_{\text{QM-MM}}^{\text{vdW}}$ only considers pairs of atoms, one from the QM and the other from the MM region. The van der Waals parameters of the QM atoms of the inner region are described by the Lennard-Jones potential of the FF (Eq.2.2). Nevertheless, the atoms of the inner region can change their character along a reaction path. These complications, in practice, are alleviated by the short-range nature of the van der Waals interaction, due to the fact that only those atoms closest to the boundary contribute significantly to the van der Waals interaction term. Then, to minimize the possible errors concerning to non-optimum Lennard-Jones parameters, the QM-MM boundary may be placed further away from the QM atoms involved in the reaction.

The *electrostatic interactions* represent the coupling between the QM charge density and the charge model employed in the MM region. The accuracy of the description of electrostatic embedding is essential for a realistic modeling of biomolecules. For that reason, three different electrostatic schemes have been developed according to the degree of polarization: the mechanical embedding, the electrostatic embedding and the polarized embedding.

- MECHANICAL EMBEDDING

The electrostatic QM-MM interactions are considered as electrostatic MM-MM interactions, in which the point charge model at classical level (typically rigid atomic point charges) is applied to the QM region. Theoretically, this type of interaction is simple and computationally efficient. However, it presents some disadvantages and restrictions: (i) the QM density is not directly polarized by the electrostatic environment; (ii) some discontinuities appear in the PES when the charge distribution in the QM region changes (typically during a reaction) and (iii) it presents problems in the derivation of proper MM charges for the inner region which not necessary reproduce the true charge distribution of the inner region.

- ELECTROSTATIC EMBEDDING

In contrast, according to this approach the electrostatic QM-MM interactions are treated at the QM level. The MM charges in the QM calculation are included as a mono-electronic terms in the QM Hamiltonian, see equation 2.23 in a.u units.

$$\hat{H}_{\text{QM/MM}}^{\text{el}} = - \sum_i^N \sum_{J \in \mathbb{O}}^L \frac{q_J}{|\mathbf{x}_i - \mathbf{X}_J|} + \sum_{\alpha \in \mathbb{I}+L}^M \sum_{J \in \mathbb{O}}^L \frac{q_J Q_\alpha}{|\mathbf{X}_\alpha - \mathbf{X}_J|} \quad (2.23)$$

where q_J are the MM point-charges located at \mathbf{X}_J , the Q_α are the nuclear QM charges at \mathbf{X}_α and \mathbf{x}_i designate electron positions. Indexes i , J , and α are linked to the N electrons, L point charges, and M QM nuclei, respectively. This type of polarization is more accurate and solves the restrictions of the mechanical embedding scheme: (i) the QM density is automatically polarized by the environment, (ii) the QM electronic structure adapts to the changes in the charge distribution of the environment and (iii) no

charge model needs to be derived for the QM region. However, the incorporation of the electrostatic embedding scheme not only requires a higher computational cost, but also requires a special care at the QM-MM boundary (section 2.3.2) to avoid overpolarization. These problems become notable when the boundary crosses a covalent bond. Aside from this, the electrostatic embedding scheme is the most well-liked embedding approach for biomolecular applications.

- POLARIZED EMBEDDING

The electrostatic QM-MM interactions include a flexible MM charge model polarized by the QM charge distribution. This polarization scheme allows the mutual polarization with a self-consistent formulation that includes the polarizable MM model into the QM Hamiltonian.

An example of the application of this additive QM/MM scheme is the current version of Chemshell Software^{114, 115} (see section 2.4).

2.3.2 QM-MM Boundary schemes

The Boundary scheme model deals with the treatment of the atoms at the boundary between the QM and MM regions, specially with covalent bonds that cross the QM-MM boundary. The main objective of the QM-MM boundary consists of defining the better QM and MM subsystems. This is easier if the boundary does not cross covalent bonds. However, in many cases it is unavoidable that the QM-MM boundary cuts a covalent bond; for instance, in an enzymatic reaction that involves a metal coordinated to several ligands or a long substrate. In these cases, three issues have to be taken into account: (i) the drooped bond of the QM atom has to be treated as in an homolitic

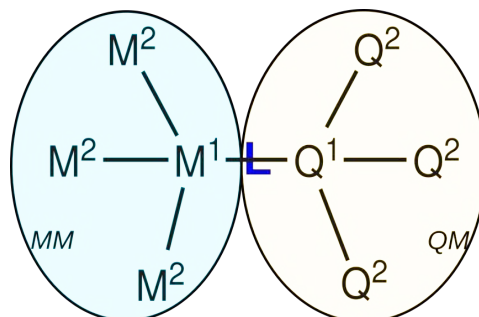


Figure 2.2: Representation of a covalent bond that crosses the QM-MM boundary using the link-atom scheme. L represents the link atom and Q and M the atoms at the QM and MM regions, respectively. The yellow area represents the atoms included in the inner region, whereas the blue area includes the atoms of the outer region.

breakage, (ii) the overpolarization of the QM density by the MM point-charges close to the boundary has to be prevented for electrostatic or polarized embedding, especially using the link-atom scheme, and (iii) it is important to achieve a well-balanced description of the QM-MM interactions at the border, avoiding double-counting of interactions and selecting the correct bonded QM/MM terms that involve atoms from both subsystems. Currently, there are two main different classes of boundary schemes: the link-atom and the localized-orbital scheme.

- LINK-ATOM SCHEME

The link-atom method treats the covalent bond at the QM-MM boundary in a very simple way (see Figure 2.2). The covalent bond that crosses the boundary is divided between the inner region (QM) and the outer region (MM). Q^1 stands for the QM atom closest to the boundary, and M^1 stands for the MM atom closest to the boundary. This atom Q^1 is included in the inner region, whereas the atom M^1 is in the outer region. Consequently, on one hand, the Q^1 atom of the QM region has a free

valence, which is capped by an additional atom (L) covalently bonded. On the other hand, the bond Q^1-M^1 is described at the MM level. For that reason, QM calculations are performed on an electronically saturated system (I + L), both for an subtractive or additive scheme, see section 2.3.1.1 and 2.3.1.2. The link atom L is in most cases a hydrogen atom, but it can also be any monovalent atom or group.

However, the presence of an extra atomic center (L) creates some problems: (i) the addition of a link atom produce three degrees of freedom not introduced in the real system and (ii) as noted above, the link atom and the QM density close to the point charge of the atom M^1 will tend to overpolarize the QM density in the case of electrostatic and polarized embedding. Nevertheless, some approaches have been put forward to reduce overpolarization. One of the most commonly used is the charge-shift scheme introduced by Sherwood and co-workers^{109, 116} based on shifting/redistributing the point charges in the link region. This approach removes the partial charge from M^1 , distributed over the M^2 atoms to preserve the total charge and dipole of the MM region. There exist two more approaches, one deletes the one-electron integrals associated with the link atom, whereas the other one deletes the MM point charges in the link region from the Hamiltonian.

- FROZEN LOCALIZED-ORBITAL SCHEME

The principle behind the Frozen Localized-Orbital (FLO) consists of placing a set of orientated localized orbitals on one of the frontiers atoms and keeping some of them frozen, not participating in the SCF interactions. Some of the different schemes that share this same approach are: the Local Self-Consistent Field

(LSCF)^{117, 118}, the frozen orbitals (a variant of LSCF)^{119–121} and the Generalized Hybrid Orbitals (GHO)^{122–124}.

2.4 Chemshell Software

ChemShell is a computational chemistry modular package focused on hybrid QM/MM simulations and developed by the main author Paul Sherwood and co-workers.^{109, 114, 115} Chemshell is widely used to study large systems such as biological macromolecules and framework materials. Chemshell is programmed with Tool Command Language (Tcl) scripting language. The concept is to leave the time-consuming QM energy evaluation to external specialized codes. The software is a package to perform QM/MM calculations by combining external QM codes with an internal MM code that can calculate the MM energy according to different forcefields. For each code, Chemshell has a corresponding interface module written also in Tcl.

2.4.1 QM/MM Methodology

Chemshell, as it is mentioned before, is mainly used to perform QM/MM calculations, but it can also be used to carry out QM or MM calculations. The software divides the total system into QM and MM subsystems, interfacing the programs to perform both the QM and MM calculations. The QM codes that can be interfaced via Chemshell are for example: Gaussian¹²⁵, Turbomole, Q-Chem, MNDO, ORCA, etc. to define the QM region. On the other hand, DL-POLY¹²⁶ is an internal module of Chemshell developed by W. Smith. DL-POLY is the MM code that can run with difference forcefields such as CHARMM and AMBER to define the MM region. The module is programmed to convert the parameters and topology files from AMBER and CHARMM

format, for instance, into the internal format suitable for calculations with DL-POLY.

Chemshell uses the additive QM/MM scheme (see section 2.3.1.2) by default, but it also presents the subtractive QM-MM scheme (see section 2.3.1.1) as an alternative.¹¹⁵

In this thesis Gaussian and DL-POLY have been used to perform the QM and MM calculations, respectively, considering the electrostatic embedding scheme.

2.4.2 Geometry Optimization

Chemshell has been chosen in this thesis to characterize the chemical reaction paths by using geometric optimization algorithms. Chemshell presents some of those algorithms incorporated in different modules of the codes such as HDLCopt¹²⁷ and the most recently developed DL-FIND¹²⁸.

- **HDLCopt** or Hybrid Delocalised internal Coordinate optimizer was developed by Alex Turner and Salomon Billeter, as part of the QUASI project.¹⁰⁹ The optimizer was designed to explore potential energy surfaces, to locate energy minima and to carry out Transition State (TS) searches, for macromolecular systems with thousands of atoms that participate in an enzymatic reaction. The HDLCopt¹²⁷ optimizer is composed of two principal optimizer algorithms: the Limited-memory Broyden-Fletcher-Goldfarb-Shanno (L-BFGS)¹²⁹ optimizer and the Partitioned Rational Function Optimizer (P-RFO)¹³⁰. The L-BFGS is used for linear scaling geometry optimization, and the P-RFO for TS searches. Furthermore, the optimizer also presents the microiterative optimization scheme.¹³¹ The last feature that must be highlighted of this optimizer is related with the generation of HDLC

as the coordinate system use for efficient geometry optimizations. To do so, the system is split up into several residues. Internal coordinates are defined and delocalized within each residue, and the relative position of those residues are defined in Cartesian coordinates.

- **DL-FIND** optimizer was developed by Johannes Kästner and Tom Keal¹²⁸ as an improvement of the HDLCopt module. DL-FIND supports a wide variety of optimization methods. The module was designed to apply the different algorithms to explore potential energy surfaces, to locate minima, to search for TSs (specially using the dimer method). Furthermore, the module also includes an algorithm to perform a constrained minimization to a conical intersection and the nudged elastic band (NEB) method to characterize reaction paths.

In this thesis the HDLCopt optimizer has been chosen to perform the QM/MM calculations, according to the Chemshell version 3.4.2 in which DL-FIND optimizer was under development.

2.5 Gaussian's ONIOM method

ONIOM stands for *Our own N-layered Integrated molecular Orbital and molecular Mechanics*.¹¹³ ONIOM is a computational approach developed by Morokuma group and co-workers¹³² that was launched for the first time as a Gaussian's method in its version 98. Nevertheless, it was not until Gaussian 03¹³³ when ONIOM was applied to study large systems of chemical and/or biological interest, such as enzymes. ONIOM is a hybrid method based on a subtractive scheme (see section 2.3.1.1) that enables different *ab initio*, DFT, semiempirical methods or MM

methods to be combined to produce reliable energies and geometry optimizations at reduced computational time.

2.5.1 QM/MM Methodology

ONIOM approach usually divides the total system into three systems called: the small model (SM) system, the intermediate (I) system and the real (R) system. In a more simplify approach there are only two systems: the SM and the R system. The energy of each system is calculated at a different level of theory, being the energy calculation less accurate as the system becomes larger. These levels of energy are called: the high level, the medium level and the low level. The most commonly used ONIOM method is a two-layer scheme known as ONIOM2. If the ONIOM2 method combines an MM method with a QM method, the approach is denominated ONIOM2(QM:MM), but if two QM methods are combined, the approach is called ONIOM2(QM1:QM2).

In this thesis, the ONIOM2(QM:MM) model is used to obtain the energy of the system and it is expressed following the equation 2.24.

$$E^{\text{ONIOM}} = E_{\text{R}}^{\text{low}} + E_{\text{SM}}^{\text{high}} - E_{\text{SM}}^{\text{low}} \quad (2.24)$$

where E^{ONIOM} is the energy of the system, $E_{\text{R}}^{\text{low}}$ corresponds to the energy of the real system (or total system) at the low level using an MM method, $E_{\text{SM}}^{\text{high}}$ is the energy of the small model system at the high level using a QM method, and $E_{\text{SM}}^{\text{low}}$ represents the energy of the small model system at the low level using an MM method. However, as it is referred in section 2.3.1.1, the subtractive scheme does not present an explicit QM-MM coupling term, causing special problems with the electrostatic interactions. Thus, in the original ONIOM method only the mechanical embedding (ME) scheme was implemented. So, the

polarization of the QM region by the MM environment system was not included yet. Later on, the electrostatic embedding (EE) scheme was implemented in ONIOM developed by Vreven et al.¹³⁴ for the Gaussian program. Nevertheless, the additive QM/MM coupling term (section 2.3.1.2), where the electrostatic embedding (QM/MM-EE) is included, is not identical as the ONIOM-EE method implementation (Eq.2.25).

The QM/MM-EE only incorporates the MM point charges as a mono-electronic term into the QM Hamiltonian (Eq.2.23). In contrast, in the ONIOM-EE embedded approach the MM point charges are included in both, the $E_{\text{SM}}^{\text{high,v}}$ and $E_{\text{SM}}^{\text{low,v}}$ terms (Eq.2.25). Then, the expression of the Hamiltonian of the QM small model $H_{\text{SM}}^{\text{high,v}}$, follows the equation 2.26.

$$E_{\text{ONIOM-EE}} = E_{\text{R}}^{\text{low}} + E_{\text{SM}}^{\text{high,v}} - E_{\text{SM}}^{\text{low,v}} \quad (2.25)$$

$$H_{\text{SM}}^{\text{high,v}} = H_{\text{SM}}^{\text{high}} - \sum_i \sum_n \frac{S_n q_n}{r_{i,n}} + \sum_j \sum_n \frac{Z_j S_n q_n}{r_{j,n}} \quad (2.26)$$

where n , j , and i refers to the point charges of the MM region, QM atoms and QM electrons, respectively. q_n is point charge in the environment system and S_n is a scale factor for the MM atom n , which is essentially 1 for most point charges. Z_j corresponds to the nuclear charge of the QM atom j . Finally, $r_{i,n}$ represents the distance between a QM electron and a point charge of the environment system and $r_{j,n}$ is the distance between a SM atom and a point charge of the environment system.

The $E_{\text{SM}}^{\text{Low},v}$ term is expressed following the equation 2.27

$$E_{\text{SM}}^{\text{Low},v} = E_{\text{SM}}^{\text{Low}} + \sum_j \sum_n \frac{q_j S_n q_n}{r_{j,n}} \quad (2.27)$$

where here j corresponds to an atom of SM model, and the rest variable are the same just as equation 2.26. Finally, in ONIOM the link-atom approach (see section 2.3.2) is also employed by default to deal with the boundary between QM and MM region.

2.5.2 Geometry Optimization

The geometry optimization of the minimum energy structures and the transition state structures is essential to understand the mechanism of a chemical reaction. The ONIOM method presents two main optimizer methods: the macro/microiteration method, and the quadratically coupled method.

- **Macro/microiteration Method** is an efficient hybrid optimization ONIOM2(QM:MM) method for large systems.¹³⁵ The method carries out two separate iterative optimizations: i) an MM optimization with microiteration steps of the real system is performed, fixing the small model system. ii) an expensive QM optimization with macroiteration steps of the small model system is performed, fixing the rest of the system. Such strategy is repeated until the gradient of the total system converges to a specific threshold. The optimizer allows to use two different algorithms for each optimizer method. A memory-demanding second-order algorithm, such as Newton-Raphson (NR) or rational function optimization (RFO), is used to optimize the small model system, at the QM level. On the other hand, a first-order

algorithm, such as steepest descent or conjugate gradient optimization, is applied to the real system at the MM level.

- **Quadratically Coupled Method** is a geometry optimization scheme developed and implemented by Vreven et al.¹³⁶ in Gaussian. The quadratically coupled ONIOM2(QM:MM) optimizer includes an explicit Hessian coupling between the small model system and the real system in the macroiteration steps (at the QM level). Such approach reduces the expensive macroiteration optimization, improves optimization stability, and facilitates to converge to closer local minima.

In this thesis the Quadratically Coupled optimizer has been chosen to perform the QM/MM calculations, including in the ONIOM2(QM:MM) model the electrostatic embedding scheme.

2.6 Molecular Dynamics Simulations

In terms of computational chemistry, as it is said in the literature,⁸¹ *Simulation* refers to methods aimed at producing representative structures of a system at a finite temperature. Based on this concept there exist two major techniques: Monte Carlo and Molecular Dynamics. This thesis is focused on working with Molecular Dynamics simulations for biomolecules.

Firstly, it must be recalled that the Born-Oppenheimer approximation have been assumed. So, a classical approach to describe the movement of nuclei on a potential energy surface is called in this work Molecular Dynamics (MD). Then, a MD simulation is a computational time-dependent method which allows to study different dynamic features of biological systems of up to millions of atoms, such as conformational sampling. The first outbreak of MD was performed by Alder

and Wainwright in 1957,¹³⁷ with the study of a condensed phase system using a hard-sphere model.¹³⁷ It was not until the latest '70s when the first simulation of a system of several hundreds of atoms, like an entire protein in solution, was executed¹³⁸ by McCammon, Gelin and Karplus.

Simulations of huge biological systems with 50.000 - 100.000 atoms is now routine, and even systems of 500.000 atoms are now commonly simulated by MD if the appropriate computer facilities are available. These improvements over the last years have been the consequence of the use of High Performance Computing (HPC)¹³⁹ and the MD algorithms computed in parallel that have greatly speed-up the simulations. In addition, the use of graphical processing units (GPUs)¹⁴⁰⁻¹⁴² has increased several folds the simulation time.

2.6.1 MD algorithm

The principle behind the MD algorithm is based on propagating in time an initial set of coordinates and velocities (a trajectory) according to Newton's equations of motion as is shown in equation 2.28.

$$\vec{F}_i(\vec{r}_i, \dots, \vec{r}_n) = -\frac{dV}{d\vec{r}_i} = m_i \frac{d^2\vec{r}_i}{dt^2} \quad (2.28)$$

where \vec{r}_i and m_i represent the position and the mass of atom i , respectively. The left-hand side represents the force upon an atom \vec{F}_i , which is applied in a large system of N particles whose potential energy is V . The most simple approach consist of calculating the potential energy surface by using the forcefield equation. However, the Newtonian equations do not have an analytical solution. Under such situation the equations are integrated using a finite difference method.

The principal idea is carried out the integration in many small steps, being the force constant within in each time step. There exist

many different algorithms for integrate the Newton's equations, and all of them approximate the positions and velocities of the system of N atoms to Taylor series expansions.

The *Verlet algorithm*¹⁴³ has been one of the most widely used methods for numerically solving the Newtonian equations. However, the algorithm has two main drawbacks: i) the new positions obtained lead to truncation errors, and ii) the velocities do not appear explicitly in the propagation equation, so preventing the generation of ensembles at constant temperature. The *leap-frog algorithm*¹⁴⁴ remedies the disadvantages of Verlet algorithm including the velocities explicitly and improving the numerical accuracy. Even so, the positions and velocities are not calculated at the same time. The *velocity Verlet algorithm*¹⁴⁵ solves this drawback of the leap-frog algorithm, being a combination of *Verlet algorithm* and *leap-frog algorithm*.

In this thesis, the forcefield implemented in AMBER code have been used to perform the Molecular Dynamics simulations with an internal module called *pmemd*,¹⁴⁶ which employs the *velocity Verlet algorithm*.

2.6.2 Protocol for the MD simulations

It is important to emphasize that biological movements spend a very wide time range. For instance, there exist very fast movements like atomic fluctuations or very slow movements like protein folding. For that reason, it is important to choose not only the correct time step, but also the best simulation protocol with the corresponding restraints or constraints to reproduce the experimental conditions.

In biomolecular simulations the fastest movements, as the C-H bond vibrations, are not usually of great interest. For that reason, the covalent bonds containing hydrogen are constrained by the SHAKE algorithm¹⁴⁷ to improve the MD calculation. In addition, some restraints

may be applied to preserve the stability of the total system along the simulation.

As regards to reproducing experimental conditions along the MD, macroscopic magnitudes must be derived. However, for such application to be possible the *Ergodic Hypothesis* must be assumed. This hypothesis establishes that in an infinite simulation a system visits all the accessible states. The most common experimental conditions simulated by MD are at constant pressure or volume, and constant temperature. Therefore, an NPT (isothermal-isobaric) and NVT (canonical) ensemble can be described by MD, allowing to study some phenomena of the system. To maintain constant T, there are two common approaches: applying Langevin dynamics,¹⁴⁸ or an external heat bath using *Berendsen algorithm*,¹⁴⁹ for instance.

2.6.3 Periodic Boundary Conditions

The Periodic Boundary Conditions (PBC) is a computational widely used technique in MD simulations.¹⁵⁰ The PBC method assumes that the solvent molecules are placed around a system inside a suitable box (unit cell) with a cubic or rectangular geometry. In a unit cell at normal density, some atoms will appear near to the external walls of the box affecting to the simulated properties. For that reason, the box is replicated in all directions, resulting in a quasi-periodic reproduction of the system. This means that, if a molecule crosses the right wall of the box, the corresponding image will appear through the left wall from the neighboring box.

Part III

Results and Discussion

Chapter 3

COX-2:AA

In this chapter, the aim is to show a global overview of the results and discussion published in the articles that compose this thesis (attached at the end of the thesis). In these articles, MD simulations and QM/MM were combined: i) to reveal the molecular details of the complete mechanism (Fig.1.6) involved in the conversion of the AA to PGG₂ catalyzed by COX-2 (see article I); ii) to discard the 10-step carbocation-based mechanism (Fig.1.7) proposed by Dean and Dean (see article I); iii) to shed light on the molecular details of the effect of the Gly526Ser mutation (see article II), and iv) to understand the formation of the main product of the AA oxidation catalyzed by aspirin-acetylated COX-2 (see article III). Additionally, more detailed results of the six-step all-radical mechanism study considering only the H_{13_{proS}} abstraction is described in Appendix A.

3.1 Insight into the all-radical mechanism

As mentioned in section 1.3.1 a general agreement exists about the mechanism that governs the enzyme reaction in the COX active site: the classical six-step all-radical mechanism. Nevertheless, most of its molecular details still remain unknown. The reaction mechanism has been studied by using MD to simulate feasible structures of the enzyme complex. However, it is not clear yet among of the scientific community, if AA occupies the COX active site before or after Tyr385 is converted into its active radical form. For that reason, in this thesis two 100 ns MD simulations of the productive AA binding to monomer B of COX-2 have been carried out: one considering Tyr385, and the other one considering the tyrosyl radical (from now on Tyr385-O•). Both MD simulations have been performed following the methodology described in the article I.

From both resulting MD simulations, the evolution of the distances H_{13proS} -OTyr385 and H_{13proR} -OTyr385 have been followed-up to study the feasibility of the first step of the mechanism, see Figure 3.1. As shown in this Figure, at the beginning of the MD trajectory, H_{13proS} is much closer to the oxygen acceptor than H_{13proR} . However, this tendency is reversed at the last 10 ns of the MD with Tyr385, and in the range between 40-80 ns of the MD with the Tyr385-O•. This unexpected tendency in the simulation with Tyr385 made us to carry out an additional 50 ns simulation, in which it was not observed any further significant variation. At this point, two unresolved questions appear: Could a productive AA structure with H_{13proR} near the oxygen acceptor be transformed by COX-2 into PGG₂?, and Could the H_{13proS} of AA be abstracted by COX-2 to produce PGG₂, as suggested by some authors^{21, 151}?

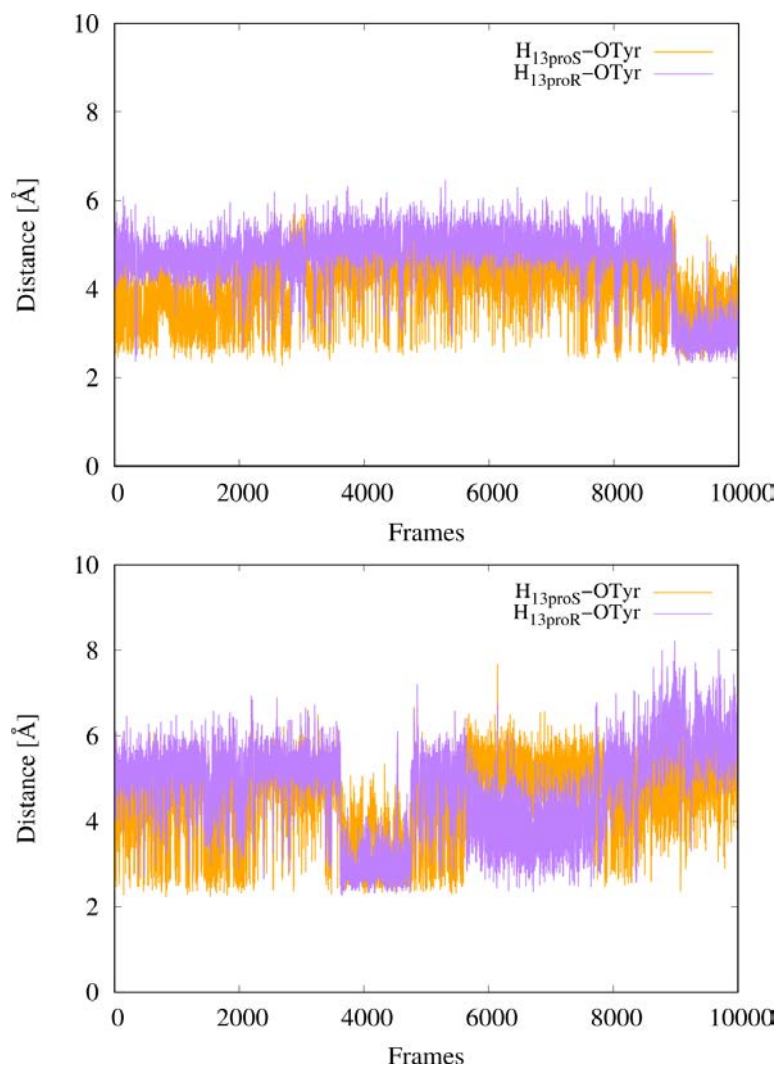


Figure 3.1: Evolution of the $H_{13proS}-OTyr385$ (orange line) and the $H_{13proR}-OTyr385$ (purple line) distances along the two 100 ns MD simulations. On top the evolution of these distances of the MD with Tyr385 is represented. On bottom the evolution of these distances of the MD with Tyr385-O• is shown. A frame has been taken each 10 ps.

In this thesis both questions were answered. This was accomplished by the complete study of the all-radical mechanism based on the calculation of the potential energy profile of each step using a QM/MM approach. First of all, the H_{13proR} abstraction is the first step, in order to prove if the formation of PGG₂ is obtained following the all-radical mechanism. For that reason, two pre-catalytic snapshots with the H_{13proR} ready to react have been taken from the MD simulation to start the reaction. Secondly, the H_{13proS} was also performed to compare if the formation of PGG₂ follows the same trend in this case. The study of six step of the mechanism, for both cases, reveals that AA undergoes various distortions to form PGG₂, being its formation viable inside the COX active site. These distortions involved different conformational changes that increase the rigidity of the substrate. This rigidity especially increases when the successive cyclizations occur, see Figure 3.2.

As seen in Figure 3.2, for both kind of abstractions, the first relevant aspect of the regio/stereoselectivity is defined in the second step of the mechanism by the entrance (antarafacial or suprafacial) of oxygen at C₁₁, and the formation of the first intermediate. The molecular analysis shows that the antarafacial entrance of oxygen at C₁₁ is crucial to obtain the correct 11R stereochemistry (see Table A.2 in the appendix for the H_{13proS} results). Nevertheless, the corresponding potential energy barriers of the suprafacial entrance are not always higher than the antarafacial ones. For instance, the O₂ addition at C₁₁ from the abstraction of the H_{13proR} is an example (see Table 2 of article I). With regards to the two subsequent cyclization steps, the formation of the endoperoxide bridge and the formation of the cyclopentane ring are determinant steps to obtain the correct stereochemistry of PGG₂.

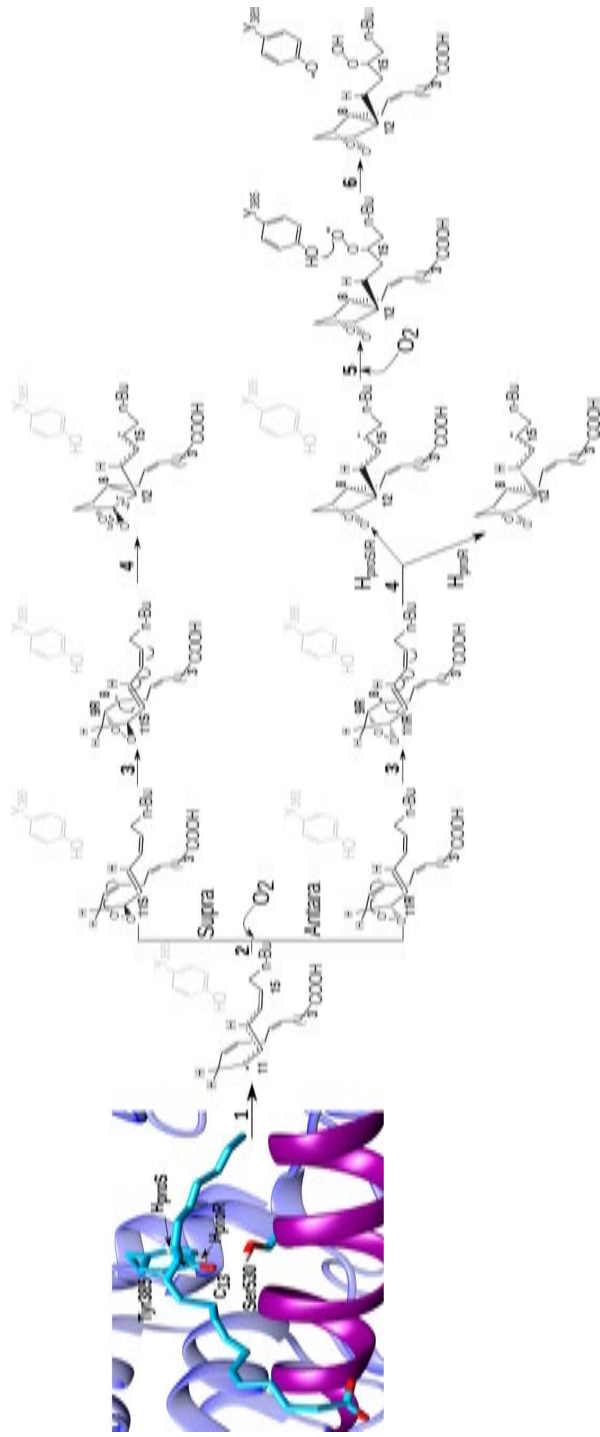


Figure 3.2: The regio/stereoselectivity of the six-step all-radical mechanism inside COX-2. The wavy lines represent the breaking of the bonds.

In this study on one hand, the correct stereochemistry of the endoperoxide bridge (9R, 11R) has been obtained from the oxygen antarafacial attack initiated from H_{13proR} as well as H_{13proS} abstractions (see Table A.3 for the H_{13proS} results).

On the other hand, the formation of two possible isomers as a result of the 8,12-cyclization: the cis ring and the trans ring isomers have been obtained by the oxygen antarafacial entrance from a H_{13proR} abstraction, being the trans the most favorable one, see article I. In contrast, only the formation of the trans ring isomer has been directly obtained by the oxygen antarafacial entrance from a H_{13proS} abstraction (see Table A.4). Conversely, for both cases, the bicyclo endoperoxide intermediate and the subsequent PGG₂ are discarded for the oxygen suprafacial entrance because the 8,12 cyclization leads to the breakage of the O–O and the C₁₁–C₁₂ bonds (Fig.3.2).

The bicyclo endoperoxide trans ring isomer is the most favorable according to our calculations, just as it has been observed experimentally.⁵¹ However, our results show two possible environments around the two isomers obtained for the 8,12-cyclization in the active site of the COX-2. Interestingly, the bicyclo endoperoxide isomers (trans and cis) are stabilized by completely different residues, see Figure 3.3. This Figure clearly shows that the bicyclo endoperoxide trans isomer is turned inside the cavity in such a way that the endoperoxide bridge interacts with Leu352, Trp387 and Phe518, and C₁₀ is near Gly526 and Leu384. Otherwise, the bicyclo endoperoxide cis isomer adopts another position, in which the endoperoxide bridge only interacts with Val349, Tyr348 and Leu352, and C₁₀ moves far away from Gly526, but gets closer to Phe518.

Finally, the last two steps: the addition of O₂ to C₁₅ starting from the optimized C₁₃–C₁₅ allyl radical trans ring isomer, and the back hydrogen transfer from Tyr385 to the peroxy radical at C₁₅ have been

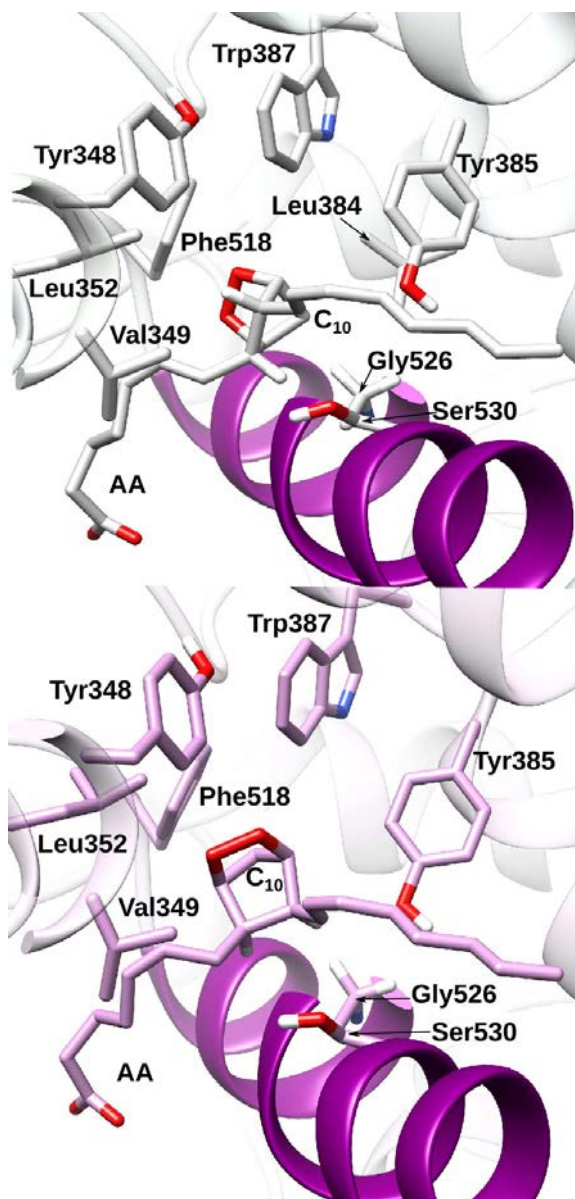


Figure 3.3: The residues of the reaction channel for the 8,12-cyclization in COX-2. On top the environment of the bicyclo endoperoxide trans isomer is represented. On bottom the environment of the bicyclo endoperoxide cis isomer is represented. The hydrogens of C_8 and C_{12} are pictured to highlight the difference of trans and cis isomers.

performed starting only from the H_{13proR} abstraction. Then, the formation of the 15 hydroperoxide group is achieved by the combination of both steps, being the potential energy barriers of the 15S stereochemistry more favorable than the 15R one. Even though these two steps have not been performed starting from the H_{13proS} abstraction, the optimized C_{13} – C_{15} allyl radical trans ring isomer for both cases presents the same arrangement, see Figure A.1. This fact probably means that the 15S stereochemistry could also be more favorable than the 15R one.

Finally, all these results indicate that there only exist one molecular mechanism that COX-2 employs to catalytically control the regioselectivity and stereoselectivity of the formation of the PGG₂. This molecular mechanism consists of the abstraction of H_{proS} or H_{proR} (being the former the most favorable), the antarafacial entrance of the oxygen at C_{11} , the subsequent formation of the (9R, 11R) endoperoxide bridge, the formation of trans cyclopentane ring isomer, and the formation of the 15S hydroperoxide group.

3.2 Carbocation-Based Mechanism

In contrast to the six-step all-radical mechanism, in this thesis also the 10-step carbocation based mechanism has been studied, see article I. As mentioned in the Introduction, the study of this mechanism is needed because its validity has recently been proposed in spite of the general agreement in the all-radical mechanism.

The obtained results are completely different to the all-radical mechanism ones. On one hand, the sigmatropic hydrogen transfer from C_{10} to C_{13} , giving a delocalized C_8 – C_{12} pentadienyl radical proposed by Dean and Dean clearly discards the carbocation based mechanism

within COX-2-cavity. The huge potential energy barrier calculated within the enzyme in this step, brushes aside the possibility of the rearrangement of AA that is involved in the hydrogen transfer from C₁₀ to C₁₃. On the other hand, the formation of 10,10-difluoro-11S-hydroxyeicosatetraenoic acid instead of PGG₂ is already explained by the all-radical mechanism, the carbocation-based mechanism not being needed.

All this demonstrates that the all-radical mechanism is the catalytic mechanism to produce PGG₂ and the carbocation-based mechanism can be clearly discarded.

3.3 Gly526Ser Mutation

As explained in section 3.1, the participant residues in the fourth step of the all-radical mechanism are crucial to form the bicyclo endoperoxide trans ring isomer and the subsequent PGG₂. For that reason, the experimental results of the G526S COX-2 mutant have been of great interest to this thesis, because although the first three reaction steps of the COX-2 mechanism (Fig.1.6) and the G526S COX-2 mechanism (Fig.1.9) are the same, its in the 8,12-cyclization step that both mechanism differ.

Schneider et al.⁶⁰ proposed that the 8,12-cyclization in the G526S mutant is sterically hindered by misalignment of the substrate carbon chain. This proposal is not compatible with the position of the 9,11-endoperoxide intermediate obtained from our calculations in the all-radical mechanism inside COX-2. Therefore, in this thesis a theoretical study is performed to shed light on the molecular details of the effect of such mutation. These calculations will provide more information of the protein residues that make easier the 8,12-cyclization in the active

site of the COX-2, see article II.

First of all, the G526S mutation is performed. Then, the equilibration of the new Ser526 residue inside the enzyme is achieved by an MD simulation. Surprisingly, at the end of the equilibration a hydrogen bond between the OH group of Ser526 and the oxygen atom of the backbone of Met522 is formed. This reveals the first conformational difference between the active site of the COX-2 and the G526S COX-2 mutant.

Thereafter, the reaction mechanism has been studied by performing first a 100 ns MD in order to simulate feasible structures to initiate the reaction. From the MD simulation it is observed that inside the G526S binding pocket AA adopts the same "L-shaped" productive binding configuration, just as in COX-2. This configuration presents the C₁₃ carbon atom and the H_{13_{proS}} atom near the phenolic oxygen of Tyr385. Therefore, from the resulting MD simulation only the evolution of the distance H_{13_{proS}}-OTyr385 has been followed-up to study the feasibility of the first step of the mechanism. Then, one pre-catalytic snapshot has been selected from the MD simulation to study the mechanism of the G526S COX-2 mutant (Fig.1.9) by the calculation of the potential energy profile of each step using a QM/MM approach.

As expected, the study of each step reveals that AA undergoes through the first three reaction steps, leading to the C₈-radical cyclic endoperoxide intermediate, just as in COX-2, see Figure 3.4. However, our calculations shown that the regioselectivity of the 9,11-endoperoxide intermediate inside the mutant can not be the (9R, 11R) configuration, as the COX-2 does. This fact is an important difference between both mechanisms, due to the fact that the bicyclo endoperoxide intermediate is not able to form, so confirming the experimental finding by Schneider et al.⁶⁰. Instead of the formation of the cyclopentane ring, a hydrogen transfer from C₁₁ to C₈, followed by the breakage of the O–O bond

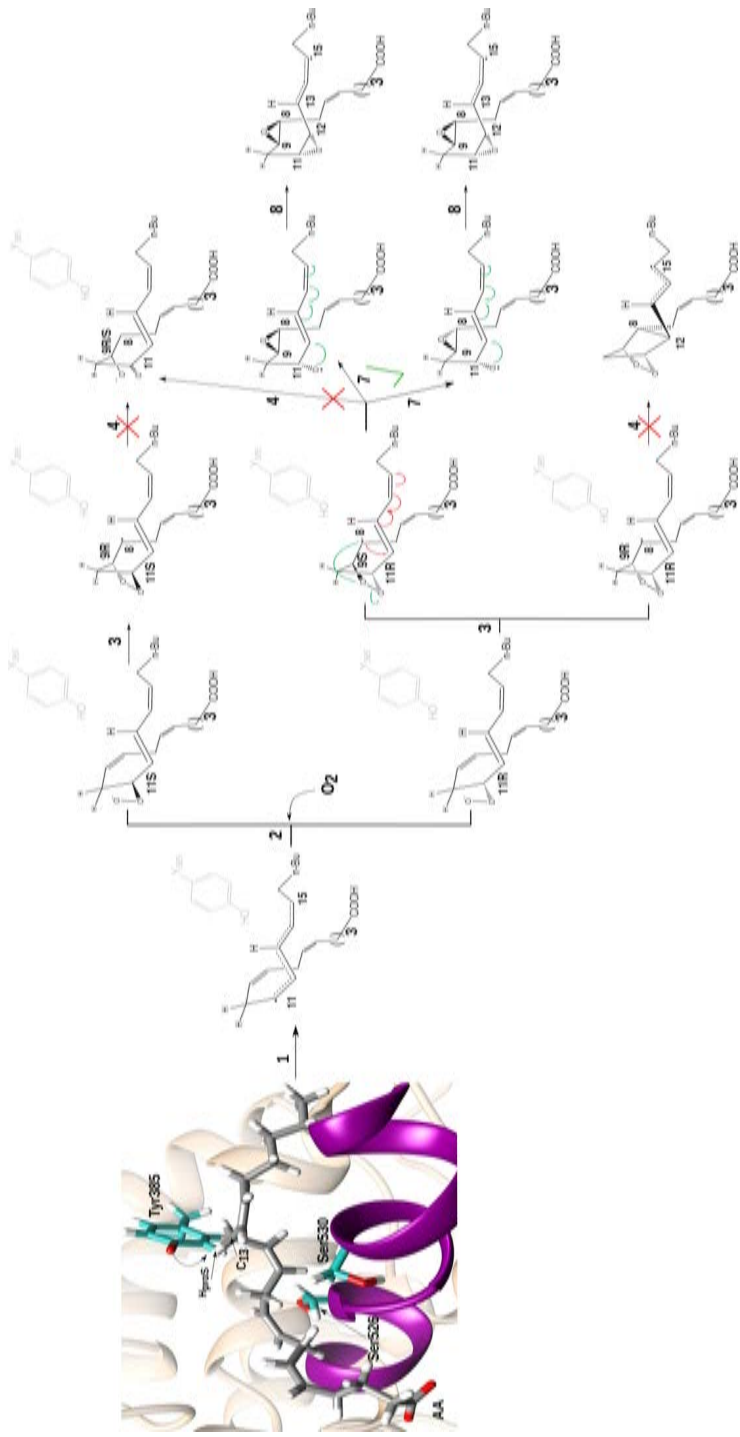


Figure 3.4: Representation of all-radical mechanism inside the G526S COX-2 mutant. The blocked paths are marked by a red cross. The possible paths are indicated by a green check-mark. Steps 1 to 4 are the same as in the all-radical mechanism. Steps 7 and 8 correspond to the formation of 8,9-11,12-diepoxy derivatives of AA.

occurred, leading to the formation of a ketone group in C₁₁ and a radical centered at the C₉. In fact, the homolytic cleavage of the O–O bond actually leads to the formation of 8,9-11,12-diepoxy derivatives of the arachidonic acid, confirming again the experimental results.⁶⁰

Finally, all these results show two important conclusions: i) the Ty385, Leu352, Tyr348 and Phe518 residues are crucial to control the regio/stereoselectivity of the two cyclization steps, and ii) the orientation of rotamers of the α -helix D (from 521 to 535 residues), for instance, Ser530, Gly526, and Met522, are also crucial to control the rigidity of the α -helix D influencing the 8,12-cyclization.

3.4 Molecular Details of the Inhibition by Aspirin

Considering that the reaction mechanism for the formation of PGG₂ in COX-2 is already well-known by the study exposed in section 3.1, the reaction mechanism of the NSAIDs, like Aspirin, becomes the new focus of interest for this thesis. The important facts for this study are focused on, after irreversible acetylation of Ser530, how aspirin inhibits the formation of PGG₂ by catalyzing the synthesis of the major product, 15R-HETE. Until now the total inhibition of prostaglandins was widely accepted. However, as mentioned in section 1.5.1.1, recent experimental results⁷⁹ of Giménez-Bastida et al. have shown that aspirin-acetylated COX-2 (from now on acetylated COX-2) is able to form PGE₂ as a minor product. These results drew our attention especially because it was not known how acetylated COX-2 still retains COX-activity.

Therefore, in this thesis the study of the all-radical mechanism inside the acetylated COX-2 is carried out, to analyze not only the

formation of 15R-HETE, but also to give a clear explanation of the role of the acetyl-Ser530 group in the formation of the small amount of PGE₂, see article III.

First of all, the acetylation of Ser530 is performed. Then, different feasible structures of AA within acetylated COX-2 active site have been simulated by a 100 ns MD simulation. Then, the resulting MD shows two important facts: i) reactive AA structures with H_{13proS} and H_{13proR} near the oxygen acceptor atom of Tyr385 are observed, and ii) non "L-shaped" structures of AA are obtained due to the steric hindrance of different rotamers of the acetyl-Ser530 group. For that reason, four pre-catalytic snapshots corresponding to different rotamers of the acetyl-Ser530 group are selected to study the reaction mechanism by the calculation of the potential energy profile of each step using a QM/MM approach. Furthermore, for each pre-catalytic snapshot the reaction mechanism has been studied for the abstraction of H_{13proS} and H_{13proR}.

To understand these results an accurate analysis of the all possible reactions steps is performed, see Figure 3.5. As expected, the results reveal two important features of the role of acetylated-Ser530 residue within COX-2. On one hand, the formation of the AA 15R peroxy radical is more favorable than the AA 15S peroxy radical. In addition, the formation of the AA 15R peroxy radical is obtained by the abstraction of H_{13proS} and H_{13proR}, and it can either occur by antarafacial or suprafacial O₂ attack, depending on the orientation of the acetyl-Ser530 group in each case. On the other hand, the small amount of PGE₂ is only viable with one orientation of the acetyl-Ser530 group, following the all-radical mechanism initiated by the abstraction of H_{13proS}.

After the corresponding hydrogen abstraction from AA by the Tyr-385-O•, the formation of the delocalized C₁₁-C₁₅ pentadienyl radical allows the O₂ attack not only to C₁₅, but also to C₁₁. Following the

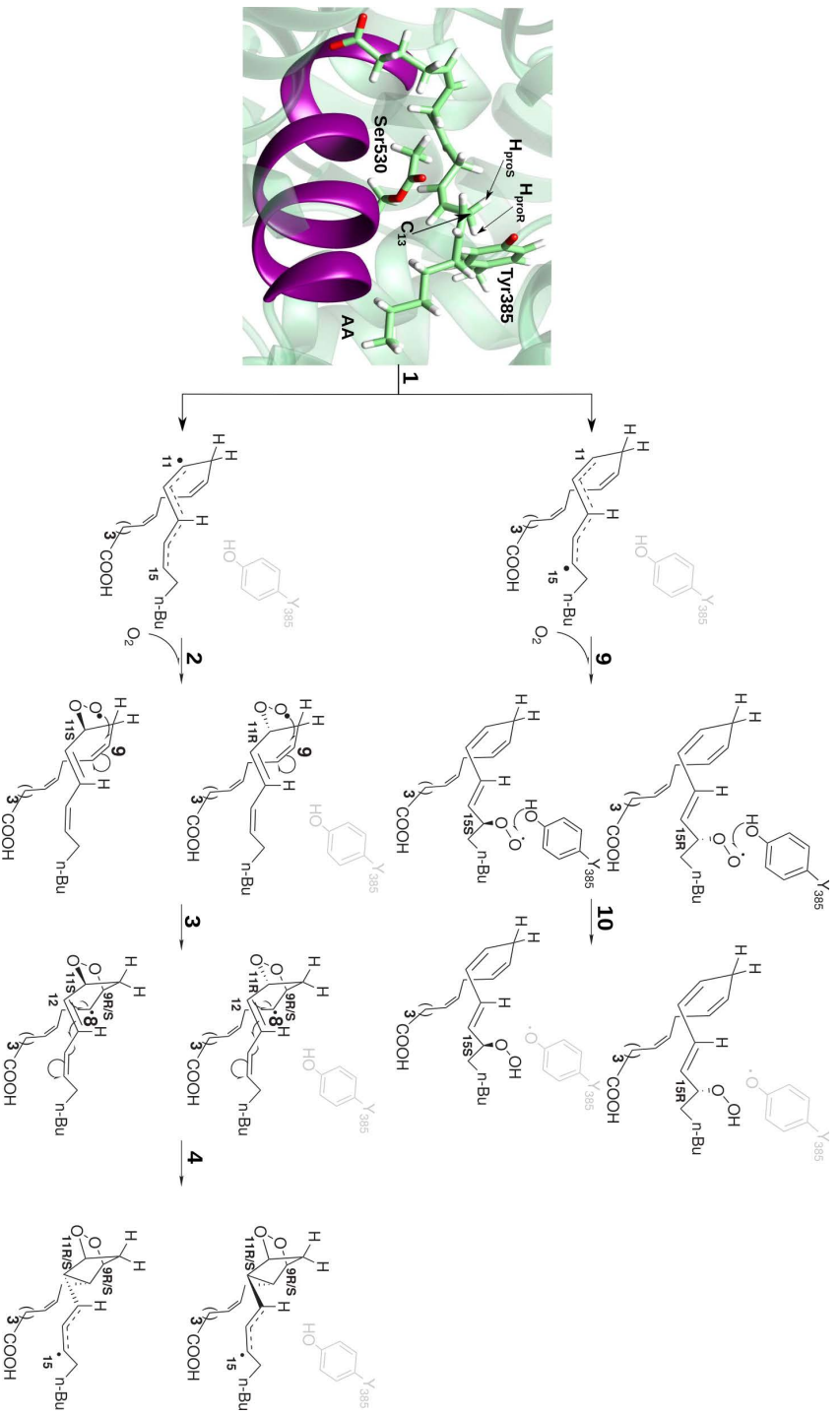


Figure 3.5: Scheme of all reaction steps studied initiated by the abstraction of H_{13proS} and H_{13proR} within acetylated COX-2. Steps 1 to 4 are the same as in the all-radical mechanism. Steps 9 and 10 correspond to the formation of the major product (15-HpETE).

steps of the all-radical mechanism (Fig.3.5), like in the case of C₁₅, we have shown that the way how O₂ attacks at C₁₁ (second step) depends on the particular conformation of the delocalized C₁₁–C₁₅ pentadienyl radical in each snapshot, and then it is influenced by the orientation of the acetyl-Ser530 group. The lower potential energy barriers clearly correspond to antarafacial attacks of O₂, leading to either R or S stereochemistry.

The formation of the C₈-radical cyclic endoperoxides (third step) behaves differently, depending on the acetyl rotamer. All the pathways studied allow the formation of the C₈-radical cyclic endoperoxides, with a considerable dispersion of potential energy barriers. Only in some cases (6 out of 21), the right (9R, 11R) endoperoxide bridge corresponding to a prostaglandin H₂ is formed, as it happens inside COX-2. The intermediates (9S, 11R) and (9R, 11S) endoperoxides turn out to be unable to produce the 8,12-cyclization to yield the bicyclo endoperoxide (fourth step). We have shown that both the intermediates (9R, 11R) and (9S, 11S) endoperoxides do produce the new C₈–C₁₂ bond, giving a ring of five carbon atoms and a C₁₃–C₁₅ allyl radical. Thus, acetylated COX-2 is really able to structurally catalyze the formation of the (9R, 11R) bicyclo endoperoxide driving the transformation of AA along the all-radical mechanism with potential energy barriers quite similar to many other enzymatic reactions.

The products obtained after the 8,12-cyclization for the snapshots with initial abstraction of H_{13_{proS}} are bicyclo endoperoxides containing a trans configuration of their side chains relative to the cyclopentane ring, as corresponds to the natural prostaglandins stereospecifically synthesized by COX-2. Conversely, the snapshots with initial abstraction of H_{13_{proR}} lead to bicyclo endoperoxides with a cis configuration, which would yield the cis isoprostane 15-H_{2_t}-IsoP. In comparison with the COX-2, the bicyclo endoperoxide trans isomer is again stabilized

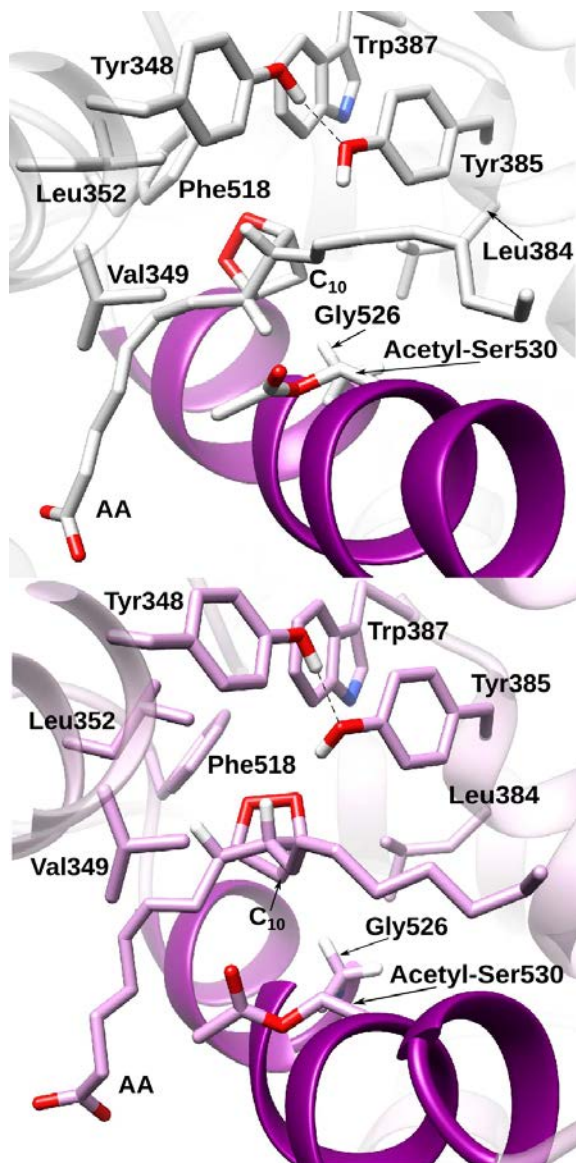


Figure 3.6: The residues of the reaction channel for the 8,12-cyclization in the acetylated COX-2. On top the environment of the bicyclo endoperoxide trans isomer is represented. On bottom the environment of the bicyclo endoperoxide cis isomer is represented. The hydrogens of C₈ and C₁₂ are pictured to highlight the difference of trans and cis isomers.

by the same residues, while the cis isomer is stabilized by completely different residues, see Figure 3.6. This Figure clearly shows that the bicyclo endoperoxide trans isomer is surrounded by Leu352, Trp387 and Phe518, while the bicyclo endoperoxide cis isomer is surrounded by Trp387, Phe518 and Tyr385. The position of the C₁₀ atom of the bicyclo endoperoxide of both is located again near Gly526 and Leu384.

Comparing the potential energy barriers involved in the production of the different possible products, it can be seen that the synthesis of 15R-HpETE (then reduced to the main product 15R-HETE) is kinetically dominant in the oxidation of AA catalyzed by acetylated COX-2. A small amount of (9R, 11R) bicyclo endoperoxide can also be formed, leading to PGH₂, and so explaining the formation of PGE₂ as a minor product detected by Giménez-Bastida et al.⁷⁹. However, the synthesis of isoprostanes is not actually achieved because it is very far from being kinetically competitive with the formation of the 15R-HETE.

Appendices

Appendix A

Radical Mechanism from HproS

In this appendix the results of the all-radical mechanism starting from H_{13proS} abstraction are reported. It is important to highlight that these results were obtained with the same methodology described in article I.

A.1 QM/MM calculations

One pre-catalytic snapshot with H_{13proR} ready to react is selected to study the H_{13proS} abstraction. The results will be compared with the ones obtained for the H_{13proR} abstraction. To initiate the analysis of the all-radical mechanism, the potential energy barriers of each step have been calculated by using the QM/MM method.

In the first step, the potential energy profile has been built as a function of the difference between the distances corresponding to the breaking bond ($C_{13}-H_{13proS}$) and the forming bond ($H_{13proS}-OTyr385$).

The distances relative to the three atoms that directly participate in the breaking/forming bonds for the reactant, transition state structure and product, along with the potential energy barrier are given in Table A.1.

Table A.1: Distances (\AA) relative to the three atoms that directly participate in the breaking/forming bonds for the reactants, transition state structures and products, along with the potential energy barrier (kcal/mol) corresponding to the $\text{H}_{13\text{proS}}$ abstraction from AA by the tyrosyl radical for the pre-catalytic snapshot. C, H and O stands, respectively, for C_{13} , $\text{H}_{13\text{proS}}$ and O of tyrosyl radical. R, TS and P stand, respectively, for reactant, transition state and product.

	R	TS	P
d(C–H)	1.09	1.31	2.53
d(H–O)	2.38	1.29	0.97
d(C–O)	3.37	2.54	3.35
ΔE^\ddagger	17.2		

In the second step, different possible starting positions of the oxygen molecule have been chosen, taking C_{11} as the origin of coordinates. In all, 53 initial positions of the oxygen molecule have been considered. Then, QM/MM single point energy calculations have been carried out for the 53 positions and the higher energy structures have been discarded. The most stable structures have been optimized and taken as starting points to build the potential energy profile, with the distance of the forming bond ($\text{O}_2\text{--C}_{11}$) as the reaction coordinate. All the pathways that have been able to reach the products are given in Table A.2.

Table A.2: Optimized reactant distances $\text{O}_2\text{-C}_{11}$ (\AA) and potential energy barriers (kcal/mol) associated to the attacks of the oxygen molecule at C_{11} that have been able to reach the peroxy radical, along with the stereochemistry at C_{11} of the peroxy radical formed. I, II and III represent the O_2 attacks that have been able to reach the final product. Antara and Supra stands for antarafacial and suprafacial O_2 attack, respectively.

	I	II	III
$d(\text{O}_2\text{-C}_{11})_{opt}$	2.67	4.40	3.79
O_2 attack	Antara	Supra	Antara
Stereochemistry C_{11}	R	S	R
ΔE^\ddagger	0.0	8.8	5.1

In the third step, all the peroxy radicals formed corresponding to the antarafacial addition and the suprafacial addition have been taken to follow the formation of the C_8 -radical cyclic endoperoxide by means of a 9,11-cyclization step. The potential energy barriers for this first cyclization, with the distance O-C_9 optimized are given in Table A.3, being this distance the reaction coordinate of the 9,11-cyclization step.

Table A.3: Optimized reactant distances (\AA) from the free oxygen of the peroxy radicals to C_{11} (I to III) and potential energy barriers (kcal/mol) associated to the 9,11-cyclization to form the C_8 -radical cyclic endoperoxide along with their corresponding stereochemistry for C_{11} and C_9 at the endoperoxide bridge.

	I	II	III
$d(\text{O-C}_9)_{opt}$	4.29	3.17	3.99
O_2 attack	Antara	Supra	Antara
Stereochemistry C_{11}	R	S	R
Stereochemistry C_9	R	R	R
ΔE^\ddagger	18.2	16.2	28.5

In the fourth step, all the C_8 -radical cyclic endoperoxide intermediates formed have been taken to follow the formation of the bicyclo endoperoxide with a C_{13} - C_{15} allyl radical by means of a 8,12-cyclization step. The potential energy barriers for this second cyclization, with the distance C_8 - C_{12} optimized are given in Table A.4, being this distance the reaction coordinate of the 8,12-cyclization step.

Table A.4: Optimized reactant distances (Å) (I to III) and potential energy barriers (kcal/mol) associated to the 8,12-cyclization to form a bicyclo endoperoxide with a C_{13} - C_{15} allyl radical along with their corresponding stereochemistry for the cyclopentane ring.

	I	II	III
$d(C_8-C_{12})_{opt}$	4.66	Not formed	4.54
O₂ attack	Antara	Supra	Antara
Cyclopentane ring	Trans	Broken structure	Trans
ΔE^\ddagger	12.8	-	12.5

It has to be remarked that only the (9R, 11R) endoperoxide bridges are able to undergo the 8-12 cyclization to form the bicyclo endoperoxides, and that just the trans ring isomers are obtained.

Finally, for lack of time, the two subsequent steps have not been calculated. However, the formed bicyclo endoperoxide with a C_{13} - C_{15} allyl radical presents the same arrangement, just as the trans ring isomer obtained from H_{13proR} abstraction, see Figure A.1.

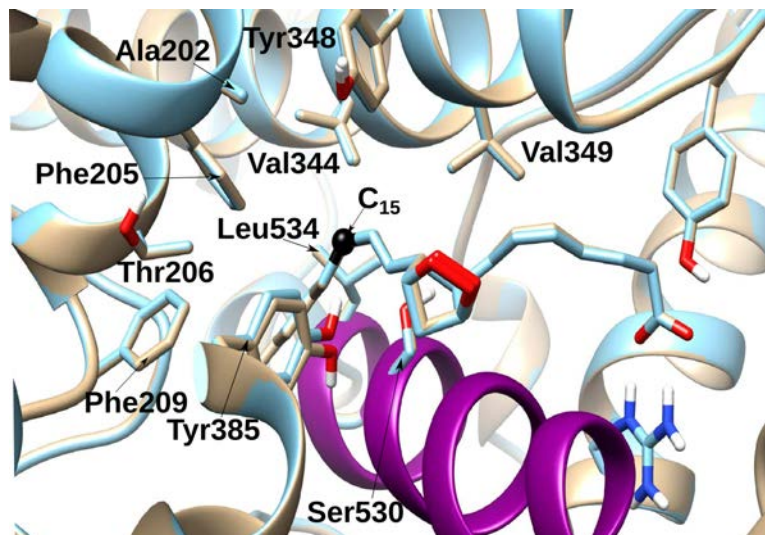


Figure A.1: Conformational arrangement of both bicyclo endoperoxides with a C₁₃–C₁₅ allyl radical formed from the H_{13*proS*} and H_{13*proR*} abstractions. In blue, the bicyclo endoperoxide from the H_{13*proS*} abstraction is represented. In tan, the trans ring isomer of the bicyclo endoperoxide from the H_{13*proR*} abstraction is represented.

Chapter 4

COX-2:EPA

First of all in this chapter the molecular details of the first step of the all-radical mechanism, involved in the conversion of the EPA to PGG_3 catalyzed by COX-2, are reported. Secondly, the first theoretical study of the first part of the biosynthesis of Resolvin E1 (RvE1) and E2 (RvE2) catalyzed by acetylated COX-2 is introduced. This work has been performed with the collaboration of the Computational Biochemistry group at the University of Porto. The article is still being written.

4.1 Introduction

As mentioned in section 1.1.4, the 3-series PGs present less inflammatory effects than the 2-series PGs,^{22, 28} and follow the same catalytic mechanism (Fig.1.6). In this case, the catalytic mechanism starts with the conversion of EPA to PGG_3 catalyzed by COX-2, and produces as well three secondary products: 11-hydroxyeicosapentaenoic (11-HEPE), 15-hydroxyeicosapentaenoic (15-HEPE) and 14-hydroxyeicosapentaenoic (14-HEPE) acids.⁷²

However, the major contribution of EPA to inflammation processes is being precursor of the formation of Specialized Pro-resolving Mediators (SPMs), such as resolvins and protectins.¹⁴ These lipid mediators present the active capacity to clear inflammation and promote tissue homeostasis.^{14, 15} Surprisingly, Serhan et al.²⁹ have demonstrated that the inhibition of COX-2 by aspirin with a later presence of EPA is crucial for the biosynthesis of two types of resolvins, namely E-series resolvins (RvE1 and RvE2).^{152, 153}

Considering the experimental results,^{152, 153} scientists know that the E-series resolvin biosynthesis starts with the conversion of EPA to 18-hydroxyeicosapentaenoic acid (18-HEPE) catalyzed by acetylated COX-2, followed by 5-LOX catalysis to obtain RvE2, or followed by 5-LOX and LTA₄ hydrolase (LTA₄H) catalysis to obtain RvE1 (see Figure 4.1). In absence of aspirin COX-2 seems unable to produce 18-HEPE.^{72, 152}

The experimental results also suggested that aspirin might promote 18R-HEPE production as well as 18S-HEPE from ingested EPA.¹⁵³ The 18R-HEPE and 18S-HEPE intermediates were also identified as the main precursors of the formation of two different resolvins: RvE1/E2 and 18S-Resolvin E1/E2, respectively (Fig.4.1).

However, the way how acetylated COX-2 manages to produce both 18R/S-HEPE is still unknown for scientists. For that reason, in this work MD simulations and QM/MM calculations were combined: i) to reveal the molecular details of the first step of the all-radical mechanism for EPA in COX-2, and ii) to shed light on the molecular details of the mechanism involved in the conversion of EPA to 18-HEPE by acetylated COX-2.

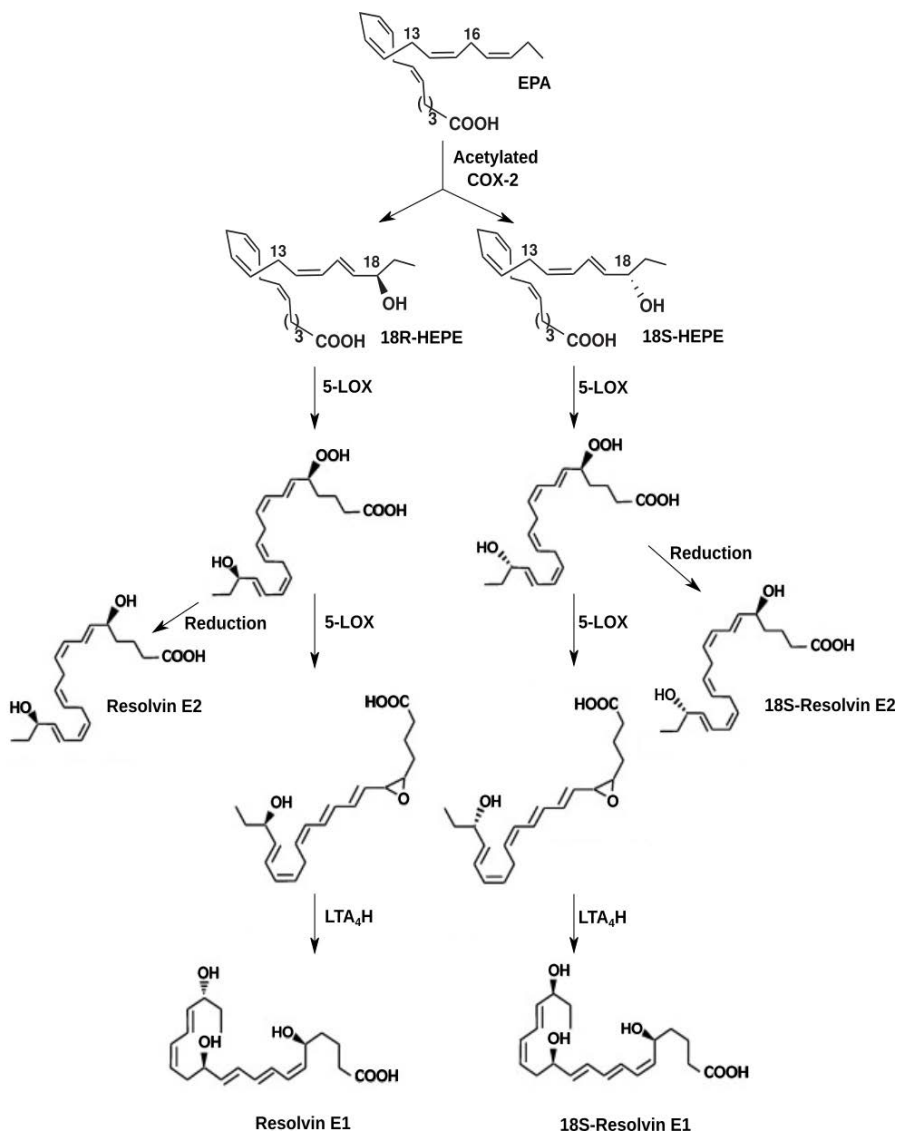


Figure 4.1: Biosynthetic pathways to obtain Resolvin E1/E2, and 18S-Resolvin E1/E2 proposed by Serhan et al.^{152, 153}

4.2 Methodology

To perform the first study, the enzyme was built based on the murine COX-2:EPA complex (PDB code 3HS6)¹, in which the protoporphyrin IX group is complexed to a Co^{3+} and the homodimer presents EPA interacting in different conformations in each monomer. The, Co^{3+} was replaced by Fe^{3+} , and the heme prosthetic group was tethered to the axial histidine ligand (His388) in order to prevent the dissociation from the complex during the simulation. As in crystallographic structure of COX-2:AA, only the monomer B exhibits the productive configuration in the cyclooxygenase channel, so this monomer was also used for this work. The heme group and the tyrosyl radical were parameterized as explained in article I. The AMBER ff14SB force field¹⁵⁴ was employed to define the protein residues, and the missing hydrogen atoms were added using the leap module of AMBER14¹⁵⁵. The total system was solvated in an almost cubic box of TIP3P¹⁵⁶ water molecules. Then, the resulting system was minimized and two MD simulations (see section 4.3.1) were performed under periodic boundary conditions using the same protocol as explained in article I. Finally, representative snapshots of the MD simulations were used to perform the QM/MM calculations of the hydrogen abstraction (first step) of the all-radical mechanism. The QM/MM calculations were performed using ONIOM2(QM:MM), in which the density functional B3LYP and the 6-31G(d,p) basis set were used for the QM method, and the interaction between regions was treated with the electrostatic embedding scheme.

To perform the second study, the acetylated COX-2:EPA Michaelis complex was built based on monomer B of the acetylated COX-2:AA complex used in article III, replacing AA by EPA. The same force-field was employed, and the total system was again solvated in an al-

most cubic box of TIP3P water molecules. Then, the resulting system was minimized and one MD simulation was performed under periodic boundary conditions applying the same protocol as explained in article I. Finally, representative snapshots of the MD simulation were used to perform the QM/MM calculations of each step of the 18-HEPE formation. The QM/MM calculations were performed in the same manner as explained in the previous paragraph.

4.3 Results and Discussion

4.3.1 MD simulations for COX-2:EPA

As explained in section 1.3.1, EPA follows the same catalytic mechanism as AA has within COX-2. For that reason, just as for COX-2:AA, two 100 ns MD simulations of COX-2:EPA have been carried out, one containing Tyr385 and the other with Tyr385-O[•].

First of all, the protein stability in both MD simulations has been checked by the root mean-square deviation (RMSD), see Figure 4.2. As seen in this Figure the protein in both MD simulations is quite equilibrated, when the N-terminal is not considered. Secondly, only the feasibility of the hydrogen abstraction (first step) of the all-radical mechanism has been studied in the first part of this work.

Considering that COX-2:EPA produces PGG₃ as a major product, and 11-HEPE, 15-HEPE and 14-HEPE as secondary products, the hydrogen abstraction could be at C₁₃ as well as C₁₆. Thus, the evolution of the H_{Z_{proX}}-OTyr385 and H_{Z_{proX}}-OTyr385 distances along both MD simulations has been followed, being *Z* the number of the carbon atom, 13 or 16, and *X* refers to the hydrogen proS or proR, see Figure 4.3.

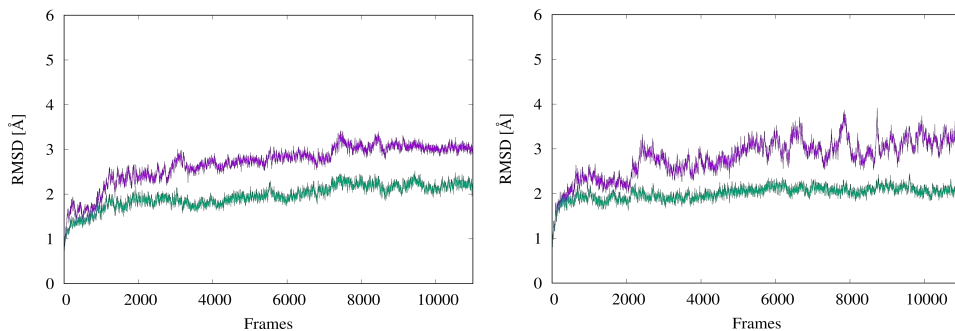


Figure 4.2: RMSD of the protein α -carbons (purple line) and the RMSD excluding the residues of the N-terminal domain (green line). The RMSD is referenced to the first structure of the 100 ns MD simulation of EPA including Tyr385 of monomer B of COX-2. On the right the RMSD with Tyr385-O \bullet is shown, and on the left the RMSD with Tyr385 is represented. A frame has been taken each 10 ps.

As shown in Figure 4.3 in both MD simulations there are more snapshots with H_{16proR} closer to the oxygen acceptor than H_{16proS}. Moreover, in the MD simulation with Tyr385-O \bullet there are more snapshots with H_{16proR} closer to the oxygen acceptor than in the MD simulation with Tyr385. As for C₁₃ in both MD simulations the H_{13proR} is generally closer to the oxygen acceptor than the H_{13proS}. Nevertheless, it is not clear if the enzyme prefers to abstract a hydrogen from C₁₃ or C₁₆. For that reason, one structure each 10 ps along both 100 ns MD simulations has been taken. Then, according to the conditions $d(\text{H}_{ZproX}\text{-OTyr385}) \leq 3 \text{ \AA}$ and $d(\text{H}_{ZproX}\text{-OTyr385}) < d(\text{C}_Z\text{-OTyr385})$, the MD snapshots have been filtered, in order to select the more adequate structures to initiate the all-radical mechanism, see Table 4.1.

Finally, this last selection clearly shows that when the enzyme includes the Tyr385-O \bullet , not only the number of reactive structures increases but also H_{13proR} is the most potentially reactive hydrogen.

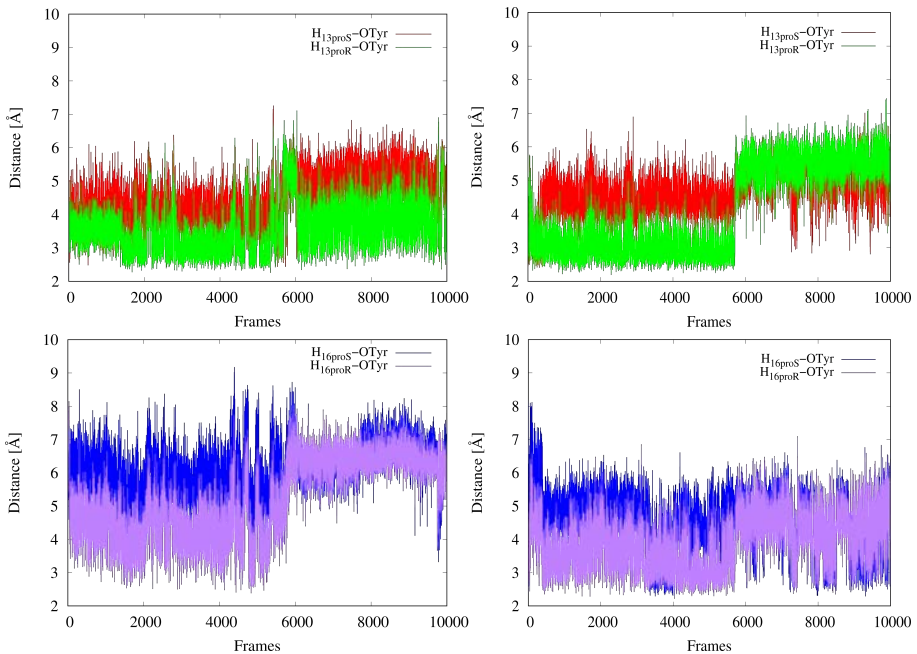


Figure 4.3: Evolution of the H_{13proX} -OTyr385 and H_{16proX} -OTyr385 distances along both 100 ns MD simulations. On the right side, these distances for the MD simulation with Tyr385-O \bullet are represented. On the left side, the same distances for the MD simulation with Tyr385 are shown.

Table 4.1: The total number of the feasible reactive structures to initiate the all-radical mechanism by the abstraction of a hydrogen at C₁₃ of EPA, and at C₁₆ of EPA. The selection is performed along the 100 ns MD simulations taking one structure each 10 ps and filtering them according to the conditions explained in the text.

Reactive Structures				
100 ns MD	H_{13proR}	H_{13proS}	H_{16proR}	H_{16proS}
Tyr385-OH	2580	192	163	0
Tyr385-O \bullet	3252	123	1677	694

Table 4.2: Initial distances (\AA) of the atoms involved in the hydrogen abstraction (first step) of the all-radical mechanism.

H_{13proR}			H_{16proR}		
Snapshots	d(H-O)	d(C-O)	Snapshots	d(H-O)	d(C-O)
I	2.51	3.53	V	2.34	3.34
II	2.45	3.50	II	2.85	3.66
III	2.95	3.87	VI	2.36	2.88
IV	2.65	3.56	VII	2.45	3.88

At this point, to facilitate the analysis of the binding modes, only the reactive structures of the simulation with Tyr385-O \bullet have been considered. On one hand, from 3252 reactive structures with the H_{13proR} near the oxygen acceptor, four structures (snapshots I to IV) have been selected randomly. On the other hand, from 1677 structures with the H_{16proR} near the oxygen acceptor, three structures (snapshots V to VII) have been selected randomly.

4.3.2 QM/MM calculations of COX-2:EPA

To initiate the analysis, all these snapshots have been selected as starting points to perform the QM/MM calculations of the hydrogen abstraction step. The initial distances of the atoms involved in the hydrogen abstraction step are presented in the Table 4.2, confirming that all the snapshots present $d(H_{ZproR}\text{-OTyr385}) < d(C_Z\text{-OTyr385})$. It is important to highlight that snapshot II is the same for both abstractions, because the H_{13proR} and H_{16proR} are both near the oxygen acceptor.

For each snapshot the distance $d(H_{ZproR}\text{-OTyr385})$ have been taken to define the reaction coordinate of the H-abstraction step. Then, in Table 4.3 only the potential energy barriers of the potential energy profiles reaching the products are reported.

Table 4.3: Potential energy barriers (kcal/mol) corresponding to the hydrogen abstractions for snapshots with H_{ZproR} that have been able to reach the products.

H_{13proR}	
Snapshots	ΔE^\ddagger
I	25.0
II	26.9
IV	22.3
H_{16proR}	
Snapshots	ΔE^\ddagger
V	29.1
II	31.9

As seen in Table 4.3, the potential energy barrier of the snapshot II with H_{13proR} is lower than the barrier of the snapshot II with H_{16proR} , being the former more reactive. With respect to the rest of snapshots the same tendency is also observed. Then, these results could explain the formation of 11-HEPE and 15-HEPE instead of 18-HEPE products as obtained experimentally.^{72, 152}

4.3.3 MD simulations for acetylated COX-2:EPA

In the second part of this work, a 100 ns MD simulation of monomer B of acetylated COX-2 with the Tyr385-O• and EPA has been carried out. Then, the protein stability along the simulation has been checked by the root mean-square deviation (RMSD), see Figure 4.4. As seen in Figure 4.4 the protein is quite equilibrated when the N-terminal is not considered.

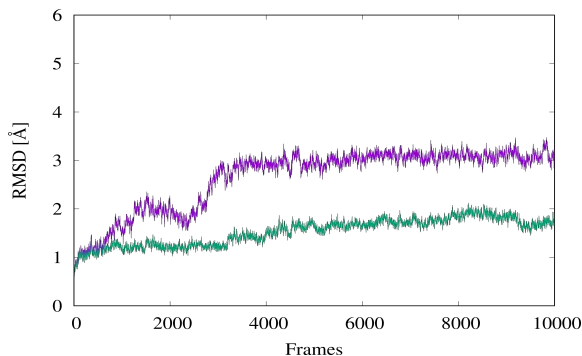


Figure 4.4: RMSD of the protein α -carbons (purple line) and the RMSD excluding the residues of the N-terminal domain (green line). The RMSD is referenced to the first structure of the 100 ns MD simulation of EPA including Tyr385-O \bullet of monomer B of acetylated COX-2. A frame has been taken each 10 ps.

As explained in section 4.1, 18-HEPE within acetylated COX-2 has been considered the principal product. This product could only be obtained by the abstraction of a hydrogen at C₁₆ of EPA.

However, considering the results of COX-2:EPA, the abstraction of a hydrogen at C₁₃ of EPA has also been studied. For that reason, in the second part of this work, not only the feasibility of the hydrogen abstraction (first step) of the all-radical mechanism, but also the possible formation of 18R/S-HEPE have been studied.

The evolution of the $H_{Z_{proX}}-OTyr385$ and $H_{Z_{proS}}-OTyr385$ distances along the MD simulation has been followed, see Figure 4.5. As shown in this Figure along the 100 ns the $H_{Z_{proS}}$ at both carbon atoms seems somewhat closer to the oxygen acceptor of Tyr385 than the $H_{Z_{proR}}$. However, it is not clear how many structures are feasible to react. For that reason, one structure each 10 ps along the 100 ns MD trajectory has been taken.

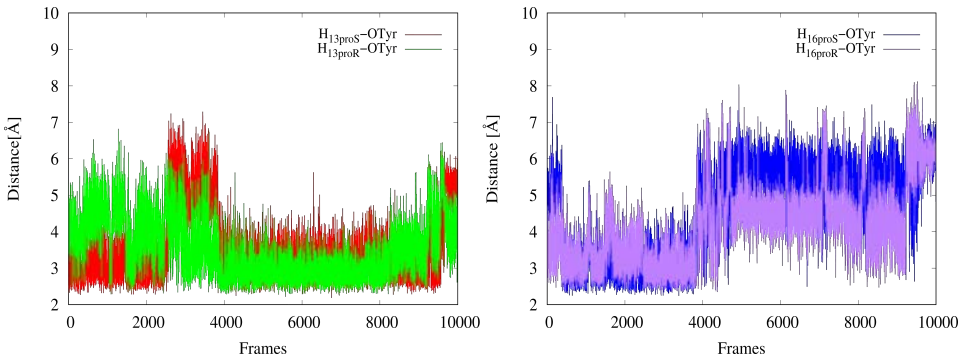


Figure 4.5: Evolution of the H_{13proX} -OTyr385 and H_{16proX} -OTyr385 distances along the 100 ns MD simulation. On the right side, the distances H_{16proX} -OTyr385 along simulation are represented. On the left side, the distances H_{13proX} -OTyr385 along simulation are shown.

Table 4.4: The total number of the feasible reactive structures to initiate the abstraction of a hydrogen at C_{13} of EPA and at C_{16} of EPA. The selection is performed along the 100 ns MD simulation taking one structure each 10 ps and filtering them according to the conditions explained in the text.

Reactive Structures				
100 ns MD	H_{13proR}	H_{13proS}	H_{16proR}	H_{16proS}
Tyr385-O\bullet	3497	3830	1552	1954

Then, according to the reactive conditions of the hydrogen abstraction $d(H_{ZproX}\text{-OTyr385}) \leq 3 \text{ \AA}$ and $d(H_{ZproX}\text{-OTyr385}) < d(C_{Z}\text{-OTyr385})$, the MD snapshots have been filtered, see Table 4.4.

As expected, Table 4.4 shows that there are more reactive structures with H_{ZproS} at both carbon atoms closer to the oxygen acceptor of Tyr385 than with H_{ZproR} . Consequently, in order to facilitate the analysis of the binding modes, only the reactive structures with H_{13proS} and H_{16proS} will be used to perform the clustering. To start this clustering analysis, 5 clusters of acetylated-Ser530 have been obtained. Next, some snapshots were selected mapping the reactive structures

of H_{ZproS} with the acetylated-Ser530 clusters, extracting the centroid snapshot of the first and second cluster, respectively.

Then, on one hand, from the 3830 reactive structures of H_{13proS} , the centroid structures are called snapshot I and II. On the other hand, from the 1954 reactive structures of H_{16proS} , the centroid structures are called snapshot V and VI. Furthermore, two snapshots with both hydrogens at C_{13} near the oxygen acceptor have been mapped with the first cluster of the acetylated-Ser530 (called snapshot III and IV). Finally, two more snapshots with H_{16proS} near Tyr385-O \bullet have been selected randomly from the resulting mapping of the reactive structures of H_{16proS} with the first cluster of the acetylated-Ser530 (called snapshot VII and VIII).

4.3.4 QM/MM calculations for acetylated COX-2:EPA

To initiate the analysis, these snapshots have been selected as starting point to perform the QM/MM calculations of the hydrogen abstraction step. It is important to highlight that snapshot V also presents H_{13proS} near Tyr385-O \bullet , so such hydrogen is also chosen to study the first step of the mechanism. On the other hand, although snapshot II presents H_{16proS} far from Tyr385-O \bullet (Table 4.5), after an optimization the $d(H_{16proS}-OTyr385)$ distance becomes to 2.44 Å, so such hydrogen is also chosen to be abstracted. The initial distances of the atoms involved in the hydrogen abstraction step are presented in Table 4.5, confirming that all snapshots present $d(H_{ZproS}-OTyr385) < d(C_Z-OTyr385)$.

Continuing with the analysis, each snapshot is taken to build the hydrogen abstraction potential energy profile, considering the distance $d(H_{ZproS}-OTyr385)$ as the reaction coordinate.

Table 4.5: The initial distances of the atoms involved in the hydrogen abstraction (first step) of the all-radical mechanism.

H_{13proS}			H_{16proS}		
Snapshots	d(H-O)	d(C-O)	Snapshots	d(H-O)	d(C-O)
I	2.82	3.81	V	2.86	3.49
II	2.92	3.85	II	3.31	2.86
III	2.73	3.33	VI	2.79	3.79
IV	2.60	3.25	VII	2.49	3.33
V	2.65	3.73	VIII	2.25	2.87

In Table 4.6 only the successful profiles are reported. As seen in Table 4.6, the potential energy barriers of snapshots II and V for H_{13proS} and H_{16proS} abstractions show the expected tendency.

Table 4.6: Potential energy barriers (kcal/mol) corresponding to the H_{13proS} or H_{16proS} abstractions that have been able to reach the products.

H_{13proS}	
Snapshots	ΔE^\ddagger
I	27.7
II	27.5
III	27.4
IV	27.0
V	24.3
H_{16proS}	
Snapshots	ΔE^\ddagger
V	20.4
II	26.6
VI	26.9
VII	24.6
VIII	25.7

The barrier of the abstraction of H_{16proS} is lower than the one of H_{13proR} , being in this case the former more reactive. With respect to the rest snapshots the same tendency is also observed. Then, these results could explain that 18-HEPE appears as a consequence of acetylation of COX-2 by aspirin.

How the acetylated COX-2 manages to form 18R-HEPE and 18S-HEPE obtained experimentally¹⁵³ remains still unclear. To understand these experimental results, the oxygen addition (second step) has been studied, taking the optimized products of the snapshots VII and VIII as starting points. The optimized products of the first step are EPA radicals delocalized over the C_{14} – C_{18} pentadienyl system, in which the radical can be localized at C_{14} or C_{18} when the oxygen molecule is added. For that reason, the oxygen addition is studied at C_{14} only for the snapshot VII, and at C_{18} with the snapshots VII and VIII, see the scheme in Figure 4.6 to follow the resulting products.

To study the second step, different possible starting positions of the oxygen molecule have been chosen to add an oxygen molecule at C_{14} or C_{18} . The placing of these starting oxygen molecules follows the same methodology explained in the three articles, resulting in 53 initial positions of the oxygen molecule for each snapshot. Then, QM/MM single points energy calculations have been carried out for the 53 positions and the higher energy structures have been discarded. Next, the most stable structures have been optimized and taken as starting points to build the reaction path for the oxygen addition to C_{14} or C_{18} , being the corresponding O–C distance the reaction coordinate.

The potential energy barriers obtained for all the pathways that have been able to reach the products for the corresponding snapshots in both additions are given in Tables 4.7 and 4.8. It is important to emphasize that the oxygen attack to both carbon atoms could be antarafacial (that is, the O_2 approaches to the pentadienyl group by the

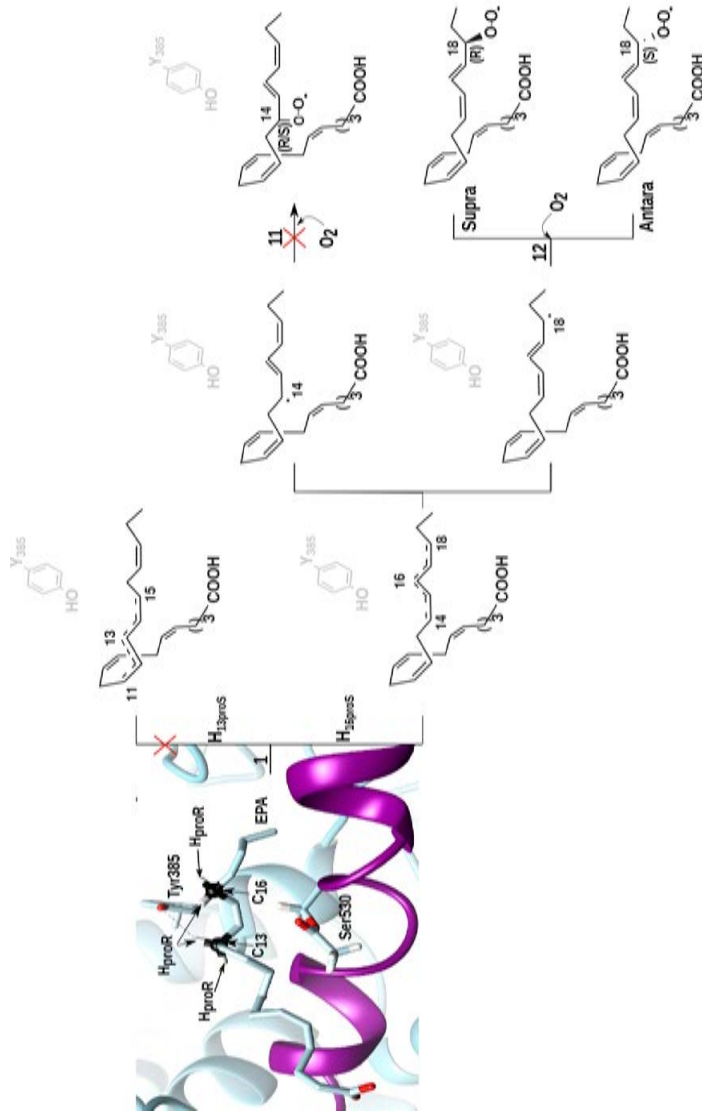


Figure 4.6: Scheme of all the reaction pathways studied to obtain 18R-HEPE and 18S-HEPE within acetylated COX-2 from EPA. Step 1 is the same as in the all-radical mechanism. Steps 11 and 12 correspond to the formation of 14-peroxy-eicosapentaenoic acid (14-pEPE) and 18-peroxy-eicosapentaenoic acid (18-pEPE), respectively. The paths with high barriers are marked by a red cross.

face opposite to Tyr385) or suprafacial (by the same side of Tyr385).

Table 4.7: Potential energy barriers (kcal/mol) corresponding to the O₂ addition to C₁₄ for all the pathways that have been able to reach the products for snapshot VII. Antara and Supra stands for antarafacial and suprafacial O₂ attack, respectively.

Snapshot	O ₂ attack	Stereochemisry C ₁₄	ΔE^\ddagger
VII	Antara	R	15.9
	Antara	R	11.4
	Antara	R	11.0
	Antara	R	13.1
	Supra	S	15.4
	Antara	R	11.3

Table 4.8: Potential energy barriers (kcal/mol) corresponding to the O₂ addition to C₁₈ for all the pathways that have been able to reach the products for snapshot VII and VIII. Antara and Supra stands for antarafacial and suprafacial O₂ attack, respectively.

Snapshots	O ₂ attack	Stereochemisry C ₁₈	ΔE^\ddagger
VII	Supra	R	1.0
	Antara	S	6.7
	Non Antara/Supra	R	4.1
	Non Antara/Supra	R	4.2
	Non Antara/Supra	R	4.0
VIII	Antara	S	7.0
	Supra	R	2.6
	Supra	R	2.1
	Antara	S	0.7

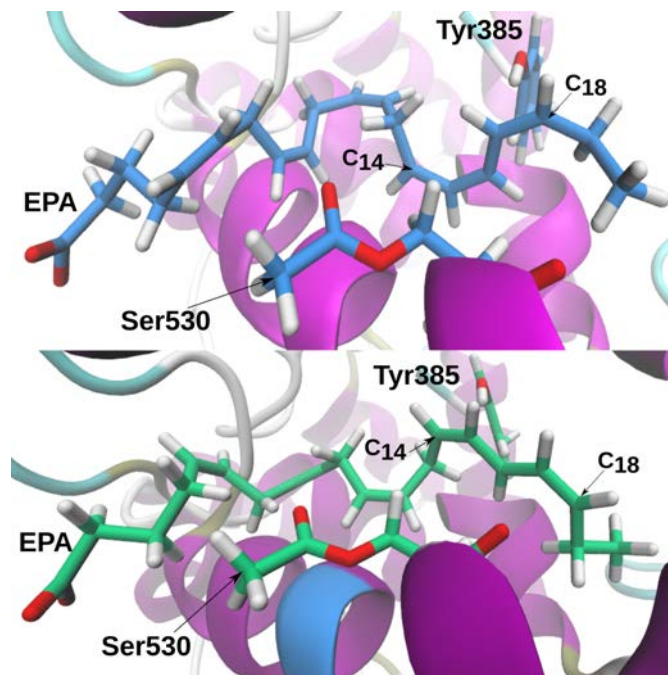


Figure 4.7: EPA delocalized C_{14} – C_{18} pentadienyl radical conformations formed inside the hydrophobic groove of the acetylated COX-2 after hydrogen abstraction of H_{16proS} . Snapshot VII is represented in blue, and Snapshot VIII in green.

On one hand, the results show that the O_2 addition to C_{14} does not appear to be possible, neither by antarafacial nor suprafacial attack, due to the corresponding too high potential energy barriers (Table 4.7). On the other hand, the O_2 addition to C_{18} for both snapshots, VII and VIII, following the antarafacial and the suprafacial attack appear to be possible, forming the 18S-peroxy-eicosapentaenoic (18S-pEPE) and 18R-peroxy-eicosapentaenoic (18R-pEPE) acid radical intermediates, respectively.

In agreement with the experimental results,^{152, 153} Table 4.8 shows that the potential energy barriers of both products are favorable, being different in each snapshot due to the conformations of the delocalized

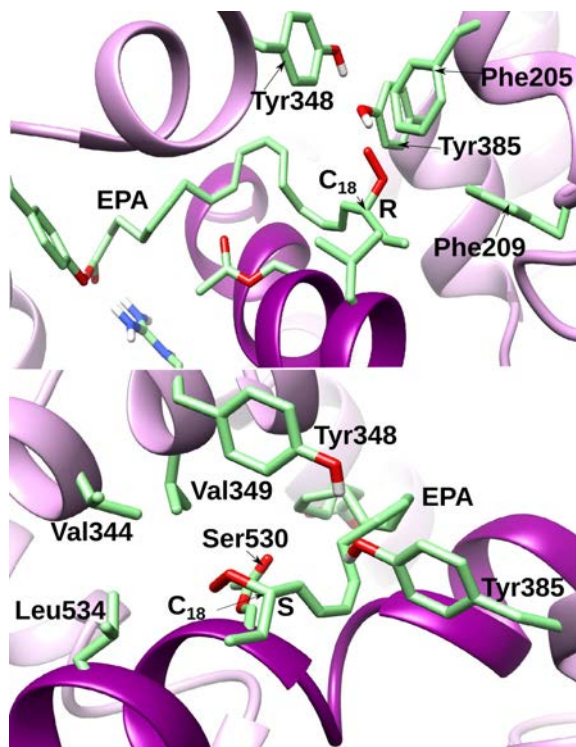


Figure 4.8: Formation of the 18R-pEPE and 18S-pEPE radical intermediates of snapshot VIII. On top, the formation of the 18R-pEPE from a suprafacial oxygen addition. On bottom, the formation of the 18S-pEPE from an antarafacial oxygen addition.

C_{14} – C_{18} pentadienyl radical adopted after the H-abstraction, see Figure 4.7, just as inside the acetylated COX-2:AA.

Finally a molecular analysis has been carried out, see Figure 4.8. Snapshot VIII is selected to check which residues stabilized the 18R-pEPE and 18S-pEPE radical intermediates. Figure 4.8 reveals that 18R-pEPE in the suprafacial side is surrounded by Tyr385, Tyr348, Phe209 and Phe205, while the 18S-pEPE in the antarafacial side is surrounded by Ser530, Leu534, Val344, Val349.

Part IV

General Conclusions

Chapter 5

General Conclusions

COX-2 is one of the two main human enzymes responsible for inflammation processes. COX-2 transforms AA to lipid pro-inflammatory mediators, such as prostaglandins. In this sense, COX-2 is considered an important pharmacological target of the nonsteroidal anti-inflammatory drugs (NSAIDs), such as aspirin. Furthermore, COX-2 participates in the biosynthesis of lipid pro-resolving mediators, such as resolvins. Nevertheless, most of the molecular details of the catalytic mechanism and inhibition by aspirin remain unknown. In this thesis, the acquired results contribute to understand these molecular insights. The conclusions of these results are exposed as follow.

First of all, the biosynthesis of prostaglandin results confirm that the six-step all-radical mechanism is the mechanism that governs the conversion of AA to PGG₂ by COX-2, dismissing the 10-step carbocation-based mechanism proposed by Dean and Dean. These results also reveal that there only exists one molecular mechanism that COX-2 employs to catalytically control the regioselectivity and stereoselectivity of PGG₂ formation.

This molecular mechanism consists of the abstraction of H_{proS} or H_{proR} (being the former the most favorable), the antarafacial entrance of the oxygen at C_{11} , the subsequent formation of the (9R, 11R) endoperoxide bridge, the formation of trans cyclopentane ring isomer, and the formation of the 15S hydroperoxide group.

Secondly, the mutagenesis analysis results confirm that PGG_2 synthesis inside Gly526Ser COX-2 follows only the three first steps of the all-radical mechanism, revealing that the orientation of the rotamers of the Ser530, Gly526, and Met522 residues are crucial to make the 8,12-cyclization step possible. However, the mutant allows the homolytic cleavage of the O–O bond of the 9,11-endoperoxide intermediate, being more favorable the formation of the 8,9-11,12-diepoxy derivatives of the arachidonic acid, according to experimental results. Apart from that, these results also show that the Ty385, Leu352, Tyr348 and Phe518 residues are also crucial to control the regio/stereoselectivity of the two cyclization steps.

Third, the results of the inhibition of the PGG_2 product by aspirin reveals the molecular features of the role of acetylated-Ser530 residue inside COX-2. On one hand, the synthesis of 15R-HpETE (then reduced to the main product 15R-HETE) is kinetically dominant in the oxidation of AA catalyzed by aspirin-acetylated COX-2. Besides, the 15R-HpETE product is obtained by the abstraction of H_{13proS} or H_{13proR} , and it can either occur by antarafacial or suprafacial O_2 attack, depending on the orientation of the acetyl-Ser530 group in each case. On the other hand, a small amount of (9R, 11R) bicyclo endoperoxide intermediate can also be formed, leading finally to PGH_2 , and so explaining the experimental results.

Besides, that intermediate is viable only with one orientation of the acetyl-Ser530 group, following the all-radical mechanism initiated by the abstraction of H_{13proS} . Lastly, the synthesis of isoprostanes (that would come from the abstraction of H_{13proR}) is not achieved because it is very far from being kinetically competitive with the formation of the 15R-HETE.

Finally, our calculations show that COX-2 is unable to catalyze the formation of 18-HEPE from EPA. Conversely, in presence of aspirin, acetylated COX-2 produces both 18R-HEPE and 18S-HEPE products, that are precursors of anti-inflammatory E-series resolvins (RvE1 and RvE2) mediators.

Bibliography

- [1] A. J. Vecchio, D. M. Simmons, and M. G. Malkowski. Structural basis of fatty acid substrate binding to cyclooxygenase-2. *Journal of Biological Chemistry*, 285:22152–22163, 2010.
- [2] W. L. Smith, D. L. DeWitt, and R. M. Garavito. Cyclooxygenases: Structural, cellular, and molecular biology. *Annual Review of Biochemistry*, 69:145–182, 2000.
- [3] J. A. Mitchell, P. Akarasereenont, C. Thiemermann, R. J. Flower, and J. R. Vane. Selectivity of nonsteroidal antiinflammatory drugs as inhibitors of constitutive and inducible cyclooxygenase. *Proceedings of the National Academy of Sciences of the United States of America*, 90:11693–7, 1993.
- [4] J. Lei, Y. Zhou, D. Xie, and Y. Zhang. Mechanistic insights into a classic wonder drug-aspirin. *Journal of the American Chemical Society*, 137:70–73, 2015.
- [5] Benjamin J. O., Michael J. L., and Michael G. M. The structure of ibuprofen bound to cyclooxygenase-2. *Journal of Structural Biology*, 189(1):62 – 66, 2015.

- [6] M. J. Lucido, B. J. Orlando, A. J. Vecchio, and M. G. Malkowski. Crystal Structure of Aspirin-Acetylated Human Cyclooxygenase-2: Insight into the Formation of Products with Reversed Stereochemistry. *Biochemistry*, 55:1226–1238, 2016.
- [7] M. E. Konkle, A. L. Blobaum, C. W. Moth, J. J. Prusakiewicz, S. Xu, K. Ghebreselasie, D. Akingbade, A. T. Jacobs, C. A. Rouzer, T. P. Lybrand, and L. J. Marnett. Conservative Secondary Shell Substitution In Cyclooxygenase-2 Reduces Inhibition by Indomethacin Amides and Esters via Altered Enzyme Dynamics. *Biochemistry*, 55:348–359, 2016.
- [8] P. Tosco. A Mechanistic Hypothesis for the Aspirin-Induced Switch in Lipid Mediator Production by Cyclooxygenase-2. *Journal of the American Chemical Society*, 135:10404–10410, 2013.
- [9] G. O. Burr and M. M. Burr. On the nature and role of the fatty acids essential in nutrition. *Journal of Biological Chemistry*, 86:587–621, 1930.
- [10] R. T. Holman. The Slow Discovery of the Importance of ω 3 Essential Fatty Acids in Human Health. *The Journal of Nutrition*, 128:427S–433S, 1998.
- [11] J. M. Lee, H. Lee, S. B. Kang, and W. J. Park. Fatty acid desaturases, polyunsaturated fatty acid regulation, and biotechnological advances. *Nutrients*, 8:23, 2016.
- [12] J. R. Hibbeln, L. R. G. Nieminen, T. L. Blasbalg, J. A. Riggs, and W. E. M. Lands. Healthy intakes of n-3 and n-6 fatty acids: Estimations considering worldwide diversity. *American Journal of Clinical Nutrition*, 83:1483S–1493S, 2006.

- [13] L. G. Cleland, M. J. James, and S. M. Proudman. Fish oil: what the prescriber needs to know. *Arthritis Research & Therapy*, 8, 2006.
- [14] C. N. Serhan and N. A. Petasis. Resolvins and protectins in inflammation resolution. *Chemical Reviews*, 111:5922–5943, 2011.
- [15] C. N. Serhan, N. Chiang, and J. Dalli. New pro-resolving n-3 mediators bridge resolution of infectious inflammation to tissue regeneration. *Molecular Aspects of Medicine*, 64:1–17, 2018.
- [16] B. Samuelsson, S. E. Dahlen, J. A. Lindgren, C. A. Rouzer, and C. N. Serhan. Leukotrienes and lipoxins: Structures, biosynthesis, and biological effects. *Science*, 237:1171–1176, 1987.
- [17] E. M. Smyth, T. Grosser, M. Wang, Y. Yu, and G. A. FitzGerald. Prostanoids in health and disease. *Journal of Lipid Research*, 50: S423–S428, 2009.
- [18] E. Ricciotti and G. A. Fitzgerald. Prostaglandins and inflammation. *Arteriosclerosis, Thrombosis, and Vascular Biology*, 31: 986–1000, 2011.
- [19] S. Moncada and J. R. Vane. The role of prostacyclin in vascular tissue. *Federation Proceedings*, 38:66–71, 1979.
- [20] H. Katagiri, Y. Ito, K. I. Ishii, I. Hayashi, M. Suematsu, S. Yamashina, T. Murata, S. Narumiya, A. Kakita, and M. Majima. Role of Thromboxane Derived from COX-1 and -2 in Hepatic Microcirculatory Dysfunction during endotoxemia in Mice. *Hepatology*, 39:139–150, 2004.

- [21] M. Hamberg and B. Samuelsson. On the mechanism of the biosynthesis of prostaglandins E-1 and F-1-alpha. *Journal of Biological Chemistry*, 242:5336–5343, 1967.
- [22] W. L. Smith, Y. Urade, and P. Jakobsson. Enzymes of the Cyclooxygenase Pathways of Prostanoid Biosynthesis. *Chemical Reviews*, 111:5821–5865, 2011.
- [23] H. R. Herschman. Recent progress in the cellular and molecular biology of prostaglandin synthesis. *Trends in Cardiovascular Medicine*, 8:145–150, 1998.
- [24] R. Poorani, A. N. Bhatt, B. S. Dwarakanath, and U. N. Das. COX-2, aspirin and metabolism of arachidonic, eicosapentaenoic and docosahexaenoic acids and their physiological and clinical significance. *European Journal of Pharmacology*, 785:116–132, 2016.
- [25] P. Yang, Y. Jiang, and S. M. Fischer. Prostaglandin E3 metabolism and cancer. *Cancer Letters*, 348:1–11, 2014.
- [26] G. Calviello, S. Serini, and E. Piccioni. n-3 Polyunsaturated Fatty Acids and the Prevention of Colorectal Cancer: Molecular Mechanisms Involved. *Current Medicinal Chemistry*, 14:3059–3069, 2007.
- [27] L. Hooper, R. L. Thompson, R. A. Harrison, C. D. Summerbell, A. R. Ness, H. J. Moore, H. V. Worthington, P. N. Durrington, J. P. T. Higgins, N. E. Capps, R. A. Riemersma, S. B. J. Ebrahim, and G. D. Smith. Risks and benefits of omega 3 fats for mortality, cardiovascular disease, and cancer: Systematic review. *British Medical Journal*, 332:752–755, 2006.

- [28] M. Wada, C. J. DeLong, Y. H. Hong, C. J. Rieke, I. Song, Ranjinder S. S., C. Yuan, M. Warnock, A. H. Schmaier, C. Yokoyama, and et al. Enzymes and receptors of prostaglandin pathways with arachidonic acid-derived versus eicosapentaenoic acid-derived substrates and products. *The Journal of biological chemistry*, 282:22254–66, 2007.
- [29] C. N. Serhan, C. B. Clish, J. Brannon, S. P. Colgan, N. Chiang, and K. Gronert. Novel functional sets of lipid-derived mediators with antiinflammatory actions generated from omega-3 fatty acids via cyclooxygenase 2-nonsteroidal antiinflammatory drugs and transcellular processing. *The Journal of Experimental Medicine*, 192:1197–1204, 2000.
- [30] T. Miyamoto, N. Ogino, S. Yamamoto, and O. Hayaishi. Purification of prostaglandin endoperoxide synthetase from bovine vesicular gland microsomes. *Journal of Biological Chemistry*, 251:2629–2636, 1976.
- [31] D. L. DeWitt and W. L. Smith. Primary structure of prostaglandin G/H synthase from sheep vesicular gland determined from the complementary DNA sequence. *Proceedings of the National Academy of Sciences of the United States of America*, 85:1412–1416, 1988.
- [32] L. J. Marnett and K. R. Maddipati. Prostaglandin H synthase. In M. Grisham, J. Everse, and K. Everse, editors, *Peroxidases in Chemistry and Biology*, pages 293–334. CRC Press, 1991.
- [33] W. L. Smith and L. J. Marnett. Prostaglandin endoperoxide synthase: structure and catalysis. *Biochimica et Biophysica Acta (BBA) - Lipids and Lipid Metabolism*, 1083:1–17, 1991.

- [34] W. L. Smith and R. Langenbach. Why there are two cyclooxygenase isozymes. *Journal of Clinical Investigation*, 107:1491–1495, 2001.
- [35] M. Sono, M. P. Roach, E. D. Coulter, and J. H. Dawson. Heme-containing oxygenases. *Chemical Reviews*, 96:2841–2887, 1996.
- [36] S. W. Rowlinson, B. C. Crews, C. A. Lanzo, and L. J. Marnett. The binding of arachidonic acid in the cyclooxygenase active site of mouse prostaglandin endoperoxide synthase-2 (COX-2). A putative L-shaped binding conformation utilizing the top channel region. *Journal of Biological Chemistry*, 274:23305–23310, 1999.
- [37] M. G. Malkowski, S. L. Ginell, W. L. Smith, and R. M. Garavito. The productive conformation of arachidonic acid bound to prostaglandin synthase. *Science*, 289:1933–1937, 2000.
- [38] R. G. Kurumbail, J. R. Kiefer, and L. J. Marnett. Cyclooxygenase enzymes: Catalysis and inhibition. *Current Opinion in Structural Biology*, 11:752–760, 2001.
- [39] C. Yuan, C. J. Rieke, G. Rimon, B. A. Wingerd, and W. L. Smith. Partnering between monomers of cyclooxygenase-2 homodimers. *Proceedings of the National Academy of Sciences*, 103:6142–6147, 2006.
- [40] C. Yuan, R. S. Sidhu, D. V. Kuklev, Y. Kado, M. Wada, I. Song, and W. L. Smith. Cyclooxygenase allostereism, fatty acid-mediated cross-talk between monomers of cyclooxygenase homodimers. *Journal of Biological Chemistry*, 284:10046–10055, 2009.

- [41] L. Dong, H. Zou, C. Yuan, Y. H. Hong, D. V. Kuklev, and W. L. Smith. Different fatty acids compete with arachidonic acid for binding to the allosteric or catalytic subunits of cyclooxygenases to regulate prostanoid synthesis. *Journal of Biological Chemistry*, 291:4069–4078, 2016.
- [42] A. L. Tsai, G. Wu, G. Palmer, B. Bambai, J. A. Koehn, P. J. Marshall, and R. J. Kulmacz. Rapid kinetics of tyrosyl radical formation and heme redox state changes in prostaglandin H synthase-1 and -2. *Journal of Biological Chemistry*, 274:21695–21700, 1999.
- [43] B. J. Orlando, P. P. Borbat, E. R. Georgieva, J. H. Freed, and M. G. Malkowski. Pulsed Dipolar Spectroscopy Reveals That Tyrosyl Radicals Are Generated in Both Monomers of the Cyclooxygenase-2 Dimer. *Biochemistry*, 54:7309–7312, 2015.
- [44] L. C. Hsi, C. W. Hoganson, G. T. Babcock, and W. L. Smith. Characterization of a tyrosyl radical in prostaglandin endoperoxide synthase-2. *Biochemical and Biophysical Research Communications*, 202:1592–1598, 1994.
- [45] T. Shimokawa, R. J. Kulmacz, D. L. DeWitt, and W. L. Smith. Tyrosine 385 of prostaglandin endoperoxide synthase is required for cyclooxygenase catalysis. *Journal of Biological Chemistry*, 265:20073–20076, 1990.
- [46] L. J. Marnett. Cyclooxygenase mechanisms. *Current Opinion in Chemical Biology*, 4:545–552, 2000.
- [47] P. J. Silva, P. A. Fernandes, and M. J. Ramos. A theoretical study of radical-only and combined radical/carbocationic mech-

- anisms of arachidonic acid cyclooxygenation by prostaglandin H synthase. *Theoretical Chemistry Accounts*, 110:345–351, 2003.
- [48] C. Schneider, W. E. Boeglin, S. Lai, J. K. Cha, and A. R. Brash. Synthesis and applications of stereospecifically 3H-labeled arachidonic acids as mechanistic probes for lipoxygenase and cyclooxygenase catalysis. *Analytical Biochemistry*, 284:125–135, 2000.
- [49] C. Schneider, D. A. Pratt, N. A. Porter, and A. R. Brash. Control of Oxygenation in Lipoxygenase and Cyclooxygenase Catalysis. *Chemistry & biology*, 14:473–488, 2007.
- [50] A. M. Dean and F. M. Dean. Carbocations in the synthesis of prostaglandins by the cyclooxygenase of PGH synthase? a radical departure! *Protein Science*, 8:1087–1098, 1999.
- [51] D. E. O'Connor, M. C. Coleman, and E. D. Mihelich. Stereochemical Course of the Autoxidative Cyclization of Lipid Hydroperoxides to Prostaglandin-like Bicyclo Endoperoxides. *Journal of the American Chemical Society*, 106:3577–3584, 1984.
- [52] P. Kwok, F. W. Muellner, and J. Fried. Enzymatic Conversions of 10,10-Difluoroarachidonic Acid with PGH Synthase and Soybean Lipoxygenase. *Journal of the American Chemical Society*, 109:3692–3698, 1987.
- [53] A. R. Navratil, M. S. Shchepinov, and E. A. Dennis. Lipidomics Reveals Dramatic Physiological Kinetic Isotope Effects during the Enzymatic Oxygenation of Polyunsaturated Fatty Acids Ex Vivo. *Journal of the American Chemical Society*, 140:235–243, 2018.

- [54] M. Hecker, V. Ullrich, C. Fischer, and C. O. Meese. Identification of novel arachidonic acid metabolites formed by prostaglandin H synthase. *European Journal of Biochemistry*, 169:113–123, 1987.
- [55] M. Lecomte, O. Laneuville, C. Ji, D. L. DeWitt, and W. L. Smith. Acetylation of human prostaglandin endoperoxide synthase-2 (cyclooxygenase-2) by aspirin. *The Journal of biological chemistry*, 269:13207–15, 1994.
- [56] G. Xiao, A. Tsai, G. Palmer, W. C. Boyar, P. J. Marshall, and R. J. Kulmacz. Analysis of Hydroperoxide-Induced Tyrosyl Radicals and Lipoxygenase Activity in Aspirin-Treated Human Prostaglandin H Synthase-2. *Biochemistry*, 36:1836–1845, 1997.
- [57] C. Schneider and A. R. Brash. Stereospecificity of hydrogen abstraction in the conversion of arachidonic acid to 15R-HETE by aspirin-treated cyclooxygenase-2. Implications for the alignment of substrate in the active site. *The Journal of biological chemistry*, 275:4743–6, 2000.
- [58] C. Schneider, W. E. Boeglin, J. J. Prusakiewicz, S. W. Rowlinson, L. J. Marnett, N. Samel, and A. R. Brash. Control of prostaglandin stereochemistry at the 15-carbon by cyclooxygenases-1 and -2: A critical role for serine 530 and valine 349. *Journal of Biological Chemistry*, 277:478–485, 2002.
- [59] S. W. Rowlinson, B. C. Crews, D. C. Goodwin, C. Schneider, J. K. Gierse, and L. J. Marnett. Spatial requirements for 15-(R)-hydroxy-5Z,8Z,11Z,13E-eicosatetraenoic acid synthesis within the cyclooxygenase active site of murine COX-2. Why acetylated COX-1 does not synthesize 15-(R)-HETE. *Journal of Biological Chemistry*, 275:6586–6591, 2000.

- [60] C. Schneider, W. E. Boeglin, and A. R. Brash. Identification of Two Cyclooxygenase Active Site Residues, Leucine 384 and Glycine 526, That Control Carbon Ring Cyclization in Prostaglandin Biosynthesis. *Journal of Biological Chemistry*, 279:4404–4414, 2004.
- [61] G. Carullo, F. Galligano, and F. Aiello. Structure-activity relationships for the synthesis of selective cyclooxygenase 2 inhibitors: an overview (2009-2016). *MedChemComm*, 8:492–500, 2017.
- [62] L. J. Marnett. The COXIB Experience: A Look in the Rearview Mirror. *Annual Review of Pharmacology and Toxicology*, 49:265–290, 2009.
- [63] D. P. Cronin-Fenton, U. Heide-Jørgensen, T. P. Ahern, T. L. Lash, P. Christiansen, B. Ejlersen, and H. T. Sørensen. Low-dose aspirin, nonsteroidal anti-inflammatory drugs, selective COX-2 inhibitors and breast cancer recurrence. *Epidemiology*, 27:586–593, 2016.
- [64] D. Y. Graham. Aspirin and Related Drugs. *Gastroenterology*, 129:1135–1136, 2005.
- [65] K. Schrör and M. Voelker. *NSAIDs and Aspirin: Recent advances and implications for clinical management*. Springer, Cham, 2016.
- [66] J. L. Masferrer, B. S. Zweifel, P. T. Manning, S. D. Hauser, K. M. Leahy, W. G. Smith, P. C. Isakson, and K. Seibert. Selective inhibition of inducible cyclooxygenase 2 in vivo is antiinflammatory and nonulcerogenic. *Proceedings of the National Academy of Sciences*, 91:3228–3232, 1994.

- [67] E. Pennisi. Building better aspirin: Does aspirin ward off cancer and Alzheimer's? *Science*, 280:1191–1192, 1998.
- [68] T. Shimokawa and W. L. Smith. Prostaglandin endoperoxide synthase. The aspirin acetylation region. *Journal of Biological Chemistry*, 267:12387–12392, 1992.
- [69] R. J. Flower. The development of COX2 inhibitors. *Nature Reviews Drug Discovery*, 2:179–191, 2003.
- [70] A. L. Blobaum and L. J. Marnett. Structural and functional basis of cyclooxygenase inhibition. *Journal of Medicinal Chemistry*, 50:1425–1441, 2007.
- [71] P. Tosco and L. Lazzarato. Mechanistic insights into cyclooxygenase irreversible inactivation by aspirin. *ChemMedChem*, 4: 939–945, 2009.
- [72] N. P Sharma, L. Dong, C. Yuan, K. R. Noon, and W. L Smith. Asymmetric acetylation of the cyclooxygenase-2 homodimer by aspirin and its effects on the oxygenation of arachidonic, eicosapentaenoic, and docosahexaenoic acids. *Molecular pharmacology*, 77:979–986, 2010.
- [73] C. N Serhan, T. Takano, and J. F. Maddox. Aspirin-triggered 15-epi-lipoxin A4 and stable analogs of lipoxin A4 are potent inhibitors of acute inflammation: Receptors and pathways. *Advances in Experimental Medicine and Biology*, 447:133–149, 1999.
- [74] N. Chiang, I. M. Fierro, K. Gronert, and C. N. Serhan. Activation of lipoxin A4 receptors by aspirin-triggered lipoxins and select peptides evokes ligand-specific responses in inflammation. *The Journal of experimental medicine*, 191:1197–208, 2000.

- [75] J. Nakano. Relationship between the chemical structure of prostaglandins and their vasoactivities in dogs. *British Journal of Pharmacology*, 44:63–70, 1972.
- [76] R. L. Spraggins. PGA₂ and isomers from coral prostaglandins. *Tetrahedron Letters*, 13:4343–4346, 1972.
- [77] A. L. Tsai, G. Palmer, G. Wu, S. Peng, N. M. Okeley, W. A. Van Der Donk, and Richard J Kulmacz. Structural characterization of arachidonyl radicals formed by aspirin-treated prostaglandin H synthase-2. *Journal of Biological Chemistry*, 277:38311–38321, 2002.
- [78] L. Dong, A. J. Anderson, and M. G. Malkowski. Arg-513 and Leu-531 Are Key Residues Governing Time-Dependent Inhibition of Cyclooxygenase-2 by Aspirin and Celebrex. *Biochemistry*, 58:3990–4002, 2019.
- [79] J. A. Giménez-Bastida, W. E. Boeglin, O. Boutaud, M. G. Malkowski, and C. Schneider. Residual cyclooxygenase activity of aspirin-acetylated COX-2 forms 15R-prostaglandins that inhibit platelet aggregation. *The FASEB Journal*, 33:1033–1041, 2019.
- [80] E. G. Lewars. *Computational chemistry : introduction to the theory and applications of molecular and quantum mechanics*. Springer, Cham, 2016.
- [81] F. Jensen. *Introduction to computational chemistry*. John Wiley & Sons Ltd, 2007.
- [82] F. H. Westheimer. A calculation of the energy of activation

- for the racemization of 2,2'-dibromo-4,4'-dicarboxydiphenyl. *The Journal of Chemical Physics*, 15:252–260, 1947.
- [83] T. L. Hill. On Steric Effects. *The Journal of Chemical Physics*, 14:465–465, 1946.
- [84] F. H. Westheimer and J. E. Mayer. The Theory of the Racemization of Optically Active Derivatives of Diphenyl. *The Journal of Chemical Physics*, 14:733–738, 1946.
- [85] C. J. Cramer. *Essentials of computational chemistry*. John Wiley & Sons, Ltd, 2006.
- [86] N. L. Allinger. Conformational analysis. 130. MM2. A hydrocarbon force field utilizing V1 and V2 torsional terms. *Journal of the American Chemical Society*, 99:8127–8134, 1977.
- [87] N. L. Allinger, F. Li, L. Yan, and J. C. Tai. Molecular mechanics (MM3) calculations on conjugated hydrocarbons. *Journal of Computational Chemistry*, 11:868–895, 1990.
- [88] N. L. Allinger, K. Chen, and J. Lii. An improved force field (MM4) for saturated hydrocarbons. *Journal of Computational Chemistry*, 17:642–668, 1996.
- [89] D. A. Pearlman, D. A. Case, J. W. Caldwell, W. S. Ross, T. E. Cheatham, S. DeBolt, D. Ferguson, G. Seibel, and P. Kollman. AMBER, a package of computer programs for applying molecular mechanics, normal mode analysis, molecular dynamics and free energy calculations to simulate the structural and energetic properties of molecules. *Computer Physics Communications*, 91:1–41, 1995.

- [90] B. R. Brooks, C. L. Brooks, A. D. Mackerell, L. Nilsson, R. J. Petrella, B. Roux, Y. Won, G. Archontis, C. Bartels, and et al. CHARMM: The biomolecular simulation program. *Journal of Computational Chemistry*, 30:1545–1614, 2009.
- [91] W. R. P. Scott, P. H. Hünenberger, I. G. Tironi, A. E. Mark, S. R. Billeter, J. Fennen, A. E. Torda, T. Huber, P. Krüger, and W. F. Van Gunsteren. The GROMOS biomolecular simulation program package. *Journal of Physical Chemistry A*, 103:3596–3607, 1999.
- [92] A. R. Leach. *Molecular modelling : principles and applications*. Pearson. Prentice Hall, 2001.
- [93] L. H. Thomas. On the Capture of Electrons by Swiftly Moving Electrified Particles. *Proceedings of the Royal Society A: Mathematical, Physical and Engineering Sciences*, 114:561–576, 1927.
- [94] E. Fermi. Statistical method to determine some properties of atoms. *Rend. Accad. Naz. Lincei*, 6:602–607, 1927.
- [95] P. Hohenberg and W. Kohn. In homogeneous electron gas. *Physical Review*, 136:B864–B871, 1964.
- [96] W. Kohn and L. J. Sham. Self-consistent equations including exchange and correlation effects. *Physical Review*, 140:A1133–A1138, 1965.
- [97] A. D. Becke. A new mixing of Hartree-Fock and local density-functional theories. *The Journal of Chemical Physics*, 98:1372–1377, 1993.

- [98] P. J. Stephens, F. J. Devlin, C. F. Chabalowski, and M. J. Frisch. Ab Initio calculation of vibrational absorption and circular dichroism spectra using density functional force fields. *The Journal of Physical Chemistry*, 98:11623–11627, 1994.
- [99] A. D. Becke. Density-functional exchange-energy approximation with correct asymptotic behavior. *Physical Review A*, 38:3098–3100, 1988.
- [100] C. Lee, W. Yang, and R. G. Parr. Development of the Colle-Salvetti correlation-energy formula into a functional of the electron density. *Physical Review B*, 37:785–789, 1988.
- [101] S. H. Vosko, L. Wilk, and M. Nusair. Accurate spin-dependent electron liquid correlation energies for local spin density calculations: a critical analysis. *Canadian Journal of Physics*, 58:1200–1211, 1980.
- [102] A. Warshel and M. Levitt. Theoretical studies of enzymic reactions: Dielectric, electrostatic and steric stabilization of the carbonium ion in the reaction of lysozyme. *Journal of Molecular Biology*, 103:227–249, 1976.
- [103] M. J. Field, P. A. Bash, and M. Karplus. A combined quantum mechanical and molecular mechanical potential for molecular dynamics simulations. *Journal of Computational Chemistry*, 11:700–733, 1990.
- [104] H. M. Senn and W. Thiel. QM/MM Methods for Biomolecular Systems. *Angewandte Chemie International Edition*, 48:1198–1229, 2009.

- [105] H. M. Senn and W. Thiel. QM/MM studies of enzymes. *Current Opinion in Chemical Biology*, 11:182–187, 2007.
- [106] D. Balcells, G. Drudis-Solé, M. Besora, N. Dölker, G. Ujaque, F. Maseras, and A. Lledós. Some critical issues in the application of quantum mechanics/molecular mechanics methods to the study of transition metal complexes. *Faraday Discuss.*, 124:429–441, 2003.
- [107] Y. Shiota, K. Suzuki, and K. Yoshizawa. QM/MM study on the catalytic mechanism of benzene hydroxylation over Fe-ZSM-5. *Organometallics*, 25:3118–3123, 2006.
- [108] S. A. French, A. A. Sokol, S. T. Bromley, C. R. A. Catlow, S. C. Rogers, F. King, and P. Sherwood. From CO₂ to methanol by hybrid QM/MM embedding. *Angewandte Chemie - International Edition*, 40:4437–4440, 2001.
- [109] P. Sherwood, A. H. de Vries, M. F. Guest, G. Schreckenbach, C. R. A. Catlow, S. A. French, A. A. Sokol, S. T. Bromley, W. Thiel, A. J. Turner, S. Billeter, and et al. QUASI: A general purpose implementation of the QM/MM approach and its application to problems in catalysis. *Journal of Molecular Structure: THEOCHEM*, 632:1–28, 2003.
- [110] M. Karplus. Development of Multiscale Models for Complex Chemical Systems: From H+H₂ to Biomolecules (Nobel Lecture). *Angewandte Chemie International Edition*, 53:9992–10005, 2014.
- [111] M. Levitt. Birth and future of multiscale modeling for macromolecular systems (Nobel Lecture). *Angewandte Chemie - International Edition*, 53:10006–100018, 2014.

- [112] H. Hirao, K. Xu, P. Chuanprasit, A. M. P. Moeljadi, and K. Morokuma. Key concepts and applications of oniom methods, chap.8. In I. Tuñón and V. Moliner, editors, *Simulating Enzyme Reactivity: Computational Methods in enzyme Catalysis*. Royal Society of Chemistry, 2016.
- [113] L. W. Chung, W. M. C. Sameera, R. Ramozzi, A. J. Page, M. Hatanaka, G. P. Petrova, T. V. Harris, X. Li, Z. Ke, F. Liu, H. B. Li, L. Ding, and K. Morokuma. The ONIOM Method and Its Applications. *Chemical Reviews*, 115:5678–5796, 2015.
- [114] P. Sherwood and et al. Chemshell, a Computational Chemistry Shell. URL <https://www.chemshell.org/>.
- [115] S. Metz, J. Kästner, A. A. Sokol, T. W. Keal, and P. Sherwood. ChemShell-a modular software package for QM/MM simulations. *WIREs Computational Molecular Science*, 4:101–110, 2014.
- [116] P. Sherwood, A. H. de Vries, S. J. Collins, S. P. Greatbanks, N. A. Burton, M. A. Vincent, and I. H. Hillier. Computer simulation of zeolite structure and reactivity using embedded cluster methods. *Faraday Discussions*, 106:79–92, 1997.
- [117] V. Théry, D. Rinaldi, J. Rivail, B. Maigret, and G. G. Ferenczy. Quantum mechanical computations on very large molecular systems: The local self-consistent field method. *Journal of Computational Chemistry*, 15:269–282, 1994.
- [118] N. Ferré, X. Assfeld, and J. L. Rivail. Specific force field parameters determination for the hybrid ab initio QM/MM LSCF method. *Journal of Computational Chemistry*, 23:610–624, 2002.

- [119] R. B. Murphy, D. M. Philipp, and R. A. Friesner. A Mixed Quantum Mechanics/Molecular Mechanics (QM/MM) Method for Large-Scale Modeling of Chemistry in Protein Environments. *Journal of Computational Chemistry*, 21:1442–1457, 2000.
- [120] D. M. Philipp and R. A. Friesner. Mixed ab initio QM/MM modeling using frozen orbitals and tests with alanine dipeptide and tetrapeptide. *Journal of Computational Chemistry*, 20:1468–1494, 1999.
- [121] R. B. Murphy, D. M. Philipp, and R. A. Friesner. Frozen orbital QM/MM methods for density functional theory. *Chemical Physics Letters*, 321:113–120, 2000.
- [122] J. Gao, P. Amara, C. Alhambra, and M. J. Field. A generalized hybrid orbital (GHO) method for the treatment of boundary atoms in combined QM/MM calculations. *Journal of Physical Chemistry A*, 102:4714–4721, 1998.
- [123] P. Amara, M. J. Field, C. Alhambra, and J. Gao. The generalized hybrid orbital method for combined quantum mechanical/molecular mechanical calculations: Formulation and tests of the analytical derivatives. *Theoretical Chemistry Accounts*, 104:336–343, 2000.
- [124] J. Pu, J. Gao, and D. G. Truhlar. Generalized Hybrid-Orbital Method for Combining Density Functional Theory with Molecular Mechanicals. *ChemPhysChem*, 6:1853–1865, 2005.
- [125] G. W. Frisch, G. W. Trucks, H. B. Schlegel, G. E. Scuseria, M. A. Robb, J. R. Cheeseman, G. Scalmani, V. Barone, B. Menucci, G. A. Petersson, and et al. *Gaussian 09*. Gaussian, Inc., Wallingford CT, 2009.

- [126] W. Smith and T. R. R. Forester. DL-POLY-2.0: A general-purpose parallel molecular dynamics simulation package. *Journal of Molecular Graphics*, 14:136–141, 1996.
- [127] S. R. Billeter, A. J. Turner, and W. Thiel. Linear scaling geometry optimisation and transition state search in hybrid delocalised internal coordinates. *Physical Chemistry Chemical Physics*, 2: 2177–2186, 2000.
- [128] J. Kästner, J. M. Carr, T. W. Keal, W. Thiel, A. Wander, and P. Sherwood. D1-find: An open-source geometry optimizer for atomistic simulations. *The Journal of Physical Chemistry A*, 113:11856–11865, 2009.
- [129] D. C. Liu and J. Nocedal. On the limited memory BFGS method for large scale optimization. *Mathematical Programming*, 45:503–528, 1989.
- [130] A. Banerjee, N. Adams, J. Simons, and R. Shepard. Search for stationary points on surfaces. *The Journal of Physical Chemistry*, 89:52–57, 1985.
- [131] J. Kästner, S. Thiel, H. M. Senn, P. Sherwood, and W. Thiel. Exploiting QM/MM Capabilities in Geometry Optimization: A Microiterative Approach Using Electrostatic Embedding. *Journal of Chemical Theory and Computation*, 3:1064–1072, 2007.
- [132] S. Dapprich, I. Komáromi, K. S. Byun, K. Morokuma, and M. J. Frisch. A new ONIOM implementation in Gaussian98. Part I. The calculation of energies, gradients, vibrational frequencies and electric field derivatives. *Journal of Molecular Structure: THEOCHEM*, 461-462:1–21, 1999.

- [133] M. Svensson, S. Humbel, R. D. J. Froese, T. Matsubara, S. Sieber, and K. Morokuma. ONIOM: A Multilayered Integrated MO+MM Method for Geometry Optimizations and Single Point Energy Predictions. A Test for Diels-Alder Reactions and Pt(P(t-Bu)₃)₂+H₂ Oxidative Addition. *The Journal of Physical Chemistry*, 100:19357–19363, 1996.
- [134] T. Vreven, K. S. Byun, I. Komáromi, S. Dapprich, J. A. Montgomery, K. Morokuma, and M. J. Frisch. Combining Quantum Mechanics Methods with Molecular Mechanics Methods in ONIOM. *Journal of Chemical Theory and Computation*, 2:815–826, 2006.
- [135] T. Vreven, K. Morokuma, O. Farkas, H. B. Schlegel, and M. J. Frisch. Geometry optimization with QM/MM, ONIOM, and other combined methods. I. Microiterations and constraints. *Journal of Computational Chemistry*, 24:760–769, 2003.
- [136] T. Vreven, M. J. Frisch, K. N. Kudin, H. B. Schlegel, and K. Morokuma. Geometry optimization with QM/MM methods II: Explicit quadratic coupling. *Molecular Physics*, 104:701–714, 2006.
- [137] B. J. Alder and T. E. Wainwright. Phase transition for a hard sphere system. *The Journal of Chemical Physics*, 27:1208–1209, 1957.
- [138] J. A. McCammon, B. R. Gelin, and M. Karplus. Dynamics of folded proteins. *Nature*, 267:585–590, 1977.
- [139] V. V. Kindratenko, J. J. Enos, G. Shi, M. T. Showerman, G. W. Arnold, J. E. Stone, J. C. Phillips, and W. Hwu. GPU clusters for high-performance computing. In *IEEE International Conference on Cluster Computing and Workshops*, 2009.

- [140] J. Glaser, T. D. Nguyen, J. A. Anderson, P. Lui, F. Spiga, J. A. Millan, D. C. Morse, and S. C. Glotzer. Strong scaling of general-purpose molecular dynamics simulations on GPUs. *Computer Physics Communications*, 192:97–107, 2015.
- [141] S. Le Grand, A. W. Götz, and R. C. Walker. SPFP: Speed without compromise-A mixed precision model for GPU accelerated molecular dynamics simulations. *Computer Physics Communications*, 184:374–380, 2013.
- [142] J. C. Phillips, J. E. Stone, and K. Schulten. Adapting a message-driven parallel application to GPU-accelerated clusters. In *SC'08: Proceedings of the 2008 ACM/IEEE Conference on Supercomputing*, 2008.
- [143] L. Verlet. Computer "Experiments" on Classical Fluids. I. Thermodynamical Properties of Lennard-Jones Molecules. *Physical Review*, 159:98–103, 1967.
- [144] R. W. Hockney. The potential calculation and some applications. *Methods in Computational Physics*, 9:135–211, 1970.
- [145] W. C. Swope, H. C. Andersen, P. H. Berens, and K. R. Wilson. A computer simulation method for the calculation of equilibrium constants for the formation of physical clusters of molecules: Application to small water clusters. *The Journal of Chemical Physics*, 76:637–649, 1982.
- [146] R. Salomon-Ferrer, A. W. Götz, D. Poole, S. Le Grand, and R. C. Walker. Routine Microsecond Molecular Dynamics Simulations with AMBER on GPUs. 2. Explicit Solvent Particle Mesh Ewald. *Journal of Chemical Theory and Computation*, 9:3878–3888, 2013.

- [147] J. P. Ryckaert, G. Ciccotti, and H. J. C. Berendsen. Numerical integration of the cartesian equations of motion of a system with constraints: molecular dynamics of n-alkanes. *Journal of Computational Physics*, 23:327–341, 1977.
- [148] H. Lei, N. A. Baker, and X. Li. Data-driven parameterization of the generalized Langevin equation. *Proceedings of the National Academy of Sciences*, 113:14183–14188, 2016.
- [149] H. J. C. Berendsen, J. P. M. Postma, W. F. Van Gunsteren, A. Dinola, and J. R. Haak. Molecular dynamics with coupling to an external bath. *The Journal of Chemical Physics*, 81:3684–3690, 1984.
- [150] W. F. van Gunsteren and H. J. C. Berendsen. Computer Simulation of Molecular Dynamics: Methodology, Applications, and Perspectives in Chemistry. *Angewandte Chemie International Edition in English*, 29:992–1023, 1990.
- [151] S. Peng, N. M. Okeley, A. L. Tsai, G. Wu, R. J. Kulmacz, and W. A. Van der Donk. Synthesis of isotopically labeled arachidonic acids to probe the reaction mechanism of prostaglandin H synthase. *Journal of the American Chemical Society*, 124:10785–10796, 2002.
- [152] S. F. Oh, T. W. Vickery, and C. N. Serhan. Chiral lipidomics of E-series resolvins: Aspirin and the biosynthesis of novel mediators. *Biochimica et Biophysica Acta - Molecular and Cell Biology of Lipids*, 1811:737–747, 2011.
- [153] S. F. Oh, P. S. Pillai, A. Recchiuti, R. Yang, and C. N. Serhan. Pro-resolving actions and stereoselective biosynthesis of 18S E-

- series resolvins in human leukocytes and murine inflammation. *Journal of Clinical Investigation*, 121:569–581, 2011.
- [154] J. A. Maier, C. Martinez, K. Kasavajhala, L. Wickstrom, K. E. Hauser, and C. Simmerling. ff14SB: Improving the Accuracy of Protein Side Chain and Backbone Parameters from ff99SB. *Journal of Chemical Theory and Computation*, 11:3696–3713, 2015.
- [155] D. A. Case, V. Babin, J. T. Berryman, R. M. Betz, Q. Cai, D. S. Cerutti, T. E. Cheatham, T. A. Darden, R. E. Duke, H. Gohlke, and et al. *Amber 14- Reference Manual*, 2014.
- [156] W. L. Jorgensen, J. Chandrasekhar, J. D. Madura, R. W. Impey, and M. L. Klein. Comparison of simple potential functions for simulating liquid water. *The journal of chemical Physics*, 79: 926–935, 1983.

Article I



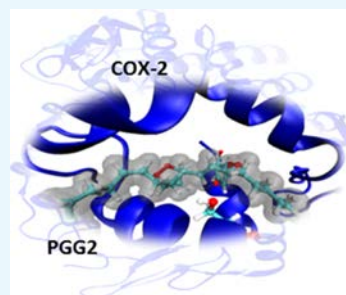
Unraveling the Molecular Details of the Complete Mechanism That Governs the Synthesis of Prostaglandin G2 Catalyzed by Cyclooxygenase-2

Anna Cebrián-Prats,[†] Àngels González-Lafont,^{†,‡,§} and José M. Lluch^{*,†,‡,§}

[†]Departament de Química and [‡]Institut de Biotecnologia i de Biomedicina (IBB), Universitat Autònoma de Barcelona, Bellaterra, 08193 Barcelona, Spain

Supporting Information

ABSTRACT: Cyclooxygenase-2 (COX-2) is the key enzyme involved in the synthesis pathway of prostaglandin G2 (PGG2) by transformation of arachidonic acid (AA). Although COX-2 is one of the principal pharmacological targets by the implication of PGG2 in several human diseases, the classical all-radical mechanism proposed for COX-2 catalysis has never been validated at the molecular level. Herein, molecular dynamics simulations and quantum mechanics/molecular mechanics (QM/MM) calculations were combined to analyze the six steps of the all-radical mechanism. The results show that O₂ addition on C₁₁ of AA can follow an antarafacial or suprafacial approach with respect to tyrosine 385, but only the antarafacial addition leads to the product with the correct 11R stereochemistry as established in the mechanistic proposal. Moreover, only the reaction pathway coming from the antarafacial intermediate describes a viable 8,12-cyclization to form the prostaglandin-like bicyclo endoperoxide that finally leads, by kinetic control, to PGG2 with the 15S stereochemistry found experimentally. The formation of the more stable trans ring isomer of natural PGG2 in an enzymatic environment is also explained. Our molecular analysis shows how COX-2 uses its relatively narrow channel in the active site to restrain certain conformational changes of AA and of the reaction intermediates, so that the PGG2 enzymatic synthesis turns out to be highly regiospecific and stereospecific. A more recent 10-step carbocation-based mechanistic proposal has been discarded.

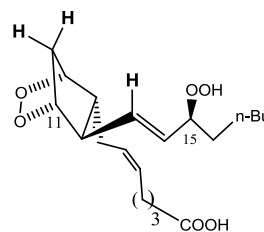


1. INTRODUCTION

Cyclooxygenase-2 (COX-2) is a membrane-associated homodimeric bifunctional hemoprotein that catalyzes the oxygenation of several polyunsaturated fatty acids.¹ Arachidonic acid (AA, 20:4 n-6), released from phospholipid membranes, is its main substrate leading to the generation of prostaglandins, whose production is associated to many human pathologies, including inflammation, cardiovascular diseases, and cancer.² COX-2 has a crucial relevance in pharmacology because it is a target of the nonsteroidal anti-inflammatory drugs such as, for instance, aspirin, ibuprofen, and diclofenac, thus producing the well-known analgesic, antipyretic, and anti-inflammatory effects.^{3–8}

Each monomer has two mechanistically coupled, spatially distinct active sites.¹ AA binds within the cyclooxygenase active site at the end of a hydrophobic channel that extends up to the membrane-binding region. After C₁₃ hydrogen abstraction from AA, the addition of two O₂ molecules converts AA to prostaglandin G2 (PGG2; see Scheme 1). PGG2 is then released to the heme-containing peroxidase active site located near the protein surface, where its 15-hydroperoxide group is reduced to give prostaglandin H2 (PGH2). The peroxidase activity can work independently of the cyclooxygenase one.² Conversely, cyclooxygenase activity is peroxide-dependent. In the resting state of COX-2, the peroxidase active site contains a

Scheme 1. Prostaglandin G2 (PGG2)



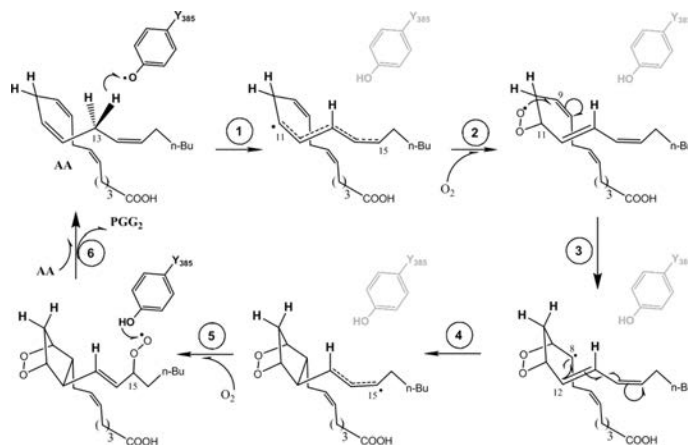
Fe³⁺-protoporphyrin IX group.⁹ An alkyl hydroperoxide activates the heme group by means of a two-electron oxidation, yielding the corresponding alcohol and an oxy-ferryl protoporphyrin IX radical cation, which, in turn, is reduced by an intramolecular electron transfer from the Tyr385 placed in the cyclooxygenase active site. The so-formed tyrosyl radical initiates the catalytic cycle in the cyclooxygenase active site when the substrate AA occupies this site. Electron para-

Received: December 20, 2018

Accepted: December 31, 2018

Published: January 25, 2019

Scheme 2. All-Radical Mechanism

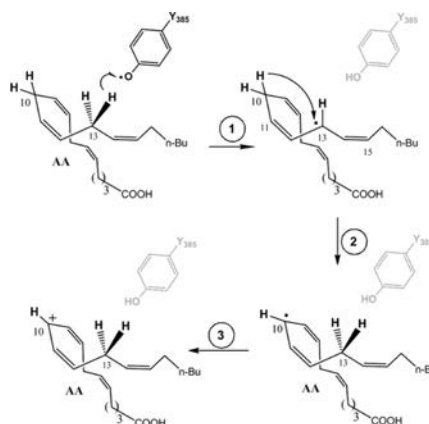


magnetic resonance spectroscopy shows the formation of Tyr385 radical after the addition of an alkyl hydroperoxide^{9,10} and the appearance of an arachidonate radical following the addition of AA.¹⁰

So far, the only existing unambiguous crystal structure of AA bound in the cyclooxygenase active site of COX-2 in a productive conformation^{1,11} corresponds to its complex with the Co³⁺-protoporphyrin IX-reconstituted murine COX-2 (muCOX-2-AA complex; PDB code 3HSS) determined to 2.1 Å that lacks both peroxidase and cyclooxygenase activities. There are no significant structural differences between both enzyme monomers A and B, although AA adopts very different conformations within the cyclooxygenase active sites of each monomer. Very interestingly, AA in monomer A exhibits a nonproductive binding mode (unable to react) with the AA carboxylate interacting with Tyr385 and Ser530 at the apex of the channel. Conversely, an “L-shaped” productive binding configuration of AA is observed in monomer B such that the AA carboxylate lies near the side chains of Arg120 and Tyr355 at the opening of the channel, whereas the AA ω -end is encased by residues Phe205, Phe209, Val228, Val344, Phe381, and Leu534 that form a hydrophobic groove above Ser530. The C₁₃ carbon atom of AA is positioned 2.95 Å below the phenolic oxygen of Tyr385, ready to start the cyclooxygenase reaction by abstraction of a C₁₃ hydrogen. This way, only one monomer (the catalytic one) of the COX-2 homodimer is active at a given time.¹²

There is a general agreement^{13–15} about the mechanism that rules such an important enzyme reaction in the cyclooxygenase active site. The classical six-step all-radical mechanism (see Scheme 2) derives from proposals by Hamberg and Samuelsson more than 50 years ago.^{16–19} After a C₁₃ hydrogen abstraction from AA by a tyrosyl radical, a delocalized C₁₁–C₁₅ pentadienyl radical is generated (step 1). An antarafacial O₂ addition at C₁₁ yields a 11R peroxy radical (step 2), which yields a C₈-radical cyclic endoperoxide by means of a 9,11-cyclization (step 3). Step 4 consists of an 8,12-cyclization leading to a bicyclo endoperoxide and a C₁₃–C₁₅ allyl radical. A second O₂ addition at the 15S position (step 5) and a back hydrogen transfer from Tyr385 to the peroxy radical at C₁₅ (step 6) finally give PGG₂.

However, Dean and Dean¹⁰ proposed later an alternative 10-step carbocation-based mechanism. After C₁₃ hydrogen abstraction from AA, a sigmatropic hydrogen transfer from C₁₀ to C₁₃ takes place, forming a delocalized C₈–C₁₂ pentadienyl radical, followed by an electron transfer from C₁₀ to the heme group, thus producing a carbocation at C₁₀ (see Scheme 3). Then, an 8,12-cyclization, a back electron transfer

Scheme 3. Formation of the Carbocation in C₁₀ according to the Carbocation-Based Mechanism

from the heme group to C₁₁, an O₂ addition at C₁₁, a 9,11-cyclization, a hydrogen transfer from C₁₃ to C₁₀, a second O₂ addition at C₁₅ and finally a back hydrogen transfer from Tyr385 to the peroxy radical at C₁₅ lead to PGG₂. Several important points that Dean and Dean argued in favor of their carbocation-based mechanism were:

- a Autoxidative cyclization of polyunsaturated fatty acid hydroperoxides in solution to form prostaglandin-like bicyclo endoperoxides through an all-radical mechanism highly favors *cis*-disubstituted cyclopentane isomers,²⁰ in clear opposition to the *trans* isomers corresponding to the natural prostaglandins generated by COX-2.

- b If 10,10-difluoroarachidonic acid is the substrate, COX enzymes do not generate any cyclic prostaglandin-like products, but acyclic alcohols such as 10,10-difluoro-11S-hydroxyeicosatetraenoic acid.²¹ Thus, it seems that the existence of hydrogen atoms at C₁₀ would be required for the formation of prostaglandins.
- c Chirality at C₁₅ is supposed to be better explained when the C₁₀–C₁₃ hydrogen shift occurs.

Very recently, Navratil et al.²² have studied the ex vivo deuterium isotope effect for the enzymatic oxidation (by COXs and lipoxygenases) of AA by macrophages. They have found that deuteration of C₁₀ promotes the formation of Lipoxin B₄, likely by interfering with AA cyclization and shunting AA to the lipoxygenase pathway under physiological conditions.

To compare at a detailed molecular level the two different mechanisms explained above, in this work we present the first theoretical study of the complete mechanism of reaction corresponding to the conversion of AA to PGG₂ catalyzed by the enzyme COX-2. To this aim, we have combined molecular dynamics simulations with quantum mechanics/molecular mechanics (QM/MM) calculations. We have devoted special attention to the analysis of the rearrangements of the AA inside the active site of COX-2 along the different steps of the mechanism and to the understanding of how COX-2 manages to get the catalytic control of the stereoselectivity and the regioselectivity of the reaction.

2. COMPUTATIONAL METHODS

2.1. System Setup. The first step of this study consists in the setup of the heme-containing homodimer enzyme COX-2 interacting with AA. To begin with, we built the enzyme based on the murine COX-2–AA complex (PDB code 3HSS),¹ in which the protoporphyrin IX group is complexed to a Co³⁺ and the homodimer presents AA interacting in different conformations in each monomer. Co³⁺ was replaced by Fe³⁺, and the heme prosthetic group was tethered to the axial histidine ligand (His388) in order to prevent the dissociation from the complex during the simulation.

Concerning the AA structure, only the monomer B exhibits the productive binding configuration, whereas the inverted orientation of the substrate is observed in monomer A in the cyclooxygenase channel. It is important to note that the productive orientation places the C₁₃ of AA near the Tyr385 allowing the abstraction of a C₁₃ hydrogen. We therefore decide to model only monomer B in order to study in detail each step of the catalytic mechanism. The AMBER ff14SB force field²³ was employed to define the protein residues, and the missing hydrogen atoms were added using the leap module of AMBER14²⁴ assuming a standard pH = 7 for the titrable residues. Five Na⁺ ions were added into the protein surface to neutralize the total charge of the system. The total system was solvated in a cubic box of TIP3P water molecules²⁵ of dimensions 91.1 Å × 101.2 Å × 87.7 Å. The size of the cubic box was created considering a minimum cutoff of 15 Å between the atoms of the enzyme and the edge of the periodic box, removing all the water molecules closer than 2.2 Å to any atom of the protein or the substrate. The resulting system contains about 80 600 atoms.

2.2. Parameterization. The partial atomic charges of the ferric penta-coordinate high spin group (Fe³⁺) were obtained from the restrained electrostatic potential (RESP)²⁶ method at the HF/6-31G(d,p) level of theory. Then, the heme

parameters were taken from a recent study²⁷ and the axial histidine parameters were described by the general AMBER force field (GAFF)²⁸ using the residuegen and parmchk module of AMBER14.²⁴ Concerning the AA, the parameters of its delocalized C₁₁–C₁₅ pentadienyl radical and its delocalized C₁₃–C₁₅ allyl radical were taken from a recent study.⁴

To parameterize the 10,10-difluoroarachidonic acid radical delocalized over the C₁₁–C₁₅ pentadienyl system, we calculated the partial atomic charges using the RESP method at the HF/6-31G(d,p) level of theory. Then, the parameters were obtained using the antechamber and parmchk module of AMBER14, combining them with some analogous parameters corresponding to the AA radical delocalized over the C₁₁–C₁₅ pentadienyl system.

Finally, the parameterization of the tyrosyl radical was performed starting with the optimization of the residue using the B3LYP functional^{29,30} and the 6-31G(d,p)^{31,32} basis set for all atoms and then calculating the partial atomic charges by using the RESP method at the B3LYP/6-31G(d,p) level of theory with Gaussian09.³³ The energy term corresponding to a stretching of a bond or a bending of an angle in the AMBER force field consist of a harmonic function that depends on a force constant. Then, the force constants associated to each bond or angle of the tyrosyl radical have been fitted to reproduce the B3LYP/6-31G(d,p) potential energy profiles generated for the corresponding stretching or bending. In this case, the dihedral parameters have not been calculated, because they do not present any differences with respect to the tyrosine. The van der Waals parameters were taken from the GAFF force field of AMBER14, considering the oxygen radical as an ether or ester oxygen.

2.3. Molecular Dynamics Simulations. After proper setup and parameterization, the resulting systems with AA within the cyclooxygenase active site, including Tyr385 and the radical Tyr385 of monomer B of COX-2, were minimized following three MM minimization steps using the steepest descent and conjugate gradient methods. In the first step, we have applied harmonic restraints on the enzyme, heme prosthetic group, and the substrate, keeping the solvation waters free. In the second step, only the substrate and the heme prosthetic group have been restrained. The final minimization protocol was carried out applying restraints only on the protein side chains, the remaining system being free.

Then, two MD simulations have been performed under periodic boundary conditions, the first one including Tyr385 and the second one with the radical Tyr385. In both cases, the Michaelis complex was gradually heated from 0 to 300 K under the NVT ensemble (using Langevin dynamics),³⁴ along 200 ps with a weak restrain of 5 kcal mol⁻¹ Å⁻² over the heme prosthetic group and the substrate. Starting from the last configuration of the NVT ensemble, a simulation of the system under the NPT ensemble was performed to control its density. Thus, we have carried out four steps of 10 ps at 300 K and 1 atm of pressure (using an isotropic weak-coupling algorithm and the Berendsen barostat)³⁵ with a weak restrain on the residues side chains and then one last longer step of 160 ps to reach a density of the system around 1 g cm⁻³ (see Figure 1).

From the last configuration of the NPT ensemble (and, therefore, taking the final volume corresponding to 1 atm of pressure), an equilibration of 10 ns and the production simulation of 100 ns have been performed at 300 K using the NVT ensemble without any restraints. Along the MD, the covalent bonds containing hydrogen were constrained using

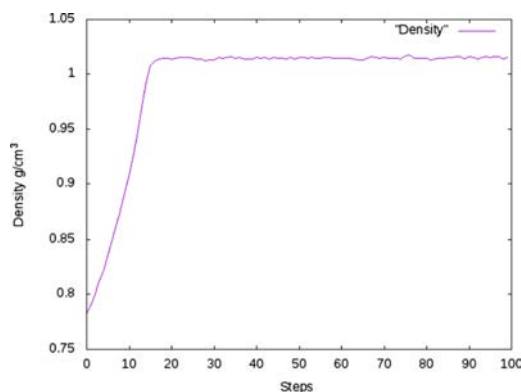


Figure 1. Evolution of the density along the NPT MD simulation of the COX-2-AA Michaelis complex including Tyr385. Each step stands for 2 ps.

the SHAKE algorithm,³⁶ and the particle-mesh Ewald method³⁷ was used to treat long-range electrostatic interactions. The simulation was performed using the AMBER 14 GPU (CUDA) version of the PMEMD package.^{38,39} A time step of 2 fs has been used in all cases.

2.4. Quantum Mechanics/Molecular Mechanics Calculations. Representative snapshots of the MD simulation were used to perform the QM/MM calculations of each step of the catalytic mechanism. The QM/MM calculations were performed using the modular program package ChemShell,^{40,41} combining Gaussian09 for the QM part and the DL_POLY module⁴² in ChemShell for the MM part.

The AMBER force field was employed for the MM region and the electrostatic embedding scheme⁴³ was used in all calculations to consider the polarizing effect of the enzyme over the QM region. Moreover, hydrogen link atoms have been employed to treat the QM/MM boundary with the charge-shift model,⁴⁴ and no cutoffs were introduced for the nonbonding MM and QM/MM interactions.

QM/MM optimizations were carried out employing the limited-memory Broyden-Fletcher-Goldfarb-Shanno (L-BFGS) algorithm⁴⁵ for energy minimizations. To build the potential energy profiles, a series of optimizations have been carried out imposing harmonic restrictions on the reaction coordinate, which, in general, increases with a step size of 0.2 Å. For the transition state search, a combination of the partitioned rational function optimizer⁴² and the L-BFGS was used. These algorithms are implemented in the HDLCopt (Hybrid Delocalized Internal Coordinate Scheme)⁴² module of Chemshell.

For each snapshot taken from the MD simulation, the corresponding QM/MM system includes all residues of the monomer B of COX-2, the complete AA and the 500 water molecules closer to C₁₁ of AA (roughly 10400 atoms). All residues and water molecules within a 15 Å radius sphere centered on C₁₁, and including the complete AA, define the active region (around 2000 atoms) in which all atoms move freely during the optimization processes, whereas the rest of the system has been kept frozen.

In all calculations, the QM region was treated using the B3LYP hybrid functional and the 6-31G(d,p) basis set for all atoms. This subsystem presents different sizes depending on

the particular step studied (see Figure S1). Because the Fe atom is in the peroxidase active site, it has been included in the MM region. Then, a doublet multiplicity has been imposed for the calculations of all reaction steps. For the reaction steps corresponding to an O₂ addition, we have checked (see Table S1) that the O₂ molecule has been introduced having a triplet character. The VMD program⁴⁶ has been used to generate the pictures of molecules.

3. RESULTS AND DISCUSSION

3.1. Molecular Dynamics Simulations. Some time ago, two previous^{47,48} 10 ns MD simulations of the COX2-AA and COX2-AA C₁₃ radical complexes by Furse et al. showed the importance of dynamics to describe the features of these systems. In the present work, as explained above, after equilibration a 100 ns MD simulation of AA within the cyclooxygenase active site including Tyr385 of monomer B of COX-2 has been carried out. The root mean-square deviation (RMSD) of the protein α -carbons with respect to the first structure (see Figure 2) clearly shows that the protein is equilibrated, especially if the N-terminal region is not considered.

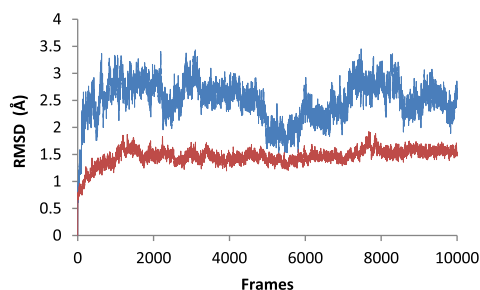


Figure 2. RMSD of the protein α -carbons (blue line) and excluding the ones corresponding to the N-terminal domain (red line) with respect to the first structure along the 100 ns MD simulation of AA within the cyclooxygenase active site including Tyr385 of monomer B of COX-2. A frame has been taken each 10 ps.

From here on H_{13A} will stand for the hydrogen of AA that will be abstracted. Then, we have followed (see Figure 3) the evolution of the distances H_{13A}-OTyr385 and C₁₃-OTyr385 along the simulation. In practical, all the frames $d(\text{H}_{13\text{A}}-\text{OTyr385}) > d(\text{C}_{13}-\text{OTyr385})$ along the first 90 ns, although this relation is reversed in the last 10 ns. In order to check how these distances change along longer MD simulations we have carried out an additional 50 ns simulation. As seen in Figure S2, no significant variation occurs within the time interval 100–150 ns.

Taking one structure each 10 ps along the first 100 ns MD simulations and filtering them according to the conditions $d(\text{H}_{13\text{A}}-\text{OTyr385}) \leq 3 \text{ \AA}$ and $d(\text{H}_{13\text{A}}-\text{OTyr385}) < d(\text{C}_{13}-\text{OTyr385})$, we have selected those structures having characteristics adequate to initiate the reactive processes. The second condition ensures that the corresponding C₁₃-H_{13A} bond is properly oriented for the hydrogen abstraction. This way we have obtained 706 snapshots, which we call precatalytic structures, ready to react as soon as the tyrosyl radical is formed. To facilitate the analysis of the binding modes, these snapshots have been clustered using a RMSD of 1.3 Å for the

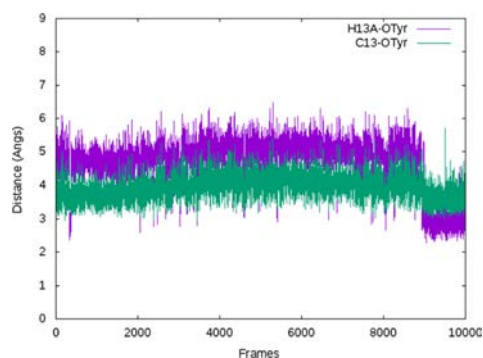


Figure 3. Evolution of the distances H_{13A} –OTyr385 (purple line) and C_{13} –OTyr385 (green line) along the 100 ns MD simulation of AA within the cyclooxygenase active site including Tyr385 of monomer B of COX-2. A frame has been taken each 10 ps.

heavy atoms of AA. The two more populated clusters have been represented in Figure 4. Our MD simulation reproduces

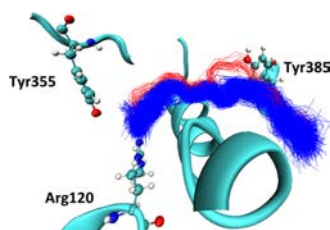


Figure 4. Two more populated clusters (the first one in blue, the second one in red) of the precatalytic structures using a RMSD of 1.3 Å for the heavy atoms of AA.

very well the “L-shaped” productive binding configuration of AA as observed in the above mentioned crystal structure by Vecchio et al.¹ The AA carboxylate lies near the side chains of Arg120 and Tyr355 at the opening of the channel, whereas the AA ω -end extends along the hydrophobic groove above Ser530, with the C_{13} carbon atom of AA located below and near the phenolic oxygen of Tyr385.

On the other hand, given that the peroxidase cycle occurs independently of the cyclooxygenase activity, AA could occupy the cyclooxygenase site already containing a tyrosyl radical. Then, we have also run a 100 ns MD simulation of AA within the cyclooxygenase active site including the Tyr385* radical of monomer B of COX-2. The analysis of the evolution of the distances H_{13A} –*OTyr385 and C_{13} –*OTyr385 along the simulation (see Figure S3) shows structures ready to react similar to the ones obtained with Tyr385.

Table 1. Distances (Å) Relatives to the Three Atoms That Directly Participate in the Breaking/Forming Bonds for the Reactants, Transition State Structures, and Products, along with the Potential Energy Barriers (kcal/mol) Corresponding to the H_{13A} Abstraction from AA by the Tyrosyl Radical for the Snapshots I and II^a

structure	$d(C-H)_R$	$d(H-O)_R$	$d(C-O)_R$	$d(C-H)_{TS}$	$d(H-O)_{TS}$	$d(C-O)_{TS}$	$d(C-H)_P$	$d(H-O)_P$	$d(C-O)_P$	ΔE^\ddagger
snapshot I	1.09	2.66	3.32	1.31	1.28	2.59	2.53	0.97	3.40	20.8
snapshot II	1.09	2.49	3.37	1.30	1.28	2.58	2.53	0.97	3.49	16.4

^aC, H, and O stand, respectively, for C_{13} , H_{13A} , and O of Tyrosyl radical.

3.2. Quantum Mechanics/Molecular Mechanics Calculations. **3.2.1. All-Radical Mechanism.** To start QM/MM calculations for the all-radical mechanism (see Scheme 2), we have selected two of the precatalytic snapshots obtained above by filtering the structures shown in Figure 3. In particular, the distances H_{13A} –OTyr385 and C_{13} –OTyr385 for snapshot I are 2.62 and 3.25 Å, respectively, and for snapshot II are 2.36 and 3.41 Å, also respectively. For each snapshot, we have first removed the phenolic hydrogen atom of Tyr385, and we have optimized the corresponding reactant structures. Because the first step of the all-radical mechanism is H_{13A} abstraction from AA by the tyrosyl radical, then we have built the potential energy profile along the corresponding reaction coordinate, in this case defined as the difference between the distances corresponding to the breaking bond (C_{13} – H_{13A}) and the forming bond (H_{13A} –OTyr385). The calculation of each profile has been repeated forward and backward until convergence to avoid hysteresis. The distances relative to the three atoms that directly participate in the breaking/forming bonds for the reactants, transition state structures, and products, along with the potential energy barriers are given in Table 1. As for these three atoms, once optimized, the reactants corresponding to the two snapshots exhibit some differences. This fact is normal when the substrate is as long and flexible as AA. In these cases, there exists a big dispersion^{49–52} of the pre-catalytic structures due to the huge number of rearrangements that, for instance, AA can adopt within the configurational space. This geometry dispersion at the reactants does not usually produce significant changes in the reaction mechanism (the main goal of this paper), but in the potential energy barriers. In fact, the evolution along the reaction path of the reactants in snapshots I and II practically matches. C_{13} and O heavy atoms approach each other up to the transition state structure to facilitate the hydrogen transfer and then recover their original distance at the product. The geometries of both transition state structures around the transferring H_{13A} are quite similar. In spite of that, the potential energy barriers differ by 4 kcal/mol. As in previously studied enzyme reactions,^{49–51} the dispersion in energy barriers is not due to different transition state structures, but to the reactants’ dispersion. Anyway, the values we have obtained are reasonable in comparison with recent measurements⁵³ of the rate constants for oxidation of AA by COX-2 at 30 °C ($k_{cat} = 16.7 \text{ s}^{-1}$, what, according to conventional transition state theory, corresponds to a phenomenological free energy barrier of 16 kcal/mol).

The optimized products of the first step are AA radicals delocalized over the C_{11} – C_{15} planar pentadienyl system. From here on we will describe the subsequent steps of the all-radical mechanism for the two parallel reaction paths derived from each snapshot, which have been studied in an identical manner. We will see that the main features of both reactions pathways are qualitatively identical, which reinforces the obtained

conclusions. To study the second step, addition of an oxygen molecule to C₁₁, we have chosen different possible starting positions of the oxygen molecule. Taking C₁₁ as the origin of coordinates, these molecules have been placed along the *x*, *y*, and *z* Cartesian axes and along the bisector axes contained in the *xy*, *xz*, and *yz* planes.⁵⁴ 9, 18, and 26 O₂ molecules have been set to a distance of 2.5, 3, and 3.5 Å, respectively, from the closest oxygen atom to C₁₁. In all, 53 initial positions of the oxygen molecule for each snapshot. Figure 5 displays the arrangement of the oxygen molecules at a distance of 3.5 Å from C₁₁.

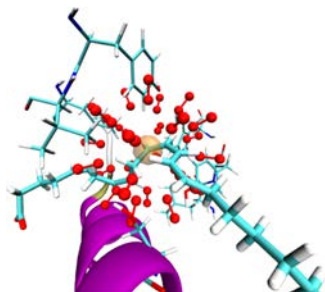


Figure 5. Arrangement of the oxygen molecules (in red) at a distance of 3.5 Å from C₁₁ (in orange).

QM/MM single point energy calculations have been carried out for the 53 positions and the higher energy structures have been discarded. The most stable structures have been optimized and taken as starting points to build the reaction path for the oxygen addition to C₁₁, with this distance chosen as the reaction coordinate. The potential energy barriers obtained for all the pathways that have been able to reach the products for both snapshots are given in Table 2.

Note that the attack of the oxygen molecule to C₁₁ could be antarafacial (i.e., by the face of the C₁₁–C₁₅ pentadienyl system opposite to the tyrosyl radical), leading to an 11R stereochemistry, or suprafacial (by the same side where the tyrosyl radical is placed), giving an 11S stereochemistry (see Figure S4 for a better view of the antarafacial/suprafacial concepts). The

Table 2. Potential Energy Barriers (kcal/mol) Corresponding to the Oxygen Addition to C₁₁ for all the Pathways That Have Been Able To Reach the Products for Snapshots I and II

snapshot I		snapshot II	
ΔE^\ddagger	O ₂ attack	ΔE^\ddagger	O ₂ attack
49.5	suprafacial	49.3	suprafacial
12.4	non ^a supra/antara	11.3	non ^a supra/antara
9.3	suprafacial	8.7	suprafacial
7.4	suprafacial	49.0	suprafacial
7.5	antarafacial	5.8	antarafacial
6.0	suprafacial	8.3	suprafacial
7.5	suprafacial	9.7	suprafacial
40.9	antarafacial		
35.8	non ^a supra/antara		
35.6	non ^a supra/antara		

^aThis oxygen attack can be classified neither as suprafacial nor as antarafacial.

two possibilities can be visualized in Figure 6. Note the antarafacial approach (Figure 6a) is the only one that is

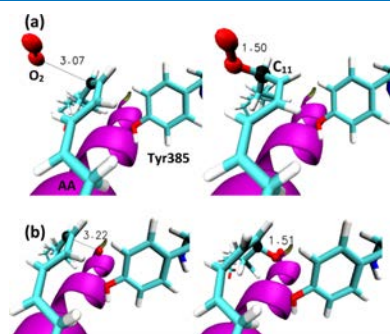


Figure 6. Optimized reactants (left) and products (right) corresponding to (a) antarafacial oxygen addition to C₁₁ for snapshot I and (b) suprafacial oxygen addition for snapshot II. The distances are given in Å. Carbon atom C₁₁ is depicted in black and oxygen atoms in red.

obtained experimentally when PGG₂ is the product. Our results show (the orientation of the O₂ attack has been indicated for each reaction path in Table 2) that both the antarafacial and the suprafacial attacks appear to be possible, existing reaction paths that involve relatively small energy barriers in comparison with other steps of the global mechanism. The lowest potential energy barriers correspond to the suprafacial attack for snapshot I (6.0 kcal/mol) and to the antarafacial attack for the snapshot II (5.8 kcal/mol). The reactants and products (peroxyl radicals) corresponding to an antarafacial addition for snapshot I and a suprafacial addition for snapshot II are pictured in Figure 6. Then, it seems that is not necessarily the oxygen addition step, the one that imposes the antarafacial final configuration of PGG₂ at C₁₁.

We have started from the products generated with the lowest potential energy barriers corresponding to the antarafacial addition and the suprafacial addition for both snapshots to follow the formation of the C₈-radical cyclic endoperoxides by means of a 9,11-cyclization. Prior to this third step, the just added oxygen molecule needs to rotate around the C₁₁–O bond the unbonded oxygen in order to face C₉. This rotation involves a small potential energy barrier of roughly 2 kcal/mol. From these optimized rotated structures, the potential energy barriers for this first cyclization (the reaction coordinate is the O–C₉ distance) are given in Table 3. The reactants and products corresponding to the formation of the endoperoxide in an antarafacial case for the snapshot I and in a suprafacial case for snapshot II are pictured in Figure 7. It can be seen that the cyclizations coming from the suprafacial (11S) O₂ additions are more favorable than the antarafacial

Table 3. Potential Energy Barriers (kcal/mol) for the First Cyclization Corresponding to Snapshots I and II

snapshot I		snapshot II	
ΔE^\ddagger	O ₂ attack	ΔE^\ddagger	O ₂ attack
15.0	suprafacial	10.0	suprafacial
19.5	antarafacial	20.0	antarafacial

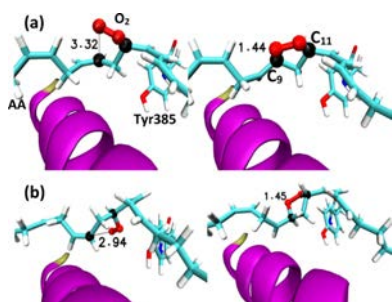


Figure 7. Optimized reactants (left) and products (right) for (a) antarafacial case (snapshot I) and (b) suprafacial case (snapshot II) for the first cyclization. The distances are given in Å. Carbon atoms C₉ and C₁₁ are depicted in black and oxygen atoms in red.

(11R) ones. Then, this third step cannot explain the natural 11R configuration of PGG₂ either.

Both snapshots behave in the same way for the 8,12-cyclization, the fourth step, for which the C₈–C₁₂ distance was chosen to define the reaction coordinate. The antarafacial intermediates form the new C₈–C₁₂ bond, leading to a ring of 5 carbon atoms and a C₁₃–C₁₅ allyl radical, with potential energy barriers of 26.5 and 24.1 kcal/mol for snapshots I and II, respectively. Conversely, the suprafacial intermediates are unable to produce this 8,12-cyclization. When the formation of the C₈–C₁₂ bond is forced by means of shortening the distance between both carbon atoms, the strain imposed to the molecule provokes its rupture, in such a way that the O–O and the C₁₁–C₁₂ bonds break, leading through a huge energy barrier (nearly 50 kcal/mol) to a broken structure that has nothing to do with the one that has to be the product of this fourth step. At this point, it has to be emphasized that the substrate AA is a very long (20 carbon atoms) and flexible molecule (as a consequence of its multiple single bonds), but at the same time its structure is quite rigid as well, due to its four C=C double bonds. This rigidity increases as AA is undergoing successive cyclizations. Therefore, a local chemical reaction at a given point of AA can require such conformational rearrangements, even in far regions of the substrate, that impose high energy barriers or even make the reaction impossible leading to the AA breakage. This is a very important factor that does not occur in enzymatic reactions involving small substrates, but that can be determinant when the substrate is as big as AA or other polyunsaturated fatty acids. In addition, we have to realize that the environment of residues that forms the enzyme active site restrains even more the conformational changes of AA and that this is the way how COX-2 manages to exert the catalytic control of the regioselectivity and stereoselectivity of the reaction. Taking into account all that, we can identify the 8,12-cyclization as the responsible for the fact that only the antarafacial molecular oxygen attack, but not the suprafacial one, in the second step leads to the final PGG₂, which, as a consequence, has an 11R configuration. This discriminating role of the 8,12-cyclization turns out to be likely the reason why Brash and cow.⁵⁵ conclude that it is impossible to perturb the stereochemistry of C₁₁ oxygenation in PGG₂ by mutagenesis experiments.

At this point, a careful analysis of the stereochemistry of the cyclopentane ring that has been formed after the 8,12-cyclization reveals that it presents a cis configuration (see

Figure 8a) for its side chains (the carboxylate end and the ω-end). That is, the hydrogen atoms bonded to C₈ and C₁₂

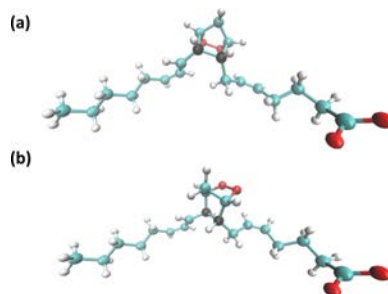


Figure 8. Prostaglandins containing (a) cis ring isomer or (b) trans ring isomer. Carbon atoms C₈ and C₁₂ are depicted in black and oxygen atoms in red.

appear on the same site of the cyclopentane. However, the natural prostaglandin produced by COX-2 contains the trans ring isomer. Very interestingly, as mentioned in the Introduction, the autoxidative cyclizations of lipid hydroperoxides in solution to form prostaglandin-like bicyclo endoperoxides through an all-radical mechanism mostly produce cis ring isomers, the trans ring isomers being highly disfavored.²⁰ Then, COX-2 in some way manages to catalytically force the formation of the biologically active trans ring isomer. At the first thought, it could be supposed that the geometries of both ring isomers are quite different. However, an overlay between both (see Figure 8) clearly shows that the differences are very subtle and do not lie in the carboxylate end nor the ω-end chains, but in the bicyclo endoperoxide, mainly in the position of the two oxygen atoms and carbon C₁₀.

Let us re-examine the 8,12-cyclization from the antarafacial C₈-radical cyclic endoperoxides. In Figure 9, we have shown the forward (red line) and backward (green line) potential energy profiles corresponding to the formation of the cis ring isomer of snapshot I. The red diamonds stand for the optimized stationary points of the cis reaction, which impose a potential energy barrier of 26.5 kcal/mol, as mentioned above. The upper insets contain pictures of the reactant (left, pre cis) and product (right, cis). When the backward profile was repeated (blue line) with a shorter optimization step size (0.1 Å vs 0.2 Å in the green line) it matches the previous cis one (green line) up to 3 Å of the C₈–C₁₂ reaction coordinate, but between the values 3.2–3.5 Å there appears an abrupt decrease of the energy barrier (roughly 10 kcal/mol) that accompanies a deformation of the bicyclo endoperoxide going from a pre cis structure to a pre trans one. Starting from the new structure of the reactant (pre trans), a forward energy profile (purple line) leads to the natural trans ring isomer. The purple diamonds stand for the optimized stationary points of the trans reaction, which now impose a potential energy barrier of 23.4 kcal/mol. The lower insets contain pictures of the reactant (left, pre trans) and product (right, trans). Moreover, the trans ring isomer turns out to be 24 kcal/mol more stable than the cis ring isomer. This way, it is clear that there are two possible reaction channels for the 8,12-cyclization in the active site of the enzyme, the cis and the trans channel. The geometric difference between them turns out to be extremely subtle, and

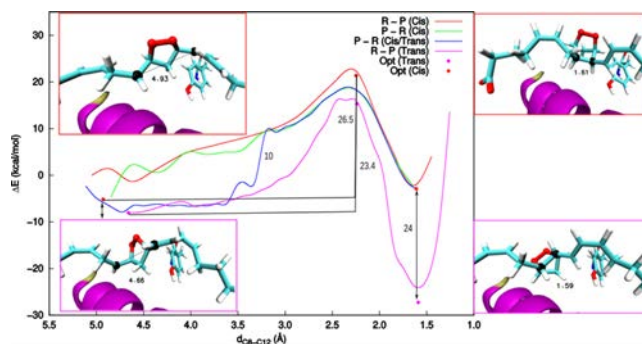


Figure 9. Forward (red line) and backward (green line) potential energy profiles corresponding to the formation of the cis ring isomer of snapshot I. The red diamonds stand for the optimized stationary points of the cis reaction. The upper insets contain pictures of the reactant (left, pre cis) and product (right, cis). The blue line is the backward profile with a shorter optimization step size. The purple line is a forward potential energy profile starting from the new structure of the reactant (pre trans) and leading to the natural trans ring isomer. The purple diamonds stand for the optimized stationary points of the trans reaction. The lower insets contain pictures of the reactant (left, pre trans) and product (right, trans). The distances are given in Å and the energies in kcal/mol. Carbon atoms C_8 and C_{12} are depicted in black and oxygen atoms in red.

the system can fall in either of the two channels depending on how the potential energy profile is built. In Figure S5, it is shown how a clockwise or an anticlockwise rotation of the endoperoxide group, which is accompanied by the corresponding motion of the cyclopentane ring, as going along the backward potential energy profile transforms the bicyclo endoperoxide from a pre cis structure to a pre trans one (green line to blue line) or not (the system holds on the green line), respectively, between the values 3.2–3.5 Å of the C_8 – C_{12} reaction coordinate. Thus, COX-2 controls the stereochemistry of the 8,12-cyclization by means of the spatial positions of the side chains of its active site residues, thus producing quite more stable trans ring isomers and with a faster rate than the corresponding cis ring isomers, in such a way that the natural PGG2 generated by COX-2 only contains the trans ring isomer of the bicyclo endoperoxide. Conversely, in solution, when that enzyme environment is absent, it is the cis ring isomer the one that is mostly produced. The same conclusion can be reached analyzing the behavior of snapshot II (Figure S6), where the potential energy barriers for the formation of the trans or cis ring isomer are, respectively, 17.5 or 24.1 kcal/mol, the first one 16.2 kcal/mol being more stable. Note that our results allow us to override one of the points argued by Dean and Dean¹⁰ in favor of their carbocation-based mechanism (see above).

The fifth step consists of the addition of O_2 to C_{15} . Starting from the optimized C_{13} – C_{15} allyl radical trans ring isomers obtained after the fourth step for snapshots I and II we have followed a strategy similar to the one adopted for the O_2 addition to C_{11} in the second step. The potential energy barriers obtained for all the pathways (with the O – C_{15} distance taken as the reaction coordinate) that have been able to reach the products (peroxyl radicals at C_{15}) for both snapshots are given in Table 4. Both the 15R and the 15S additions are possible for snapshot I, although only the 15S stereochemistry is reached in the case of snapshot II. In all cases, the potential energy barriers are relatively small.

The sixth and last step of the all-radical mechanism consists of the back hydrogen transfer from Tyr385 to the peroxyl radicals at C_{15} formed in the fifth step. We have taken the unbonded oxygen–H distance to define the reaction

Table 4. Potential Energy Barriers (kcal/mol) Corresponding to the Oxygen Addition to C_{15} for all the Pathways That Have Been Able To Reach the Products for Snapshots I and II

snapshot I		snapshot II	
ΔE^\ddagger	stereochemistry C_{15}	ΔE^\ddagger	stereochemistry C_{15}
2.6	R	2.4	S
6.8	S	2.5	S

coordinate. In the case of snapshot I, the peroxy group has to first rotate the unbonded oxygen in order to become close to the hydrogen atom of Tyr385 that will be abstracted. This rotation involves two small potential energy barriers (see Figure S7) preceding the energy rise corresponding to the hydrogen abstraction itself. We can observe in Table 5 that the

Table 5. Potential Energy Barriers (kcal/mol) Corresponding to the Back Hydrogen Transfer from Tyr385 to the Peroxyl Radical at C_{15}

snapshot I		snapshot II	
ΔE^\ddagger	stereochemistry C_{15}	ΔE^\ddagger	stereochemistry C_{15}
14.9	R	11.8	S
13.2	S	10.2	S

formation of the hydroperoxide group with stereochemistry 15S is favored versus the 15R one. The scenario corresponding to the snapshot II is slightly different. In this case, the peroxy group formed in the fifth step is already well oriented to abstract the hydrogen atom. No previous rotation is needed. As a consequence, the potential energy barriers (see Table 5) for the two pathways we have built (both of them leading to a 15S hydroperoxide) are smaller than in the case of snapshot I. Thus, the results corresponding to the last two steps show that the oxygen molecule can attack C_{15} forming either a 15S or a 15R hydroxyl radical, but the formation of the final 15S hydroperoxide is faster enough than the formation of the final 15R hydroperoxide to explain why only the 15S PGG2 is found experimentally.⁵⁵ Then, we have shown that the all-radical mechanism is able to account for the chirality at C_{15} , no

invocation to the carbocation-based mechanism being necessary.

3.2.2. Carbocation-Based Mechanism. As mentioned in the Introduction, a central point in this mechanism¹⁰ is the sigmatropic hydrogen transfer from C₁₀ to C₁₃, giving a delocalized C₈–C₁₂ pentadienyl radical. Starting from the optimized products after the H_{13A} abstraction from AA by the tyrosyl radical (see above), we have chosen the H₁₀–C₁₃ distance to determine the potential energy profiles for that hydrogen transfer. The potential energy barriers are 34.5 and 40.5 kcal/mol for the snapshots I and II, respectively. These very high barriers discard the carbocation-based mechanism. This process would transform an AA with a nonplanar C₈–C₁₂ fragment and a planar pentadienyl radical delocalized over C₁₁–C₁₅ to an AA with a planar pentadienyl radical delocalized over C₈–C₁₂ and a nonplanar C₁₁–C₁₅ fragment (the corresponding stationary points for snapshot I are pictured in Figure 10). This fact involves a considerable rearrangement

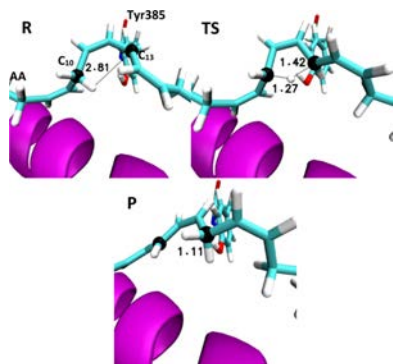


Figure 10. Stationary points corresponding to the sigmatropic hydrogen transfer from C₁₀ to C₁₃ according to the carbocation-based mechanism for snapshot I. R, TS, and P stand for the reactant, transition state structure, and product, respectively. The distances are given in Å. Carbon atoms C₁₀ and C₁₃ are depicted in black.

of AA that inside the active site of COX-2 causes those huge energy barriers. That hydrogen transfer could be feasible in a short hydrocarbon radical in solution, but this is not the case.

Thus, our results confirm the electron paramagnetic resonance experiments which do not detect a pentadienyl radical delocalized over C₈–C₁₂, but over C₁₁–C₁₅.^{22,56}

On the other hand, the experimental finding²¹ (see the Introduction) that with 10,10-difluoroarachidonic acid as substrate, COX enzymes do not generate any cyclic prostaglandin-like products, but acyclic alcohols such as 10,10-difluoro-11S-hydroxyeicosatetraenoic acid, seems to support the important role of C₁₀ (and, as a consequence, the feasibility of the carbocation based mechanism) for the formation of prostaglandins. Then, we have decided to check what predicts the all-radical mechanism for that substrate. To this aim, we have first substituted the two hydrogen atoms at C₁₀ by two fluorine atoms in the snapshots I and II of the AA radical delocalized over the C₁₁–C₁₅ planar pentadienyl system generated in the first reaction step (the H_{13A} abstraction). After optimization, we have followed a procedure similar to the one outlined above to select different possible starting positions of the oxygen molecule and proceed to add the oxygen molecule

to C₁₁. For snapshot II, we have found an antarafacial reaction path with a potential energy barrier of 40 kcal/mol but a suprafacial pathway with a barrier of 13.2 kcal/mol. The corresponding addition products are pictured in Figure 11.

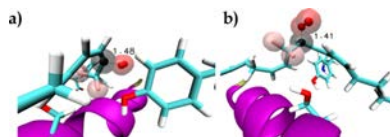


Figure 11. Optimized products of the (a) suprafacial and (b) antarafacial oxygen addition to C₁₁, of the 10,10-difluoroarachidonic acid radical delocalized over the C₁₁–C₁₅ planar pentadienyl system for snapshot II. The distances are given in Å. Carbon atom C₁₁ is depicted in black, oxygen atoms in red, and fluorine atoms in pink.

Note that the two fluorine atoms at C₁₀ are antarafacial with respect to the tyrosyl radical. Then, it can be easily understood that they highly prevent the antarafacial molecular oxygen attack, but not the suprafacial one. On the other hand, we have found two suprafacial additions for snapshot I, with barriers of 6.1 and 12.3 kcal/mol. As mentioned above, the suprafacial oxygen attack involves an 11S stereochemistry and is not able to produce PGG₂. As a consequence, we have demonstrated that the all-radical mechanism does explain why COX-2 converts the substrate 10,10-difluoroarachidonic acid just to the 10,10-difluoro-11S-hydroxyeicosatetraenoic acid, but not to PGG₂, no invocation to any special role of C₁₀ (nor to the carbocation based mechanism) being required.

4. CONCLUSIONS

COX-2 is one of the two main human enzymes responsible for inflammation and in this sense is an extremely important pharmacologic target of the nonsteroidal anti-inflammatory drugs. COX-2 transforms arachidonic acid, its main substrate, to the lipid pro-inflammatory mediators prostaglandins. In this paper, we have combined molecular dynamics simulations and QM/MM calculations to study the complete reaction mechanism corresponding to the formation of PGG₂ in the cyclooxygenase active site of COX-2. We have shown that COX-2 converts AA to PGG₂ by means of an all-radical catalytic mechanism^{16–19} that involves six successive reaction steps, including two hydrogen transfers, two O₂ additions, and two cyclizations. We have followed the evolution and fate of two pre-catalytic (i.e., ready to react) snapshots taken from the initial molecular dynamics simulation of the enzyme: substrate Michaelis complex. We have found that the main trends of the mechanism are the same for both, although each one retains its own quantitative values. That is, we can infer that, as usual in this kind of enzymatic reactions, there exists a significant dispersion of the initial geometry of the reactants, which produces some dispersion of the quantitative values for each step, but within a common mechanism. Indeed, the quantitative values (for instance, the energy barriers) measured experimentally for the macroscopic reaction come from a probability weighted average over all the possible reactants.

As seen in Figure 12, AA undergoes quite significant distortions in its way to form PGG₂. These distortions involve considerable conformational changes (especially from carbon atoms 8 to 15) that are not easy for such a long substrate, that is both flexible (due to its single bonds) and rigid (due to its four C=C double bond), and this rigidity increases as the

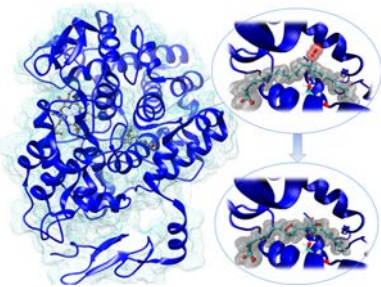


Figure 12. COX-2 showing the two active sites, the peroxidase active site (left) and the cyclooxygenase active site (right). The two elliptic inset corresponds to AA being attacked by an oxygen molecule at the beginning of the second step (up) and to PGG2 formed in the sixth step (down).

successive cyclizations occur. COX-2 uses its relatively narrow channel in the cyclooxygenase active site to restrain the available conformational changes of AA. This is the way how COX-2 manages to catalytically control the exquisite regioselectivity and stereoselectivity of the formation of PGG2, in particular its 11R and 15S final stereochemistry and its trans cyclopentane ring isomer (recall that the all-radical mechanism mostly produces the cis cyclopentane ring isomer in solution).

Conversely, the huge potential energy barriers we have found for the postulated hydrogen transfer between carbon atoms 10 and 13 are enough to discard the carbocation based mechanism.¹⁰ These high barriers are the consequence of the transformation of an AA with a nonplanar C₈–C₁₂ fragment and a planar pentadienyl radical delocalized over C₁₁–C₁₅ to an AA with a planar pentadienyl radical delocalized over C₈–C₁₂ and a nonplanar C₁₁–C₁₅ fragment, a considerable rearrangement of AA that inside the active site of COX-2 is not feasible. In addition, we have shown that the all-radical mechanism already predicts that COX-2 does not generate PGG2 but just the 10,10-difluoro-11S-hydroxyicosatetraenoic acid when 10,10-difluoroarachidonic acid is the substrate, this way decaying one of the main arguments in favor of the carbocation based mechanism.¹⁰

To summarize, we have shown that the formation of PGG2 from AA catalyzed by COX-2 takes place through the all-radical catalytic mechanism, and we have explained how this enzyme manages to control the regioselectivity and stereoselectivity of the reaction. We hope that this detailed molecular knowledge can be useful to understand how the nonsteroidal anti-inflammatory drugs act and to design other ones with fewer side effects.

■ ASSOCIATED CONTENT

Supporting Information

The Supporting Information is available free of charge on the ACS Publications website at DOI: 10.1021/acsomega.8b03575.

QM regions defined for the different steps studied in the all-radical mechanism, evolution of the distances H_{13A}–OTyr385 and C₁₃–OTyr385 along the 150 ns MD simulation of AA within the cyclooxygenase active site including Tyr385 of monomer B of COX-2, evolution of the distances H_{13A}–OTyr385 and C₁₃–OTyr385 along

the 100 ns MD simulation of AA within the cyclooxygenase active site including the Tyr385* radical of monomer B of COX-2, view of the antarafacial/suprafacial concepts, potential energy profiles corresponding to the formation of the cis ring isomer of snapshot I, potential energy profiles corresponding to the formation of the cis ring isomer of snapshot II, potential energy profiles corresponding to the back hydrogen transfer from Tyr385 to the peroxy radicals at C₁₅ formed in the fifth step of the all-radical mechanism, and atomic spin density information (PDF)

■ AUTHOR INFORMATION

Corresponding Author

*Email: JoseMaria.Lluch@uab.cat.

ORCID

Àngels González-Lafont: 0000-0003-0729-2483

José M. Lluch: 0000-0002-7536-1869

Notes

The authors declare no competing financial interest.

■ ACKNOWLEDGMENTS

We thank the Spanish “Ministerio de Ciencia, Innovación y Universidades” for Grant CTQ2017-83745-P. We acknowledge CSUC for computational facilities. We also thank Pedro Alexandrino Fernandes (Universidade do Porto) for helping us to parameterize the tyrosyl radical.

■ REFERENCES

- Vecchio, A. J.; Simmons, D. M.; Malkowski, M. G. Structural Basis of Fatty Acid Substrate Binding to Cyclooxygenase-2. *J. Biol. Chem.* **2010**, *285*, 22152–22163.
- Smith, W. L.; DeWitt, D. L.; Garavito, R. M. Cyclooxygenases: Structural, Cellular, and Molecular Biology. *Annu. Rev. Biochem.* **2000**, *69*, 145–182.
- Mitchell, J. A.; Akarasereenont, P.; Thiemermann, C.; Flower, R. J.; Vane, J. R. Selectivity of Nonsteroidal Antiinflammatory Drugs as Inhibitors of Constitutive and Inducible Cyclooxygenase. *Proc. Natl. Acad. Sci. U.S.A.* **1993**, *90*, 11693–11697.
- Tosco, P. A Mechanistic Hypothesis for the Aspirin-Induced Switch in Lipid Mediator Production by Cyclooxygenase-2. *J. Am. Chem. Soc.* **2013**, *135*, 10404–10410.
- Lei, J.; Zhou, Y.; Xie, D.; Zhang, Y. Mechanistic Insights into a Classic Wonder Drug–Aspirin. *J. Am. Chem. Soc.* **2014**, *137*, 70–73.
- Orlando, B. J.; Lucido, M. J.; Malkowski, M. G. The Structure of Ibuprofen Bound to Cyclooxygenase-2. *J. Struct. Biol.* **2015**, *189*, 62–66.
- Konkle, M. E.; Blobaum, A. L.; Moth, C. W.; Prusakiewicz, J. J.; Xu, S.; Ghebreselasie, K.; Akingbade, D.; Jacobs, A. T.; Rouzer, C. A.; Lybrand, T. P.; et al. Conservative Secondary Shell Substitution In Cyclooxygenase-2 Reduces Inhibition by Indomethacin Amides and Esters via Altered Enzyme Dynamics. *Biochemistry* **2015**, *55*, 348–359.
- Lucido, M. J.; Orlando, B. J.; Vecchio, A. J.; Malkowski, M. G. Crystal Structure of Aspirin-Acetylated Human Cyclooxygenase-2: Insight into the Formation of Products with Reversed Stereochemistry. *Biochemistry* **2016**, *55*, 1226–1238.
- Orlando, B. J.; Borbat, P. P.; Georgieva, E. R.; Freed, J. H.; Malkowski, M. G. Pulsed Dipolar Spectroscopy Reveals That Tyrosyl Radicals Are Generated in Both Monomers of the Cyclooxygenase-2 Dimer. *Biochemistry* **2015**, *54*, 7309–7312.
- Dean, A. M.; Dean, F. M. Carbocations in the Synthesis of Prostaglandins by the Cyclooxygenase of Pgh Synthase? *Protein Sci.* **1999**, *8*, 1087–1098.

- (11) Kiefer, J. R.; Pawlitz, J. L.; Moreland, K. T.; Stegeman, R. A.; Hood, W. F.; Gierse, J. K.; Stevens, A. M.; Goodwin, D. C.; Rowlinson, S. W.; Marnett, L. J.; et al. Structural Insights into the Stereochemistry of the Cyclooxygenase Reaction. *Nature* **2000**, *405*, 97–101.
- (12) Yuan, C.; Rieke, C. J.; Rimón, G.; Wingerd, B. A.; Smith, W. L. Partnering between Monomers of Cyclooxygenase-2 Homodimers. *Proc. Natl. Acad. Sci. U.S.A.* **2006**, *103*, 6142–6147.
- (13) Silva, P. J.; Fernandes, P. A.; Ramos, M. J. A Theoretical Study of Radical-Only and Combined Radical/Carbocationic Mechanisms of Arachidonic Acid Cyclooxygenation by Prostaglandin H Synthase. *Theor. Chem. Acc.* **2003**, *110*, 345–351.
- (14) Marnett, L. J. Cyclooxygenase Mechanisms. *Curr. Opin. Chem. Biol.* **2000**, *4*, 545–552.
- (15) Schneider, C.; Boeglin, W. E.; Lai, S.; Cha, J. K.; Brash, A. R. Synthesis and Applications of Stereospecifically-³H-Labeled Arachidonic Acids as Mechanistic Probes for Lipoxygenase and Cyclooxygenase Catalysis. *Anal. Biochem.* **2000**, *284*, 125–135.
- (16) Hamberg, M.; Samuelsson, B. On the Mechanism of the Biosynthesis of Prostaglandins E-1 and F-1-Alpha. *J. Biol. Chem.* **1967**, *242*, 5336–5343.
- (17) Marnett, L. J.; Maddipati, K. R. Prostaglandin H Synthase. In *Peroxidases in Chemistry and Biology*; Everse, J., Everse, K. E., Grisham, M. B., Eds.; CRC PRESS, 1991; Vol. 1, pp 293–334.
- (18) Smith, W. L.; Marnett, L. J. Prostaglandin Endoperoxide Synthase: Structure and Catalysis. *Biochim. Biophys. Acta, Lipids Lipid Metab.* **1991**, *1083*, 1–17.
- (19) Schneider, C.; Pratt, D. A.; Porter, N. A.; Brash, A. R. Control of Oxygenation in Lipoxygenase and Cyclooxygenase Catalysis. *Chem. Biol.* **2007**, *14*, 473–488.
- (20) O'Connor, D. E.; Mihelich, E. D.; Coleman, M. C. Stereochemical Course of the Autoxidative Cyclization of Lipid Hydroperoxides to Prostaglandin-like Bicyclo Endoperoxides. *J. Am. Chem. Soc.* **1984**, *106*, 3577–3584.
- (21) Kwok, P. Y.; Muellner, F. W.; Fried, J. Enzymatic Conversions of 10,10-Difluoroarachidonic Acid with PGH Synthase and Soybean Lipoxygenase. *J. Am. Chem. Soc.* **1987**, *109*, 3692–3698.
- (22) Navratil, A. R.; Shchepinov, M. S.; Dennis, E. A. Lipidomics Reveals Dramatic Physiological Kinetic Isotope Effects during the Enzymatic Oxygenation of Polyunsaturated Fatty Acids Ex Vivo. *J. Am. Chem. Soc.* **2017**, *140*, 235–243.
- (23) Maier, J. A.; Martinez, C.; Kasavajhala, K.; Wickstrom, L.; Hauser, K. E.; Simmerling, C. Ff14SB: Improving the Accuracy of Protein Side Chain and Backbone Parameters from Ff99SB. *J. Chem. Theory Comput.* **2015**, *11*, 3696–3713.
- (24) Case, Babin, V.; Berryman, J.; Betz, R.; Cai, Q.; Cerutti, D.; Cheatham, T.; Darden, T.; Duke, R.; Gohlke, H.; et al. *Amber 14-Reference Manual*. 2014.
- (25) Jorgensen, W. L.; Chandrasekhar, J.; Madura, J. D.; Impey, R. W.; Klein, M. L. Comparison of Simple Potential Functions for Simulating Liquid Water. *J. Chem. Phys.* **1983**, *79*, 926–935.
- (26) Klein, C. I.; Cieplak, P.; Cornell, W.; Kollman, P. A. A Well-Behaved Electrostatic Potential Based Method Using Charge Restraints for Deriving Atomic Charges: The RESP Model. 2002.
- (27) Shahrokh, K.; Orendt, A.; Yost, G. S.; Cheatham, T. E. Quantum Mechanically Derived AMBER-Compatible Heme Parameters for Various States of the Cytochrome P450 Catalytic Cycle. *J. Comput. Chem.* **2011**, *33*, 119–133.
- (28) Wang, J.; Wolf, R. M.; Caldwell, J. W.; Kollman, P. A.; Case, D. A. Development and Testing of a General Amber Force Field. *J. Comput. Chem.* **2004**, *25*, 1157–1174.
- (29) Lee, C.; Yang, W.; Parr, R. G. Development of the Colle-Salvetti Correlation-Energy Formula into a Functional of the Electron Density. *Phys. Rev. B* **1988**, *37* (2), 785–789, DOI: 10.1103/PhysRevB37.785.
- (30) Becke, A. D. Density-Functional Thermochemistry. III. The Role of Exact Exchange. *J. Chem. Phys.* **1993**, *98*, 5648–5652.
- (31) Hariharan, P. C.; Pople, J. A. The Influence of Polarization Functions on Molecular Orbital Hydrogenation Energies. *Theor. Chim. Acta.* **1973**, *28*, 213–222.
- (32) Francl, M. M.; Pietro, W. J.; Hehre, W. J.; Binkley, J. S.; Gordon, M. S.; DeFrees, D. J.; Pople, J. A. Self-Consistent Molecular Orbital Methods. XXIII. A Polarization-Type Basis Set for Second-Row Elements. *J. Chem. Phys.* **1982**, *77*, 3654–3665.
- (33) Frisch; Trucks, G.; Schlegel, H.; Scuseria, G.; Robb, M.; Cheeseman, J.; Scalmani, G.; Barone, V.; Mennucci, B.; Petersson, G.; et al. *Gaussian 09*; Gaussian, Inc.: Wallingford, CT, 2009.
- (34) Lei, H.; Baker, N. A.; Li, X. Data-Driven Parameterization of the Generalized Langevin Equation. *Proc. Natl. Acad. Sci. U.S.A.* **2016**, *113*, 14183–14188.
- (35) Berendsen, H. J. C.; Postma, J. P. M.; van Gunsteren, W. F.; DiNola, A.; Haak, J. R. Molecular Dynamics with Coupling to an External Bath. *J. Chem. Phys.* **1984**, *81*, 3684–3690.
- (36) Ryckaert, J.-P.; Cicotti, G.; Berendsen, H. J. C. Numerical Integration of the Cartesian Equations of Motion of a System with Constraints: Molecular Dynamics of n-Alkanes. *J. Comput. Phys.* **1977**, *23*, 327–341.
- (37) Deserno, M.; Holm, C. How to Mesh up Ewald Sums. I. a Theoretical and Numerical Comparison of Various Particle Mesh Routines. *J. Chem. Phys.* **1998**, *109*, 7678–7693.
- (38) Le Grand, S.; Götz, A. W.; Walker, R. C. SPFP: Speed without Compromise—A Mixed Precision Model for GPU Accelerated Molecular Dynamics Simulations. *Comput. Phys. Commun.* **2013**, *184*, 374–380.
- (39) Salomon-Ferrer, R.; Götz, A. W.; Poole, D.; Le Grand, S.; Walker, R. C. Routine Microsecond Molecular Dynamics Simulations with AMBER on GPUs. 2. Explicit Solvent Particle Mesh Ewald. *J. Chem. Theory Comput.* **2013**, *9*, 3878–3888.
- (40) Sherwood, P.; de Vries, A. H.; Guest, M. F.; Schreckenbach, G.; Catlow, C. R. A.; French, S. A.; Sokol, A. A.; Bromley, S. T.; Thiel, W.; Turner, A. J.; et al. QUASI: A General Purpose Implementation of the QM/MM Approach and Its Application to Problems in Catalysis. *J. Mol. Struct.: THEOCHEM* **2003**, *632*, 1–28.
- (41) Metz, S.; Kästner, J.; Sokol, A. A.; Keal, T. W.; Sherwood, P. ChemShell—a Modular Software Package for QM/MM Simulations. *Wiley Interdiscip. Rev.: Comput. Mol. Sci.* **2013**, *4*, 101–110.
- (42) Smith, W.; Forester, T. R. DL_POLY 2.0: A general-purpose parallel molecular dynamics simulation package. *J. Mol. Graphics* **1996**, *14*, 136–141.
- (43) Bakowies, D.; Thiel, W. Hybrid Models for Combined Quantum Mechanical and Molecular Mechanical Approaches. *J. Phys. Chem.* **1996**, *100*, 10580–10594.
- (44) Senn, H. M.; Thiel, W. QM/MM Methods for Biomolecular Systems. *Angew. Chem., Int. Ed.* **2009**, *48*, 1198–1229.
- (45) Liu, D. C.; Nocedal, J. On the Limited Memory BFGS Method for Large Scale Optimization. *Math. Program.* **1989**, *45*, 503–528.
- (46) Humphrey, W.; Dalke, A.; Schulten, K. VMD: Visual Molecular Dynamics. *J. Mol. Graphics* **1996**, *14*, 33–38.
- (47) Furse, K. E.; Pratt, D. A.; Schneider, C.; Brash, A. R.; Porter, N. A.; Lybrand, T. P. Molecular Dynamics Simulations of Arachidonic Acid-Derived Pentadienyl Radical Intermediate Complexes with COX-1 and COX-2: Insights into Oxygenation Regio- and Stereoselectivity. *Biochemistry* **2006**, *45*, 3206–3218.
- (48) Furse, K. E.; Pratt, D. A.; Porter, N. A.; Lybrand, T. P. Molecular Dynamics Simulations of Arachidonic Acid Complexes with COX-1 and COX-2: Insights into. *Biochemistry* **2006**, *45*, 3189–3205.
- (49) Saura, P.; Suardiaz, R.; Masgrau, L.; Lluch, J. M.; González-Lafont, A. Unraveling How Enzymes Can Use Bulky Residues to Drive Site-Selective c-h Activation: The Case of Mammalian Lipoxygenases Catalyzing Arachidonic Acid Oxidation. *ACS Catal.* **2014**, *4*, 4351–4363.
- (50) Adel, S.; Karst, F.; González-Lafont, A.; Pekárová, M.; Saura, P.; Masgrau, L.; Lluch, J. M.; Stehling, S.; Horn, T.; Kuhn, H.; et al. Evolutionary Alteration of ALOX15 Specificity Optimizes the

Biosynthesis of Antiinflammatory and Proresolving Lipoxins. *Proc. Natl. Acad. Sci. U.S.A.* **2016**, *113*, E4266–E4275.

(51) Saura, P.; Kaganer, I.; Heydeck, D.; Lluch, J. M.; Kühn, H.; González-Lafont, À. Mutagenesis of Sequence Determinants of Truncated Porcine ALOX15 Induces Changes in the Reaction Specificity by Altering the Catalytic Mechanism of Initial Hydrogen Abstraction. *Chem.—Eur. J.* **2017**, *24*, 962–973.

(52) Ribeiro, A. J. M.; Santos-Martins, D.; Russo, N.; Ramos, M. J.; Fernandes, P. A. Enzymatic Flexibility and Reaction Rate: A QM/MM Study of HIV-1 Protease. *ACS Catal.* **2015**, *5*, 5617–5626.

(53) Liu, Y.; Roth, J. P. A Revised Mechanism for Human Cyclooxygenase-2. *J. Biol. Chem.* **2015**, *291*, 948–958.

(54) Saura, P.; Suardiàz, R.; Masgrau, L.; González-Lafont, À.; Rosta, E.; Lluch, J. M. Understanding the Molecular Mechanism of the Ala-versus-Gly Concept Controlling the Product Specificity in Reactions Catalyzed by Lipoygenases: A Combined Molecular Dynamics and QM/MM Study of Coral 8R-Lipoygenase. *ACS Catal.* **2017**, *7*, 4854–4866.

(55) Schneider, C.; Boeglin, W. E.; Prusakiewicz, J. J.; Rowlinson, S. W.; Marnett, L. J.; Samel, N.; Brash, A. R. Control of Prostaglandin Stereochemistry at the 15-Carbon by Cyclooxygenases-1 and -2. *J. Biol. Chem.* **2001**, *277*, 478–485.

(56) Peng, S.; Okeley, N. M.; Tsai, A.-L.; Wu, G.; Kulmacz, R. J.; van der Donk, W. A. Synthesis of Isotopically Labeled Arachidonic Acids To Probe the Reaction Mechanism of Prostaglandin H Synthase. *J. Am. Chem. Soc.* **2002**, *124*, 10785–10796.

Supporting information

Unraveling the Molecular Details of the Complete Mechanism that Governs the Synthesis of Prostaglandin G2 Catalyzed by Cyclooxygenase-2

Anna Cebrián-Prats,[†] Àngels González-Lafont,^{†,‡} and José M. Lluch^{†, ‡, *}

[†]Departament de Química and [‡]Institut de Biotecnologia i de Biomedicina (IBB), Universitat Autònoma de Barcelona, 08193 Bellaterra, Barcelona, Spain

Email: JoseMaria.Lluch@uab.cat

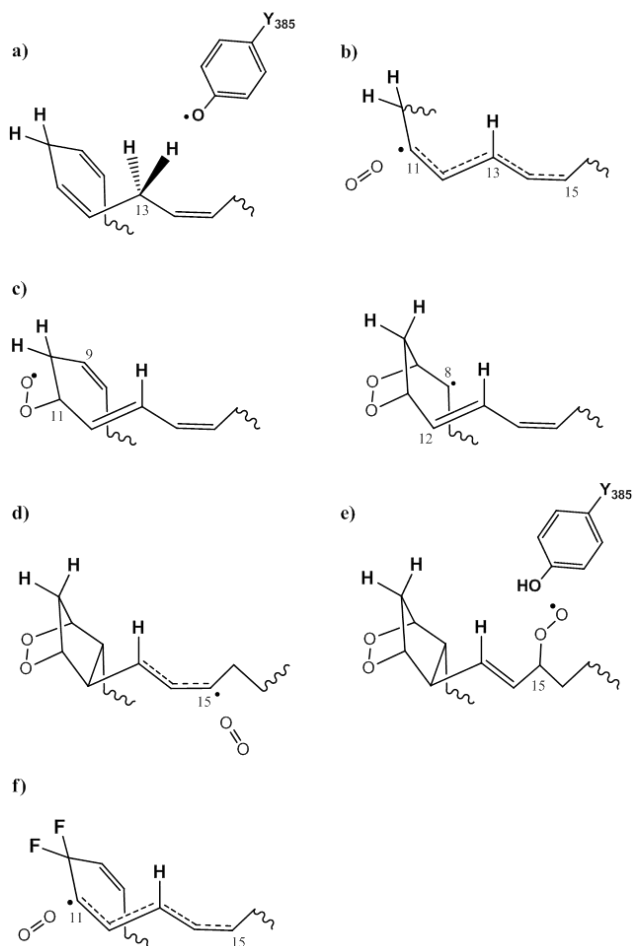


Figure S1. QM regions defined for the different steps studied in the all-radical mechanism: a) 38 atoms (link atoms not included) for the C₁₃ hydrogen abstraction (first step); b) 18 atoms for the O₂ addition at C₁₁ (second step); c) 25 atoms for the 9-11 (third step) and the 8-12 (fourth step) cyclizations; d) 30 atoms for the O₂ addition to C₁₅ (fifth step); e) 45 atoms for the back hydrogen transfer (sixth step); and f) 25 atoms for the O₂ addition at C₁₁ in the case of the 10,10-difluoroarachidonic acid as substrate. Link atoms are represented by wavy lines.

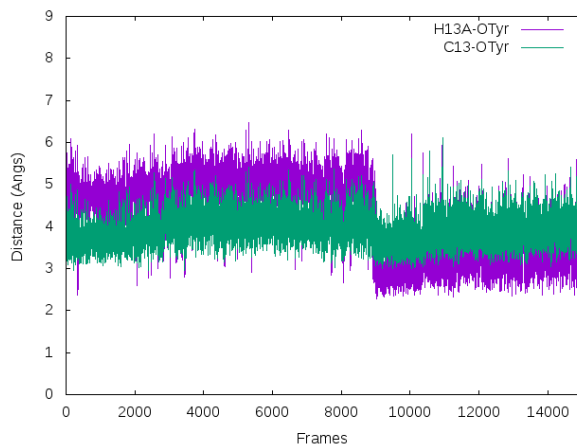


Figure S2. Evolution of the distances H_{13A} - OTyr385 (purple line) and C_{13} - OTyr385 (green line) along the 150 ns MD simulation of AA within the cyclooxygenase active site including Tyr385 of monomer B of COX-2. A frame has been taken each 10 ps.

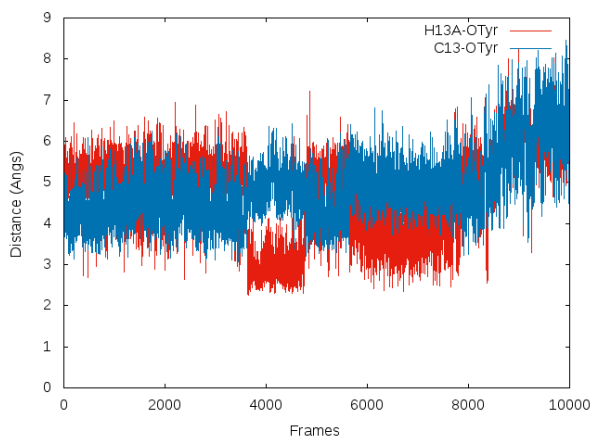


Figure S3. Evolution of the distances H_{13A} - OTyr385 (red line) and C_{13} - OTyr385 (blue line) along the 100 ns MD simulation of AA within the cyclooxygenase active site including the Tyr385 radical of monomer B of COX-2. A frame has been taken each 10 ps.

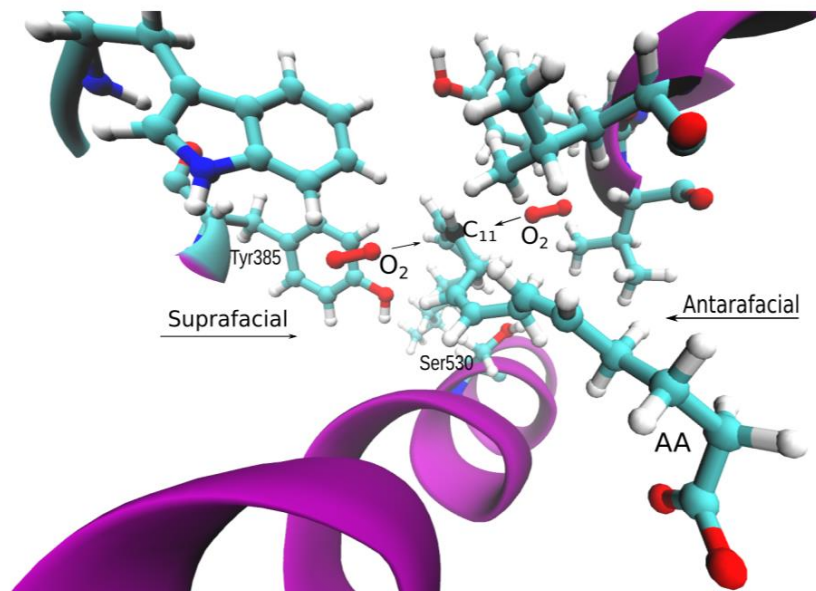


Figure S4. Comparative view between the suprafacial and the antarafacial O₂ attack to C₁₁. Carbon atom C₁₁ is depicted in black and oxygen atoms in red.

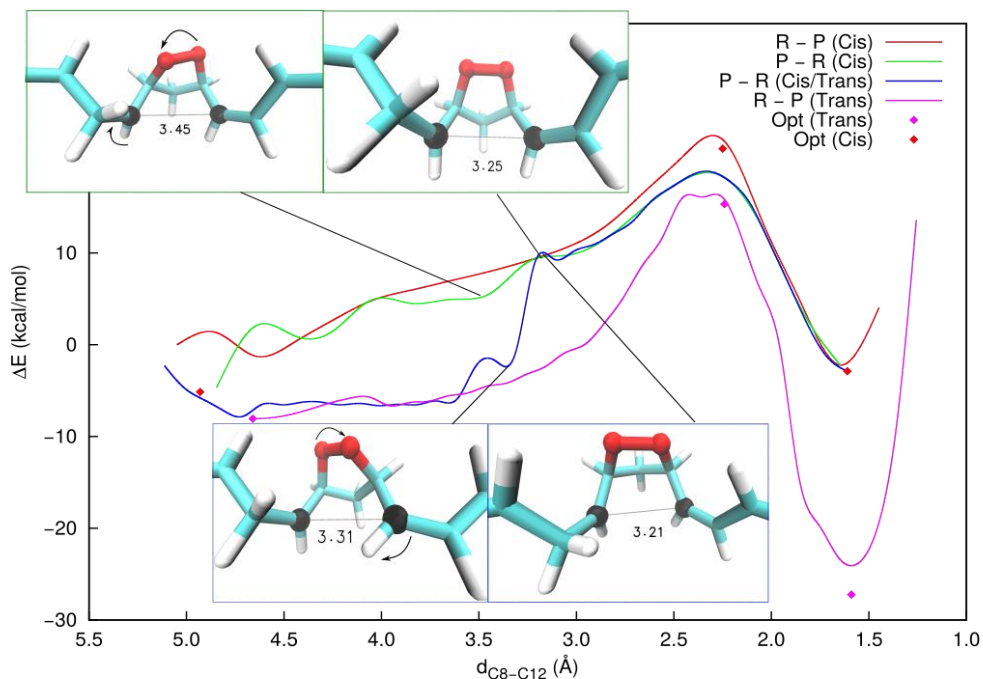


Figure S5. Forward (red line) and backward (green line) potential energy profiles corresponding to the formation of the *cis* ring isomer of snapshot I. The red diamonds stand for the optimized stationary points of the *cis* reaction. The upper insets show how the pre *cis* structure of the reactant is reached by means of an antidockwise rotation of the endoperoxide group. The blue line is the backward profile with a shorter optimization step size. The purple line is a forward potential energy profile starting from the new structure of the reactant (pre *trans*) leading to the natural *trans* ring isomer. The purple diamonds stand for the optimized stationary points of the *trans* reaction. The lower insets show how the pre *trans* structure of the reactant is reached by means of a clockwise rotation of the endoperoxide group. The distances are given in Å and the energies in kcal/mol. Carbon atoms C₈ and C₁₂ are depicted in black and oxygen atoms in red.

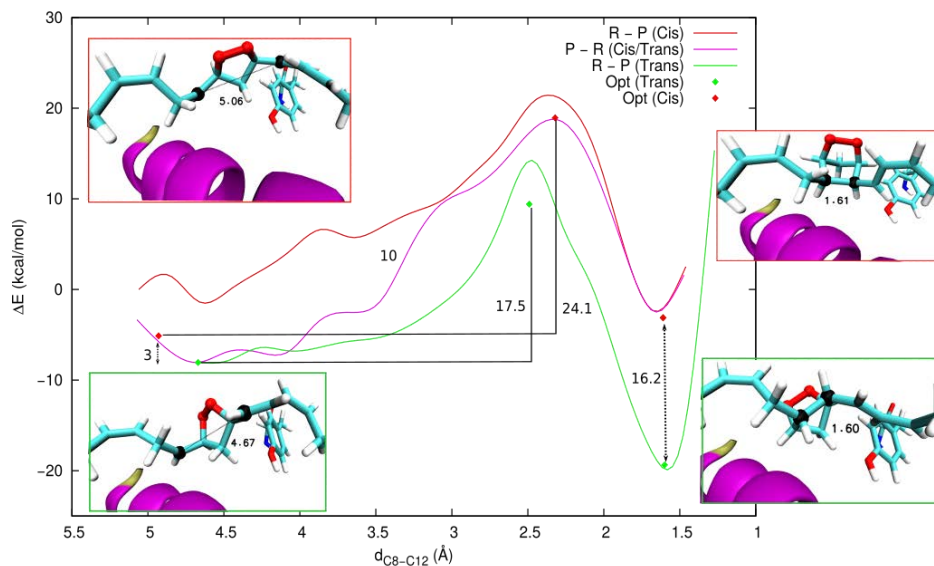
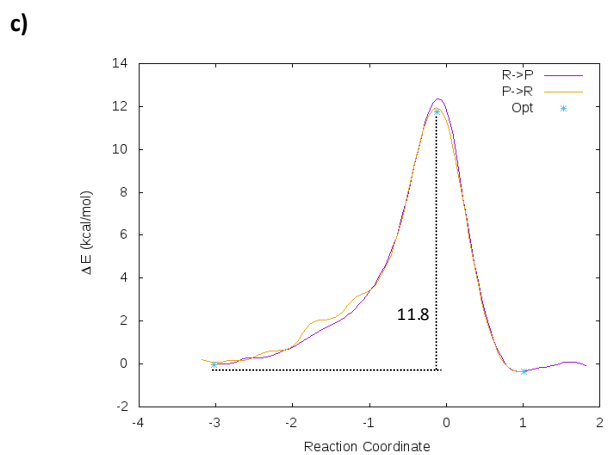
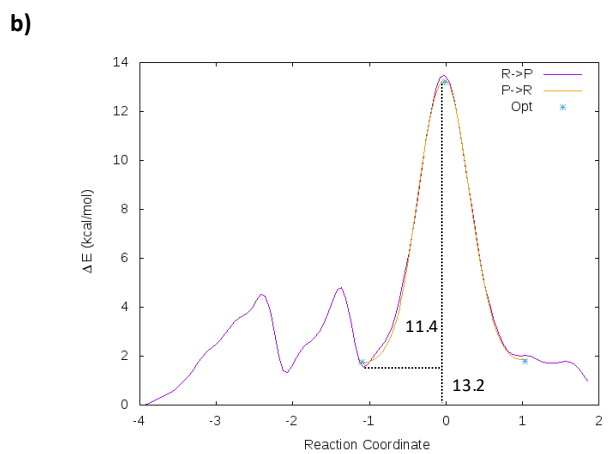
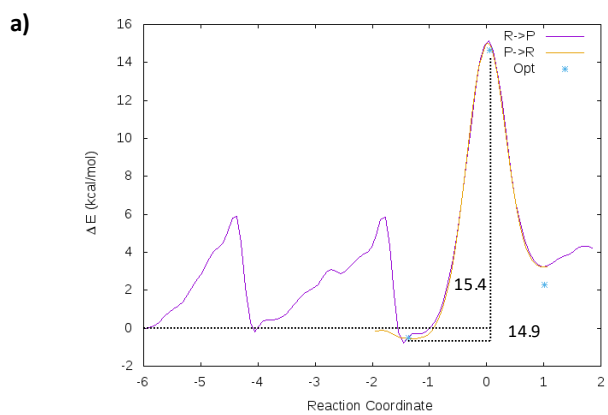


Figure S6. Forward (red line) potential energy profile corresponding to the formation of the *cis* ring isomer of snapshot II. The red diamonds stand for the optimized stationary points of the *cis* reaction. The upper insets contain pictures of the reactant (left, pre *cis*) and product (right, *cis*). The purple line is the backward profile with a shorter optimization step size. The green line is a forward potential energy profile starting from the new structure of the reactant (pre *trans*) and leading to the natural *trans* ring isomer. The green diamonds stand for the optimized stationary points of the *trans* reaction. The lower insets contain pictures of the reactant (left, pre *trans*) and product (right, *trans*). The distances are given in Å and the energies in kcal/mol. Carbon atoms C_8 and C_{12} are depicted in black and oxygen atoms in red.



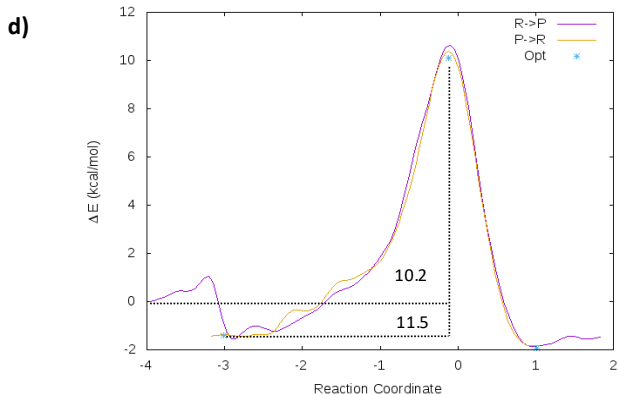


Figure S7. Potential energy profiles corresponding to the back hydrogen transfer (sixth step) from Tyr385 to the peroxy radicals at C₁₅ formed in the fifth step of the all-radical mechanism. a) Formation of a 15R hydroperoxide in snapshot I; b) Formation of a 15S hydroperoxide in snapshot I; c) Formation of a 15S hydroperoxide in snapshot II; and d) Formation of another 15S hydroperoxide in snapshot II. The reaction coordinate (in Å) is the difference between the distance corresponding to the breaking bond (HTyr385 – OTyr385) and the forming bond (HTyr385 – ·O (O₂)). The small barriers of the snapshot I represent the reorientation of the O₂ (a, b). The product obtained is the PGG₂. In the graphics the forward potential energy profiles are represented with purple lines, the backward ones with yellow lines, and the optimized stationary points with blue asterisks.

Table S1: Atomic spin densities (a.u.) (expressed as the excess of α spin) on the heavy atoms for one of the O₂ additions studied when O₂ is still far from the carbon atom (C₁₁).

Heavy atoms (QM region)	Spin Density
O _A	0.988
O _B	0.974
C ₁₀	0.024
C ₁₁	-0.365
C ₁₂	0.199
C ₁₃	-0.576
C ₁₄	0.230
C ₁₅	-0.486
C ₁₆	0.038

Article II


 Cite this: *RSC Adv.*, 2020, 10, 986

Unraveling how the Gly526Ser mutation arrests prostaglandin formation from arachidonic acid catalyzed by cyclooxygenase-2: a combined molecular dynamics and QM/MM study†

 Adrián Suñer-Rubio,^{ib a} Anna Cebrián-Prats,^{ib a} Àngels González-Lafont^{ib ab} and José M. Lluch^{ib *ab}

Cyclooxygenases (COXs) are the enzymes responsible for the biosynthesis of prostaglandins, eicosanoids that play a major role in many physiological processes. Particularly, prostaglandins are known to trigger inflammation, and COX-2, the enzyme isoform associated with this inflammatory response, catalyzes the cyclooxidation of arachidonic acid, leading to prostaglandin G₂. For this reason, COX-2 has been a very important pharmacological target for several decades now. The catalytic mechanism of COX-2, a so-called all-radical mechanism, consists of six chemical steps. One of the most intriguing aspects of this mechanism is how COX-2 manages to control the regio- and stereospecificity of the products formed at each step. Mutagenesis experiments have previously been performed in an attempt to find those hot-spot residues that make such control possible. In this context, it is worth mentioning that in experiments with the Gly526Ser COX-2 mutant, prostaglandins were not detected. In this paper, we have combined molecular dynamics simulations and quantum mechanics/molecular mechanics calculations to analyze how the COX-2 catalytic mechanism is modified in the Gly526Ser mutant. Therefore, this study provides new insights into the COX-2 catalytic function.

 Received 28th October 2019
 Accepted 12th December 2019

DOI: 10.1039/c9ra08860a

rsc.li/rsc-advances

1 Introduction

Lipid mediators¹ are bioactive lipids involved in many physiological processes, and are generated through specific biosynthetic pathways. They bind to their corresponding G protein-coupled receptors and transmit signals to target cells. The synthesis of many lipid mediators begins with the oxygenation of polyunsaturated fatty acids by some enzymes.² One of the most well known and important cases is the dioxygenation of arachidonic acid (AA, 20:4 n-6) by the enzyme cyclooxygenase-2

(COX-2), which leads to the formation of the eicosanoid prostaglandins. Prostaglandins control many pathological events, such as inflammation, fever, pain, cardiovascular diseases, and cancer.¹

AA is released from membrane glycerophospholipids. COX-2 is a membrane-associated homodimeric bifunctional hemoprotein.³ Only one monomer acts as a catalyst at a given time.⁴ The determination of the corresponding crystal structure³ has shown that in the murine cyclooxygenase active site of the catalytic monomer the AA carboxylate lies near the side chains

^aDepartament de Química, Universitat Autònoma de Barcelona, 08193 Bellaterra, Barcelona, Spain. E-mail: JoseMaria.Lluch@uab.cat

^bInstitut de Biotecnologia i de Biomedicina (IBB), Universitat Autònoma de Barcelona, 08193 Bellaterra, Barcelona, Spain

† Electronic supplementary information (ESI) available: The QM region of each particular reaction step; evolution of the C₁₃ pro-S hydrogen–O(Tyr385) distance during 100 ns of the first MD simulation of the Michaelis complex Gly526Ser COX-2/AA; evolution of the C₁₃–O(Tyr385) distance during 100 ns of the first MD simulation of the Michaelis complex Gly526Ser COX-2/AA; distance between the hydrogen of the Ser526 OH group and the oxygen atom of the backbone of Met522 during 10 ns (equilibration) + 20 ns (production) MD simulation of the Gly526Ser COX-2 mutated enzyme without AA; comparison between the structure corresponding to snapshot 1 extracted from the MD simulation of the COX-2/AA Michaelis complex and the centroid snapshot of the most populated cluster of the last MD simulation of the Gly526Ser COX-2/AA Michaelis complex; comparison between the centroid of the most

populated clusters; evolution of the C₁₃ pro-S hydrogen–O(Tyr385) and C₁₃–O(Tyr385) distances during 250 ns of the last MD simulation of the Gly526Ser COX-2/AA Michaelis complex; evolution of the C₁₃ pro-S hydrogen–O(Tyr385) and C₁₃–O(Tyr385) distances during a new 100 ns MD simulation of the Gly526Ser COX-2/AA Michaelis complex; distances between side chain carbon atoms of selected residues of snapshot 1 extracted from the MD simulation of the COX-2/AA Michaelis complex or the centroid snapshot of the most populated cluster of the last MD simulation of the Gly526Ser COX-2/AA Michaelis complex, and arachidonic acid bound in the corresponding active site active site; distances corresponding to the three atoms that directly participate in the breaking/forming of bonds for the reactant, transition state structure and product corresponding to the C₁₃ pro-S hydrogen abstraction by the tyrosyl radical; evolution of the key distances during C₁₃ pro-S hydrogen abstraction by the tyrosyl radical; structure obtained after the 8,12-cyclization to give a bicyclo endoperoxide which occurs in wild-type COX-2. See DOI: 10.1039/c9ra08860a



of Arg120 and Tyr355, whereas the ω -end is positioned in the hydrophobic groove above Ser530, exhibiting an "L-shaped" binding conformation. A tyrosyl radical is generated as a consequence of one-electron transfer from Tyr385 to the oxyferryl protoporphyrin IX radical cation formed in the peroxidase active site after activation by an alkyl hydroperoxide of its heme group. The C₁₃ carbon atom of AA is positioned 2.95 Å below the phenolic oxygen of Tyr385. The nascent tyrosyl radical starts the cyclooxygenase reaction by abstraction of the C₁₃ pro-S hydrogen atom when AA occupies the cyclooxygenase active site.^{5,6} Afterwards, addition of two oxygen molecules converts AA to prostaglandin G₂ (PGG₂). Later, PGG₂ is released to the peroxidase active site, where its 15-hydroperoxyl group is reduced to give prostaglandin H₂ (PGH₂).

The biosynthesis of PGG₂ in the cyclooxygenase active site is achieved by a six-step all-radical mechanism^{2,7–13} (see Scheme 1) derived from proposals by Hamberg and Samuelsson. It successively consists of: a C₁₃ pro-S hydrogen abstraction from AA by the tyrosyl radical 385, forming a planar delocalized C₁₁–C₁₅ pentadienyl radical (step 1); an antarafacial molecular oxygen addition at C₁₁ to give an 11R peroxy radical (step 2); a 9,11-cyclization leading to a C₈-radical cyclic endoperoxide (step 3); an 8,12-cyclization yielding a bicyclo endoperoxide and a C₁₃–C₁₅ allyl radical (step 4); a second antarafacial molecular oxygen addition at the 15S position (step 5); and a final back transfer of hydrogen from Tyr385 to the peroxy radical at C₁₅ (step 6), leading to the formation of PGG₂.

One of the most amazing features of the six-step all-radical mechanism is the extremely efficient way how COX-2 manages to control the stereochemistry and regiochemistry of the reactions it catalyzes. AA is a very long substrate (it contains 20 carbon

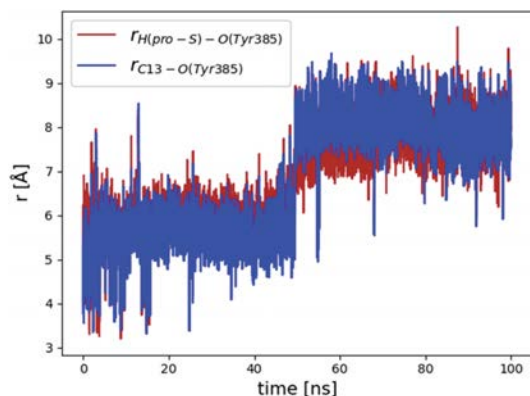
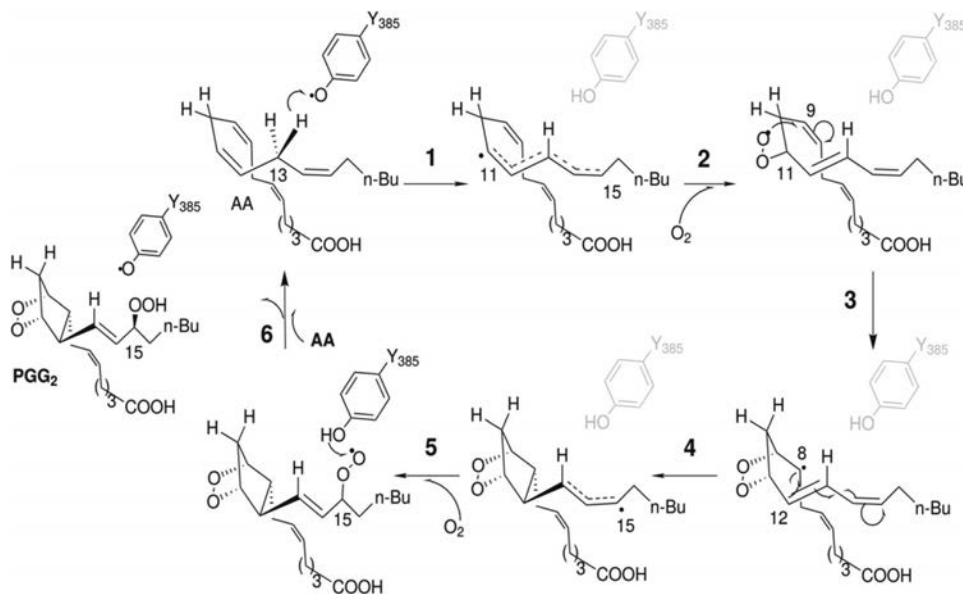


Fig. 1 Evolution of the C₁₃ pro-S hydrogen–O(Tyr385) (red line) and C₁₃–O(Tyr385) (blue line) distances over 100 ns of the first MD simulation of the Gly526Ser COX-2/AA Michaelis complex.

atoms). It is simultaneously a flexible molecule (owing to its multiple single bonds) and a rigid molecule (owing to its four C=C double bonds). The role of many active site residues of COX-2 is to make this control possible. A number of mutagenesis experiments have been performed to better understand the way they act.^{14–16} Particularly interesting is the case of the Gly526Ser mutant human COX-2.¹⁶ This mutation does not appear to interfere with the first three reaction steps. However, no formation of prostaglandins was detected, 11R-hydroperoxyicosatetraenoic acid (11R-HPETE) becoming the main product. Brash and co-workers¹⁶ proposed that the 8,12-cyclization in the Gly526Ser



Scheme 1 The all-radical mechanism for the formation of PGG₂ from arachidonic acid catalyzed by wild-type COX-2.



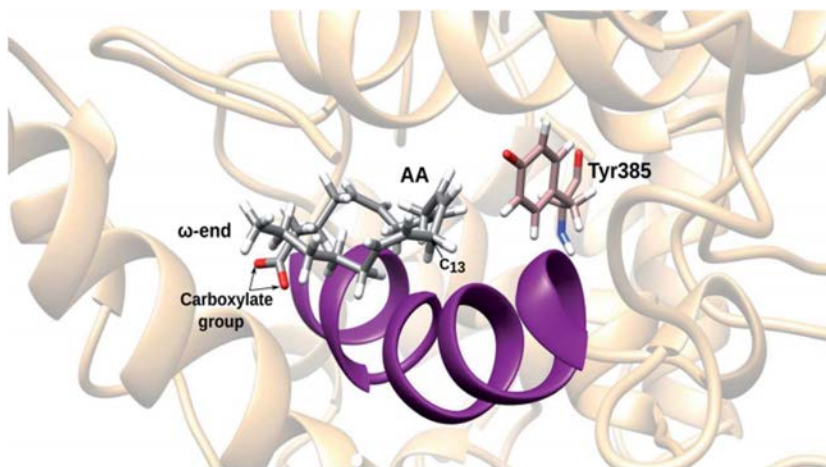


Fig. 2 A typical structure corresponding to the second half of the first MD simulation of the Gly526Ser COX-2/AA Michaelis complex.

mutant is sterically hindered by misalignment of the substrate carbon chains. So, instead of prostaglandins they found novel products, which were identified as 8,9-11,12-diepoxy-13*R*- (or 15*R*)-hydroperoxy derivatives of arachidonic acid.

The aim of this paper is to provide a detailed molecular view of the way how an apparently little significant mutation is able to fully arrest the PGG₂ biosynthesis, instead yielding diepoxy products. Thus, we have combined molecular dynamics (MD) simulations with quantum mechanics/molecular mechanics (QM/MM) calculations to analyze how the Gly526Ser mutant of COX-2 alters the six-step all-radical mechanism shown in Scheme 1 that holds for wild-type COX-2, so contributing to the understanding of the very important catalytic function of COX-2.

2 Computational methods

2.1 System setup

In a previous paper we studied¹³ the mechanism that governs the biosynthesis of PGG₂ catalyzed by wild-type COX-2. That system was built from the murine COX-2/AA complex (PDB code 3HS5)³, replacing the Co³⁺ complexed to the protoporphyrin IX group by Fe³⁺. The heme prosthetic group was tethered to the axial histidine (His388). Only the monomer B (the one where AA adopts an “L-shaped” productive binding configuration, with the C₁₃ carbon atom of AA near Tyr385) was modeled in the cyclooxygenase active site. After a 100 ns MD simulation a pair of snapshots was selected, and we showed that both were able to follow the all-radical mechanism displayed in Scheme 1, eventually yielding PGG₂. In this paper, we have taken one of those snapshots (snapshot 1), and we have replaced the Gly526 residue by a serine using the CHIMERA¹⁷ program. All the amino acid residues of the protein but His388 and Tyr385 were described using the AMBER ff14SB force field.¹⁸ All water molecules were deleted and the system was solvated again by means of the AMBER18¹⁹ tleap program. A pH of 7 was assumed for the titratable residues. Five Na⁺ ions were added at

the protein surface to neutralize the total charge of the system. An almost cubic box (100.2 Å × 113.4 Å × 92.5 Å) of TIP3P water molecules²⁰ was constructed, with a minimum cutoff distance of 15 Å between the atoms of the enzyme and the edge of the periodic box. All the water molecules closer than 2.2 Å to any atom of the enzyme or AA were removed. In all, the system contained about 80 000 atoms.

2.2 Parameterization

First of all, the parameters of the heme group were taken from a recent study.²¹ However, the corresponding partial charges of the ferric penta-coordinated high spin group (Fe³⁺) were calculated using the Restrained Electrostatic Potential (RESP)²² method at the HF/6-31G(d,p) level of theory. In addition, the

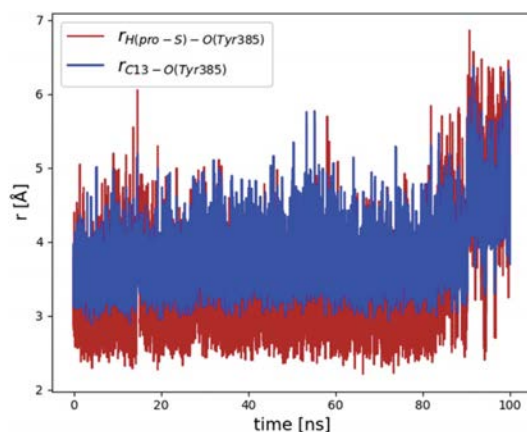


Fig. 3 Evolution of the C₁₃ pro-S hydrogen–O(Tyr385) (red line) and C₁₃–O(Tyr385) (blue line) distances over 100 ns of the last MD simulation of the Gly526Ser COX-2/AA Michaelis complex.



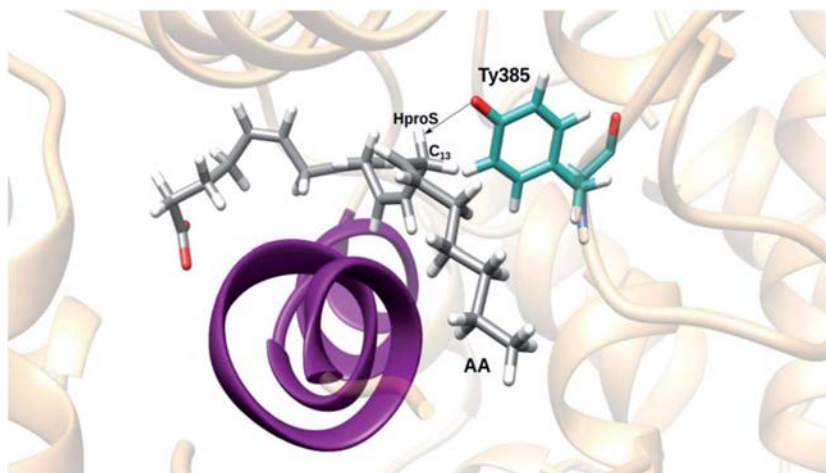


Fig. 4 A centroid snapshot of the most populated cluster, chosen as a snapshot representative of the ensemble of structures generated during the last MD simulation of the Gly526Ser COX-2/AA Michaelis complex.

parameters of the histidine coordinated to the metal were described by the general AMBER force field (GAFF)²³ using the residuegen and parmchk modules of AMBER14.²⁴ Secondly, the AA substrate, the delocalized C₁₁–C₁₅ pentadienyl radical of AA, and its delocalized C₁₃–C₁₅ allyl radical parameters were also taken from a recent study.²⁵ Finally, the parameterization of the tyrosyl radical was performed by calculating first the optimized structure of this residue using the B3LYP functional^{26,27} and the 6-31G(d,p)^{28,29} basis set for all atoms, followed by an RESP calculation of the partial atomic charges at the same level of theory using Gaussian09.³⁰ At this point, as the residue is not a standard tyrosine, the parameters of its bonds, angles, dihedrals and van der Waals terms should be re-calculated. Therefore, the force constants associated with each bond and angle were fitted using a harmonic function to reproduce the B3LYP/6-31G(d,p) potential energy profiles generated for the corresponding stretching and bending vibrations. The dihedral parameters were not calculated as they do not present significant differences with the standard tyrosine residue. The van der Waals parameters were taken from the GAFF force field of AMBER14, assigning the oxygen radical as an ether or ester oxygen.

2.3 Molecular dynamics simulations

Starting from the structure resulting from the setup, we carried out three successive molecular dynamics simulations using the same protocol before the production stage. For the first MD simulation the monomer B of Gly526Ser COX-2, with AA and the radical Tyr385 within the cyclooxygenase active site, was optimized following three successive molecular mechanics (MM) minimizations using the steepest descent and conjugate gradient methods. This was done to relax the system. Firstly, we applied harmonic restraints on the enzyme, the heme prosthetic group and AA, keeping the solvation water molecules free.

In the second minimization, only the heme prosthetic group and His388 were restrained. In the last minimization only the protein side chains were restrained, the rest of the system remaining free. Then, we carried out the MD simulation employing periodic boundary conditions (PBCs), with a cutoff of 10 Å for all Lennard-Jones and electrostatic interactions and the particle-mesh Ewald method³¹ to treat long-range electrostatic effects. The system was gradually heated from 0 to 300 K, with an increment of 30 K, during 10 steps of 20 ps each, imposing a harmonic restraint (5 kcal mol⁻¹ Å⁻²) to the heme prosthetic group, under the canonic (*NVT*) ensemble using Langevin dynamics.³² Next, a simulation was performed under the isothermic–isobaric (*NPT*) ensemble to ensure that the box

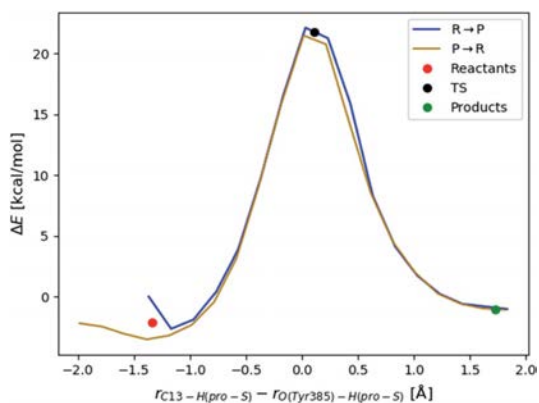


Fig. 5 Forward (blue line) and backward (ochre line) potential energy profiles corresponding to C₁₃ pro-S hydrogen abstraction by the tyrosyl radical. The circles indicate the locations of the stationary points.



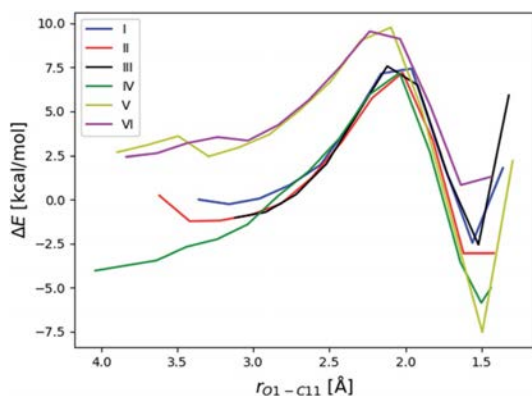


Fig. 6 Potential energy profiles corresponding to the addition of the oxygen molecule to C_{11} . The first point of reaction path I sets the origin of potential energies. O1 stands for the oxygen atom of the oxygen molecule that is closest to C_{11} .

did not deform, and to achieve an adequate density. Thus, once at 300 K, we carried out four steps of 10 ps each, at 1 atm pressure, with a weak restraint on the residue side chains, using an isotropic weak-coupling algorithm and the Berendsen barostat,³³ and then one more step of 160 ps with the same restraint up to a density of around 1 g cm^{-3} . Finally, an equilibration stage of 10 ns followed by a production period of 100 ns were calculated at 300 K under the NVT ensemble without any restraints apart from employing the SHAKE algorithm³⁴ to constrain all the covalent bonds containing hydrogen.

The other two MD simulations will be explained below. All the MD simulations were performed using the AMBER18 GPU (CUDA) version of the PMEMD package.^{35,36}

2.4 QM/MM calculations

We used quantum mechanics/molecular mechanics (QM/MM) calculations for the energy optimization of the structures. Each QM/MM system consisted of nearly 10 500 atoms, including all the residues of the monomer B of Gly526Ser COX-2 (with the radical Tyr385), the complete AA, and the 500 water molecules closest to C_{10} of AA. The active region, where all atoms moved freely during the optimization processes, involved around 2100 atoms whereas the rest of the system was kept

frozen. This region was defined by all residues and water molecules within a 15 \AA radius sphere centering on C_{10} , including the complete AA and the heme prosthetic group.

The QM/MM calculations were carried out with the modular package ChemShell,^{37,38} using Gaussian09 for the density functional theory (DFT) calculations of the quantum mechanics (QM) part. The calculations of the MM part were carried out with the DL_POLY module³⁹ in Chemshell, employing the AMBER force field.¹⁸ The QM region (being the Fe atom in the MM part because it did not belong to the cyclooxygenase active site) was described by the B3LYP functional with the 6-31G(d,p) basis set for all atoms, with a zero total charge and doublet multiplicity in all reaction steps. This QM region presented different sizes depending on the particular step studied in the catalytic mechanism (see Fig. S1†). The polarizing effect of the enzyme over the QM part was included by the electrostatic embedding scheme,⁴⁰ and the QM/MM boundary was treated using hydrogen link atoms with the charge-shift model.⁴¹ Finally, no cutoffs were introduced for the nonbonding MM and QM/MM interactions.

To determine the potential energy profiles, a series of optimizations were carried out imposing harmonic restraints on the reaction coordinate, with an increment of 0.2 \AA at each step. The energy minimizations were done with the limited-memory Broyden–Fletcher–Goldfarb–Shanno (L-BFGS) algorithm.⁴² A combination of the partitioned rational function optimizer (P-RFO)³⁹ and the L-BFGS methods was used to locate transition state structures. All these algorithms are included in the Hybrid Delocalized Internal Coordinate Optimiser (HDLCOpt)³⁹ module of Chemshell. All the pictures of molecules were generated with the VMD⁴³ and CHIMERA¹⁷ programs.

3 Results and discussion

3.1 Molecular dynamics simulations

As explained above, the first MD simulation of the Gly526Ser COX-2/AA Michaelis complex was carried out over 100 ns starting from the structure resulting from the setup. The evolution of the distances between the C_{13} pro-*S* hydrogen or the C_{13} carbon atom and the hydrogen-acceptor oxygen of the Tyr385 radical is displayed in Fig. 1 (for greater clarity, see the separated evolution of both distances in Fig. S2 and S3†). The distributions of both distances practically match throughout the simulation. The distances oscillate between about 5 \AA and 7

Table 1 Initial O– C_{11} distances, potential energy barriers, type of oxygen addition, and stereochemistry at C_{11} for the six reaction paths corresponding to the addition of the oxygen molecule to C_{11}

Reaction path	Initial distance O– C_{11} (Å)	ΔE (kcal mol ⁻¹)	O ₂ attack	Stereochemistry at C_{11}
I	3.18	7.7	Suprafacial	R
II	3.43	8.4	Suprafacial	R
III	3.12	8.6	Suprafacial	R
IV	4.04	11.2	Suprafacial	R
V	3.70	7.3	Antarafacial	S
VI	3.84	7.1	Antarafacial	S



Å most of the time for the first 50 ns, but, after a sudden jump, both remain between about 7 Å and 9 Å for the last 50 ns.

A typical structure corresponding to the second half of the MD simulation is pictured in Fig. 2. It can be seen that AA is forced to undergo a major repositioning as a consequence of the Gly526Ser mutation, moving from the “L-shaped” binding conformation that it adopts in the wild-type COX-2³ to a conformation where the chains corresponding to the AA ω-end and the AA carboxylate-end become roughly parallel. This motion causes the C₁₃ pro-S hydrogen to be too far from the hydrogen-acceptor oxygen of the Tyr385 radical for the abstraction of the first step of the all-radical mechanism to occur.

This rather unexpected behavior of AA inside the Gly526Ser mutant could not explain the experimental results by Brash and co-workers.¹⁶ Thus, we checked if the problem lay in the fact that we generated the setup of the mutant keeping the substrate AA within it. That is, we had not thus far allowed a free relaxation of the mutant enzyme in the absence of AA. Then, we eliminated AA from the setup (see Section 2.1), we repeated the protocol previous to the production stage as described in Section 2.3, and we ran a 20 ns MD simulation of the Gly526Ser COX-2 mutated enzyme. During these 20 ns, Ser526 rotates in order that the hydrogen of its OH group forms a hydrogen bond with the oxygen atom of the backbone of Met522 (this hydrogen bond is not possible with Gly526 in wild-type COX-2). This position is mostly maintained during this MD simulation (see Fig. S4†). As a consequence, the two hydrogen atoms of the C_β of Ser530 point towards the hydrophobic groove where the AA ω-end will finally lie.

Next, we re-introduced AA into the cavity of the mutant. To this aim, we eliminated the water molecules from the setup (see Section 2.1) and from the last structure of the previous 20 ns MD simulation, and we overlaid the enzyme residues of both structures. Then, we re-solvated the system, as explained in Section

Table 2 Potential energy barriers, and stereochemistry at C₁₁ and C₉ for the six reaction paths corresponding to the 9,11-cyclization leading to a C₈-radical cyclic endoperoxide

Reaction path	ΔE (kcal mol ⁻¹)	Stereochemistry at C ₁₁	Stereochemistry at C ₉
I	8.0	R	S
II	7.3	R	S
III	7.7	R	S
IV	8.1	R	S
V	9.9	S	R
VI	10.7	S	R

2.1, and we repeated the protocol described in Section 2.3 to run another 100 ns MD simulation of the Gly526Ser COX-2/AA Michaelis complex. The evolution of the distances between the C₁₃ pro-S hydrogen or the C₁₃ carbon atom and the hydrogen-acceptor oxygen of the Tyr385 radical (see Fig. 3) shows that most of the structures are now ready for the abstraction in the first step of the all-radical mechanism, especially for the first 90 ns, when the distances C₁₃ pro-S hydrogen–O(Tyr385) and C₁₃–O(Tyr385) are 3.4 ± 0.8 Å and 3.8 ± 0.8 Å, respectively.

In order to choose a snapshot representative of the ensemble of structures generated along this last MD simulation of the Gly526Ser COX-2/AA Michaelis complex, we picked one structure each 10 ps and filtered the structures by imposing the conditions $r(\text{C}_{13} \text{ pro-S H-O}(\text{Tyr385})) \leq 3$ Å and $r(\text{C}_{13} \text{ pro-S H-O}(\text{Tyr385})) < r(\text{C}_{13}\text{-O}(\text{Tyr385}))$. So, we obtained 3049 snapshots, which we clustered using a root mean square deviation (RMSD) of 1.3 Å for the heavy atoms of AA. The three most populated clusters included 1737, 1000 and 305 structures, respectively. Next, we determined the average position of the heavy atoms of AA over all the structures belonging to the most populated cluster, and we found the snapshot of that cluster with the smallest AA heavy atoms RMSD with respect to that average position. This snapshot, the so-called centroid snapshot for the

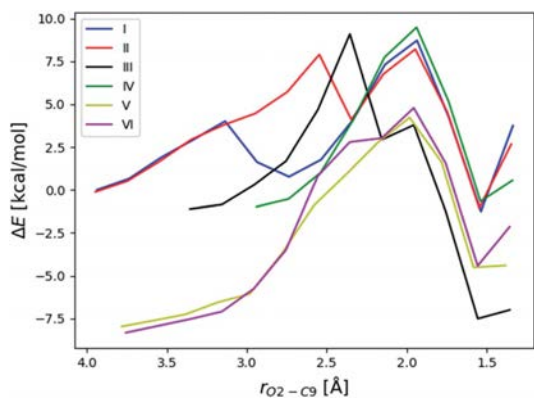


Fig. 7 Potential energy profiles corresponding to the 9,11-cyclization leading to a C₈-radical cyclic endoperoxide. O₂ stands for the oxygen atom of the oxygen molecule that is free and can attack C₉. The potential energy of the initial structure of reaction path I is taken as the origin of energies.

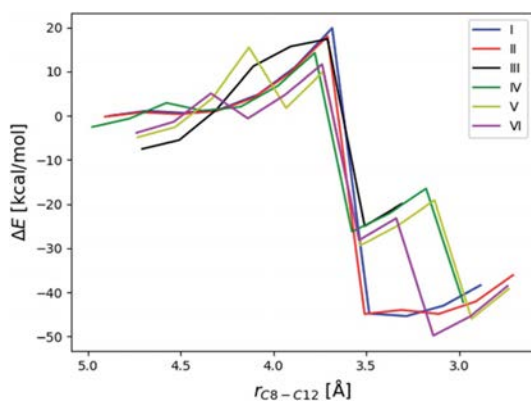


Fig. 8 Potential energy profiles as a function of the C₈–C₁₂ distance taken as the reaction coordinate. The potential energy of the initial structure of reaction path I is taken as the origin of energies.



most populated cluster, is pictured in Fig. 4. This structure has no similarities with the one shown in Fig. 2 in the case of the unrelaxed mutant enzyme. Now the “L-shaped” productive binding configuration of AA, as observed in the above-mentioned COX-2 crystal structure,³ has been recovered, with the AA ω -end extending along the hydrophobic groove above Ser530, and the C₁₃ carbon atom and the C₁₃ pro-S hydrogen atom of AA located below and near the phenolic oxygen of Tyr385. A comparison between the structure corresponding to snapshot 1 extracted from the MD simulation of the COX-2/AA Michaelis complex (see ref. 13) and the centroid snapshot of the most populated cluster of the last MD simulation of the Gly526Ser COX-2/AA Michaelis complex (Fig. 4) is pictured in

Fig. S5.† In addition, the distances between side chain carbon atoms of selected residues of that snapshot 1 (COX-2/AA) or that centroid snapshot (Gly526Ser COX-2/AA) and selected carbon atoms of AA bound in the corresponding active site are shown in Table S1.†

The centroids of the second and third most populated clusters were also determined. They are compared with the centroid of the most populated cluster in Fig. S6.† An “L-shaped” binding configuration of AA is obtained in the three cases.

In order to check if the 100 ns MD simulation shown in Fig. 3 is actually representative of the configurational space visited by an equilibrated Gly526Ser COX-2/AA Michaelis complex, we carried out two additional MD simulations. In the first, we

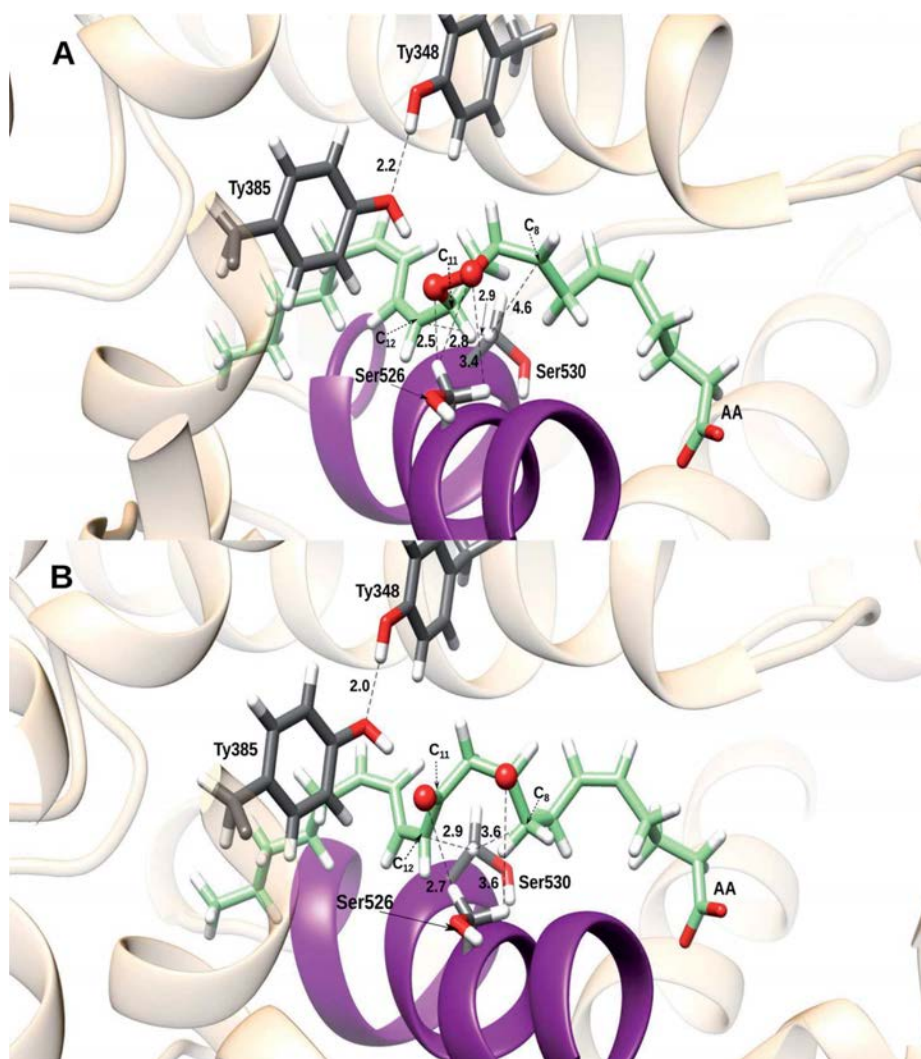


Fig. 9 Cyclic endoperoxide corresponding to reaction path II as a function of the C₈–C₁₂ distance at a point before the hydrogen transfer and the O–O cleavage (A), and at a point after that (B). Distances are given in Å.



lengthened this MD simulation for an additional 150 ns (see Fig. S7†). In the second, we selected at random one of the structures of the 20 ns MD simulation of the Gly526Ser COX-2 mutated enzyme, and after re-introducing AA into the cavity of the mutant as explained above, we generated a 100 ns MD simulation of the Gly526Ser COX-2/AA Michaelis complex (see Fig. S8†). This new MD simulation is equivalent to the one shown in Fig. 3, but starting from a different structure and different initial velocities. Comparison of Fig. 3 and S7, S8† confirms that, except for some local deviations, the Gly526Ser COX-2/AA Michaelis complex populates a region of the configurational space where most of the structures are ready for the C₁₃ pro-*S* hydrogen abstraction by O(Tyr385) in the first step of the all-radical mechanism.

3.2 QM/MM calculations

Now we used QM/MM calculations to determine if the Gly526Ser mutant of COX-2 is capable of driving the centroid snapshot of AA throughout the all-radical mechanism. Firstly, we built the potential energy profile of the C₁₃ pro-*S* hydrogen abstraction by the tyrosyl radical (step 1) as a function of the reaction coordinate. In this case, the reaction coordinate was taken as the difference between the distances corresponding to the breaking bond (C₁₃-pro-*S* hydrogen) and the forming bond (pro-*S* hydrogen-O(Tyr385)). The energy profile was calculated both forward and backward to avoid hysteresis (see Fig. 5). Once the reactants, transition state structure, and products had been located, the potential energy barrier turned out to be 24.8 kcal mol⁻¹. The values of the distances corresponding to the three atoms that directly participate in the breaking/forming bonds are given in Table S2† for each structure. As expected for a hydrogen transfer, the hydrogen donor and acceptor atoms approach each other to make the hydrogen transfer easier. After the transfer, both atoms move away. The transition state structure appears in the region with the closest distance (see Fig. S9†).

The first step produces a planar delocalized C₁₁-C₁₅ pentadienyl radical AA. In the second step the addition of the oxygen molecule to C₁₁ can be antarafacial (with the face of the C₁₁-C₁₅ pentadienyl system opposite to the tyrosyl radical), giving an 11*R* stereochemistry, or suprafacial (on the same side as the tyrosyl radical), leading to an 11*S* stereochemistry. We chose different possible starting positions of the oxygen molecule for the attack to C₁₁, as we had already done in previous work.¹³ That C₁₁ atom was chosen as the origin of coordinates, and the oxygen molecules, when possible, were placed around it along the *x*, *y* and *z* Cartesian axes, along the bisector axes contained in the *xy*, *xz* and *yz* planes, or near them. In all, 53 initial oxygen molecules were set close to C₁₁, at distances of 2.5, 3, and 3.5 Å, corresponding to 9, 18, and 26 O₂ molecules, respectively. Fifty-three QM/MM single point energy calculations were carried out for each one. Then, the structures with the highest energies were discarded and the most stable structures were optimized. The optimized structures were taken as starting points to build the potential energy profiles for the oxygen addition to C₁₁, the distance O (the one closest to C₁₁)-C₁₁ being the reaction

coordinate. Only six different reaction paths leading to the peroxy radical in C₁₁ were obtained. In Fig. 6 we display these reactions paths (labeled I to VI) according to the structure (that is, the initial optimized position of the oxygen molecule) from which the reaction path starts. The corresponding potential energy barriers and geometrical information are given in Table 1. The suprafacial and antarafacial oxygen additions lead to peroxides with *R* and *S* configurations at C₁₁, respectively. This scenario is the opposite to the case of wild-type COX-2, where the suprafacial and antarafacial oxygen attacks produce the *S* and *R* configurations at C₁₁, respectively.¹³ On the other hand, the potential energy barriers (7.1 to 11.2 kcal mol⁻¹) turn out to be small in comparison with that for hydrogen abstraction (24.8 kcal mol⁻¹).

The third step consists of the 9,11-cyclization, leading to a C₈-radical cyclic endoperoxide. In Fig. 7 we have plotted the potential energy profiles obtained as a function of the reaction coordinate O-C₉ for the six reaction paths. Some of the profiles

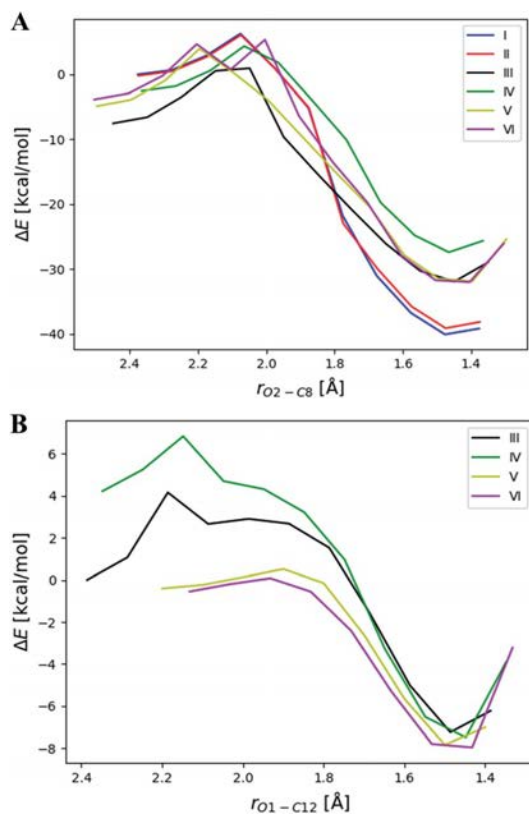


Fig. 10 Potential energy profiles corresponding to the formation of (A) the 8,9- and 11,12-epoxides in a concerted way for reaction paths I and II, but just the 8,9-epoxide for reaction paths III-VI, as a function of the O2 (bonded to C₉)-C₈ distance taken as the reaction coordinate; and (B) the 11,12-epoxide for reaction paths III to VI, as a function of the O1 (bonded to C₁₁)-C₁₂ distance taken as the reaction coordinate.



involve two potential energy maxima. In these cases, in the first stage the free oxygen of the oxygen molecule added to C_{11} has to rotate around the C_{11} -O bond in order to approach C_9 (first maximum) and then the 9,11-cyclization occurs (second maximum). The potential energy barriers corresponding to the higher energy transition state structures for each reaction path are shown in Table 2, along with stereochemical information. The four paths corresponding to an *R* configuration at C_{11} involve barriers 2–3 kcal mol⁻¹ lower than the two paths with an *S* configuration at C_{11} . Most interestingly, we have obtained (9*S*,

11*R*) and (9*R*, 11*S*) cyclic endoperoxides, but not (9*R*, 11*R*). This fact will have important consequences for the following mechanistic step.

For the fourth step we chose the distance C_8 - C_{12} to define the reaction coordinate for the 8,12-cyclization. When that distance was shortened the O-O bond of the cyclic endoperoxide was broken in all cases. Instead of the formation of the cyclopentane ring, a hydrogen transfer from C_{11} to C_8 followed by the breakage of the O-O bond occurred, leading to the formation of a ketone group in C_{11} and a radical centered at the

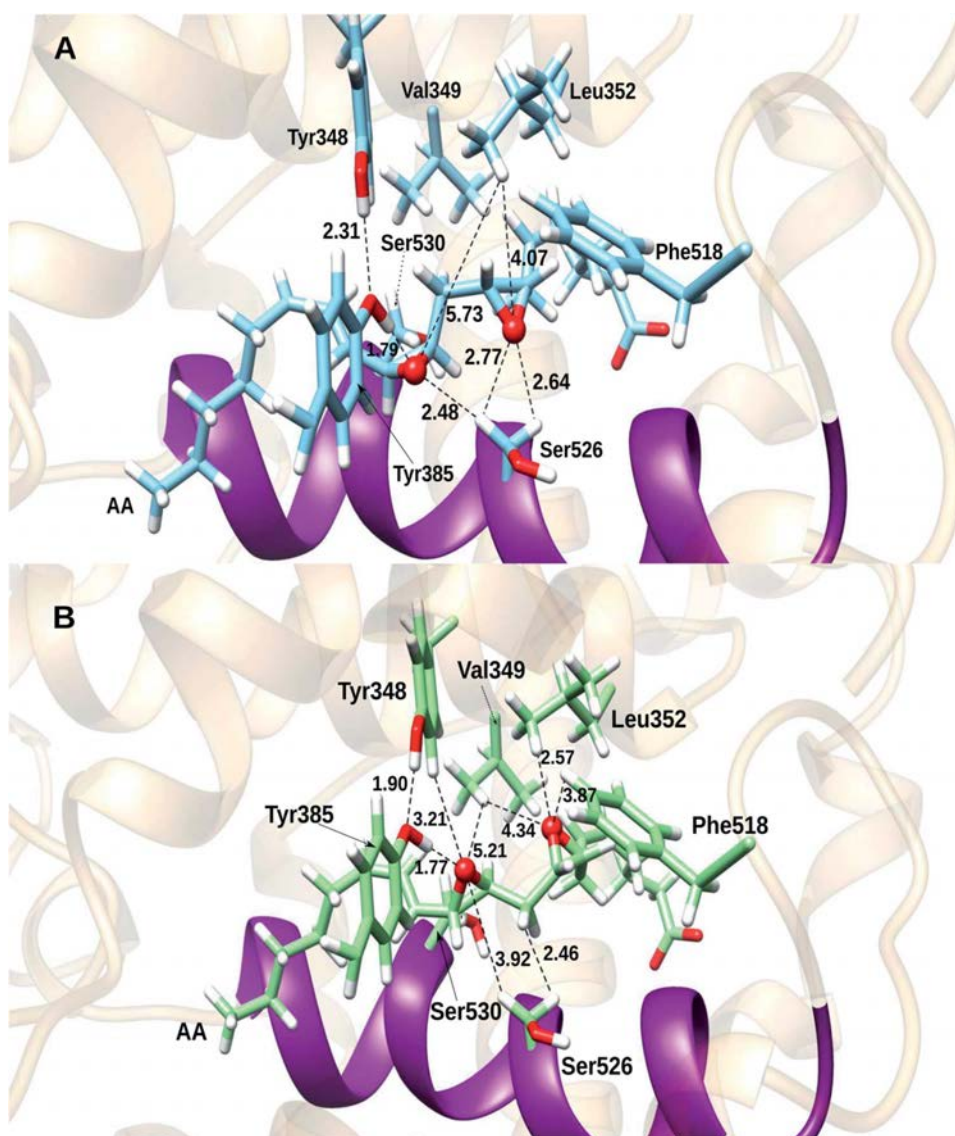


Fig. 11 Structure of the 8,9- and 11,12-epoxides corresponding to (A) reaction path I; and (B) reaction path III. Distances are given in Å.



other oxygen atom (the one bonded to C₉). The corresponding potential energy profiles are displayed in Fig. 8. This process turns out to be very exothermic, and the hydrogen transfer and the O–O cleavage can take place in a concerted way or in two stages, depending on the reaction path. The potential energy barriers range from 15.5 kcal mol⁻¹ to 25 kcal mol⁻¹.

Our calculations confirm the experimental finding by Brash and co-workers,¹⁶ who found that the 8,12-cyclization does not occur in the Gly526Ser mutant COX-2. We know that the cyclopentane ring closure only occurs with a (9*R*, 11*R*) configuration,^{13,16} but this is just the stereochemical configuration that cannot be reached after the third mechanistic step in the mutant, as mentioned above. The reason for that can be understood by analyzing Fig. 9, where, for the sake of example, we have pictured the cyclic endoperoxide corresponding to reaction path II as a function of the C₈–C₁₂ distance at a point before the hydrogen transfer and the O–O cleavage (Fig. 9A), and at a point after that (Fig. 9B). As commented in Section 3.1, in the Gly526Ser mutant COX-2 the hydrogen of the Ser526 OH group forms a hydrogen bond (see Fig. S5[†]) with the oxygen atom of the Met522 backbone (a hydrogen bond that cannot exist with Gly526 in wild-type COX-2). As a consequence, the two hydrogen atoms of the C_β Ser530 point towards the hydrophobic groove where the AA ω-end lies. This position makes the helix D containing residues from 521 to 535 quite rigid and forces Ser530 to adopt the position shown in Fig. 9A (both Ser residues belong to that helix). As a result, the hydrogen at C₉ cannot be at the same side as the hydrogen at C₁₁ (this is equivalent to saying that the (9*R*, 11*R*) configuration cannot be reached), and the 8,12-cyclization cannot happen. In Fig. 9B the hydrogen transfer from C₁₁ to C₈ and the breakage of the O–O bond have already taken place.

At this point it is clear that the Gly526Ser mutation hinders the formation of prostaglandins because the 8,12-cyclization does not occur, and the cyclic endoperoxide breaks. Nevertheless, this breakage does not experimentally take place in the way described above according to Fig. 8 and 9B. In effect, as already found by Brash and co-workers,¹⁶ the homolytic cleavage of the O–O bond actually leads to the formation of 8,9-11,12-diepoxy derivatives of the arachidonic acid. Taking the distance O (bonded to C₉)–C₈ as the reaction coordinate, the 8,9- and 11,12-epoxides are formed in a concerted way for reaction paths I and II (see Fig. 10A), but just the 8,9-epoxide for reaction paths III–VI (see also Fig. 10A). The 11,12-epoxide for these last reaction paths is formed next when the distance O (bonded to C₁₁)–C₁₂ is chosen to define the reaction coordinate (see Fig. 10B). Anyway, the product contains an allyl radical delocalized from C₁₃ to C₁₅. In all cases the potential energy barriers for the formation of the epoxides are clearly lower than the ones corresponding to the above-discussed O–O cleavage involving a hydrogen transfer from C₁₁ to C₈, so explaining the experimental formation of the 8,9-11,12-diepoxy derivatives.

Both epoxides are stabilized by interactions with several residues like Ser526. The 11,12-epoxide is especially stabilized by formation of a hydrogen bond with Tyr385, which, in turn, is hydrogen-bonded to Tyr348 (see Fig. 11). As a matter of fact, the two early maxima that appear for the formation of the 11,12-

epoxide in the case of reaction paths III and IV (Fig. 10B) just correspond to the previous reorganization of Tyr385 in order to be able to interact with the epoxide to be formed. It is interesting to note that, conversely, Tyr385 does not interact with either of the two oxygen atoms of the O–O bridge after the 8,12-cyclization to give a bicyclo endoperoxide which occurs in wild-type COX-2 (see Fig. S10,[†] derived from the calculations in our previous work¹³ for the sake of comparison).

4. Conclusions

The biosynthesis of prostaglandins from arachidonic acid catalyzed by cyclooxygenase-2 is the result of a complex mechanism where every residue of the cyclooxygenase active site plays its role to achieve exceptional stereochemical and regiochemical control of the outcome. Unraveling these roles is not an easy task. Particularly remarkable is the case of the Gly526 residue. Brash and co-workers¹⁶ have shown that the Gly526Ser mutant of human COX-2 is unable to produce the 8,12-cyclization required for the formation of prostaglandin. Instead, they found novel products that were identified as 8,9-11,12-diepoxy-13*R*- (or 15*R*)-hydroperoxy derivatives of arachidonic acid. In this work we have combined molecular dynamics simulations and QM/MM calculations to shed light on the molecular details of the effects of such a mutation.

Our results show that inside the Gly526Ser COX-2 binding pocket, AA adopts the same “L-shaped” productive binding configuration as the one observed in the COX-2 crystal structure,³ with the AA ω-end extending along the hydrophobic groove above Ser530, and the C₁₃ carbon atom and the C₁₃ pro-S hydrogen atom of AA located below and near the phenolic oxygen of Tyr385. Then, the first three reaction steps of the all-radical mechanism^{7,13} can take place, leading to C₈-radical cyclic endoperoxides, in both wild-type COX-2 and Gly526Ser COX-2. The difference between the two cases lies in the fact that only COX-2, but not the mutant, is able to produce cyclic endoperoxides with a (9*R*, 11*R*) configuration, the stereochemistry that is required to make the 8,12-cyclization possible. This is a consequence of the fact that in the Gly526Ser mutant COX-2, the hydrogen of the Ser526 OH group forms a hydrogen bond with the oxygen atom of the Met522 backbone (a hydrogen bond that cannot exist with Gly526 in wild-type COX-2). Then, the two hydrogen atoms of C_β Ser530 point towards the hydrophobic groove where the AA ω-end is located, in a position that hinders the hydrogen at C₉ from being at the same side as the hydrogen at C₁₁ (this is equivalent to saying that the (9*R*, 11*R*) configuration cannot be reached). Consequently, the 8,12-cyclization towards the formation of prostaglandin cannot take place in Gly526Ser COX-2. In fact, all attempts to force the shortening of the C₈–C₁₂ distance provoke hydrogen transfer from C₁₁ to C₈ followed by the breakage of the O–O bond of the cyclic endoperoxide. Anyway, the homolytic cleavage of the O–O bond leading to the formation of 8,9-11,12-diepoxy derivatives of the arachidonic acid turns out to occur faster, thus explaining the experimental findings by Brash and co-workers.¹⁶ We hope that this work can contribute to better molecular comprehension of



the catalytic mechanism of COX-2, one of the main enzymes responsible for inflammation processes in humans.

Conflicts of interest

There are no conflicts to declare.

Acknowledgements

This work was supported by the Spanish “Ministerio de Ciencia, Innovación y Universidades” (project CTQ2017-83745-P).

References

- M. Murakami, *Exp. Anim.*, 2011, **60**, 7–20.
- C. Schneider, D. A. Pratt, N. A. Porter and A. R. Brash, *Chem. Biol.*, 2007, **14**, 473–488.
- A. J. Vecchio, D. M. Simmons and M. G. Malkowski, *J. Biol. Chem.*, 2010, **285**, 22152–22163.
- C. Yuan, C. J. Rieke, G. Rimon, B. A. Wingerd and W. L. Smith, *Proc. Natl. Acad. Sci. U. S. A.*, 2006, **103**, 6142–6147.
- W. L. Smith, D. L. DeWitt and R. M. Garavito, *Annu. Rev. Biochem.*, 2000, **69**, 145–182.
- B. J. Orlando, P. P. Borbat, E. R. Georgieva, J. H. Freed and M. G. Malkowski, *Biochemistry*, 2015, **54**, 7309–7312.
- M. Hamberg and B. Samuelsson, *J. Biol. Chem.*, 1967, **242**, 5336–5343.
- K. Marnett and L. J. Maddipati, ed. M. Grisham, J. Everse and K. Everse, *Prostaglandin H Synthase*, CRC Press, Florida, Unites States, Boca Raton, 1991, vol. 1, pp. 293–334.
- W. L. Smith and L. J. Marnett, *Biochim. Biophys. Acta*, 1991, **1083**, 1–17.
- C. Schneider, W. E. Boeglin, S. Lai, J. K. Cha and A. R. Brash, *Anal. Biochem.*, 2000, **284**, 125–135.
- L. J. Marnett, *Curr. Opin. Chem. Biol.*, 2000, **4**, 545–552.
- P. J. Silva, P. A. Fernandes and M. J. Ramos, *Theor. Chem. Acc.*, 2003, **110**, 345–351.
- A. Cebrián-Prats, À. González-Lafont and J. M. Lluch, *ACS Omega*, 2019, **4**, 2063–2074.
- S. W. Rowlinson, B. C. Crews, D. C. Goodwin, C. Schneider, J. K. Gierse and L. J. Marnett, *J. Biol. Chem.*, 2000, **275**, 6586–6591.
- C. Schneider, W. E. Boeglin, J. J. Prusakiewicz, S. W. Rowlinson, L. J. Marnett, N. Samel and A. R. Brash, *J. Biol. Chem.*, 2002, **277**, 478–485.
- C. Schneider, W. E. Boeglin and A. R. Brash, *J. Biol. Chem.*, 2004, **279**, 4404–4414.
- E. F. Pettersen, T. D. Goddard, C. C. Huang, G. S. Couch, D. M. Greenblatt, E. C. Meng and T. E. Ferrin, *J. Comput. Chem.*, 2004, **25**, 1605–1612.
- J. A. Maier, C. Martinez, K. Kasavajhala, L. Wickstrom, K. E. Hauser and C. Simmerling, *J. Chem. Theory Comput.*, 2015, **11**, 3696–3713.
- D. A. Case, I. Y. Ben-Shalom, S. R. Brozell, D. S. Cerutti, T. E. Cheatham III, V. W. D. Cruzeiro, T. A. Darden, R. E. Duke, D. Ghoreishi, M. K. Gilson, H. Gohlke, A. W. Goetz, D. Greene, R. Harris, N. Homeyer, S. Izadi, A. Kovalenko, T. Kurtzman, T. S. Lee, S. LeGrand, P. Li, C. Lin, J. Liu, T. Luchko, R. Luo, D. J. Mermelstein, K. M. Merz, Y. Miao, G. Monard, C. Nguyen, H. Nguyen, I. Omelyan, A. Onufriev, F. Pan, R. Qi, D. R. Roe, A. Roitberg, C. Sagui, S. Schott-Verdugo, J. Shen, C. L. Simmerling, J. Smith, R. Salomon-Ferrer, J. Swails, R. C. Walker, J. Wang, H. Wei, R. M. Wolf, X. Wu, L. Xiao, D. M. York and P. A. Kollman, *AMBER 2018*, University of California, San Francisco, 2018.
- W. L. Jorgensen, J. Chandrasekhar, J. D. Madura, R. W. Impey and M. L. Klein, *J. Chem. Phys.*, 1983, **79**, 926–935.
- K. Shahrokh, A. Orendt, G. S. Yost and T. E. Cheatham, *J. Comput. Chem.*, 2012, **33**, 119–133.
- C. I. Bayly, P. Cieplak, W. Cornell and P. A. Kollman, *J. Phys. Chem.*, 1993, **97**, 10269–10280.
- J. Wang, R. M. Wolf, J. W. Caldwell, P. A. Kollman and D. A. Case, *J. Comput. Chem.*, 2004, **25**, 1157–1174.
- D. A. Case, V. Babin, J. T. Berryman, R. M. Betz, Q. Cai, D. S. Cerutti, T. E. Cheatham III, T. A. Darden, R. E. Duke, H. Gohlke, A. W. Goetz, S. Gusarov, N. Homeyer, P. Janowski, J. Kaus, I. Kolossváry, A. Kovalenko, T. S. Lee, S. LeGrand, T. Luchko, R. Luo, B. Madej, K. M. Merz, F. Paesani, D. R. Roe, A. Roitberg, C. Sagui, R. Salomon-Ferrer, G. Seabra, C. L. Simmerling, W. Smith, J. Swails, R. C. Walker, J. Wang, R. M. Wolf, X. Wu and P. A. Kollman, *AMBER 14*, University of California, San Francisco, 2014.
- P. Tosco, *J. Am. Chem. Soc.*, 2013, **135**, 10404–10410.
- C. Lee, W. Yang and R. G. Parr, *Phys. Rev. B: Condens. Matter Mater. Phys.*, 1988, **37**, 785–789.
- A. D. Becke, *J. Chem. Phys.*, 1993, **98**, 5648–5652.
- P. C. Hariharan and J. A. Pople, *Theor. Chim. Acta*, 1973, **28**, 213–222.
- M. M. Francl, W. J. Pietro, W. J. Hehre, J. S. Binkley, M. S. Gordon, D. J. DeFrees and J. A. Pople, *J. Chem. Phys.*, 1982, **77**, 3654–3665.
- M. J. Frisch, G. W. Trucks, H. B. Schlegel, G. E. Scuseria, M. A. Robb, J. R. Cheeseman, G. Scalmani, V. Barone, B. Mennucci, G. A. Petersson, H. Nakatsuji, M. Caricato, X. Li, H. P. Hratchian, A. F. Izmaylov, J. Bloino, G. Zheng, J. L. Sonnenberg, M. Hada, M. Ehara, K. Toyota, R. Fukuda, J. Hasegawa, M. Ishida, T. Nakajima, Y. Honda, O. Kitao, H. Nakai, T. Vreven, J. A. Montgomery, J. E. Peralta, F. Ogliaro, M. Bearpark, J. J. Heyd, E. Brothers, K. N. Kudin, V. N. Staroverov, R. Kobayashi, J. Normand, K. Raghavachari, A. Rendell, J. C. Burant, S. S. Iyengar, J. Tomasi, M. Cossi, N. Rega, J. M. Millam, M. Klene, J. E. Knox, J. B. Cross, V. Bakken, C. Adamo, J. Jaramillo, R. Gomperts, R. E. Stratmann, O. Yazyev, A. J. Austin, R. Cammi, C. Pomelli, J. W. Ochterski, R. L. Martin, K. Morokuma, V. G. Zakrzewski, G. A. Voth, P. Salvador, J. J. Dannenberg, S. Dapprich, A. D. Daniels, Farkas, J. B. Foresman, J. V. Ortiz, J. Cioslowski, D. J. Fox, M. J. Frisch, G. W. Trucks, H. B. Schlegel, G. E. Scuseria, M. A. Robb, J. R. Cheeseman, G. Scalmani, V. Barone,



- B. Mennucci, G. A. Petersson, H. Nakatsuji, M. Caricato, X. Li, H. P. Hratchian, A. F. Izmaylov, J. Bloino, G. Zheng, J. L. Sonnenberg, M. Had and D. J. Fox, Gaussian, Inc., Wallingford CT, 2009.
- 31 M. Deserno and C. Holm, *J. Chem. Phys.*, 1998, **109**, 7678–7693.
- 32 H. Lei, N. A. Baker and X. Li, *Proc. Natl. Acad. Sci. U. S. A.*, 2016, **113**, 14183–14188.
- 33 H. J. C. Berendsen, J. P. M. Postma, W. F. Van Gunsteren, A. Dinola and J. R. Haak, *J. Chem. Phys.*, 1984, **81**, 3684–3690.
- 34 J. P. Ryckaert, G. Ciccotti and H. J. C. Berendsen, *J. Comput. Phys.*, 1977, **23**, 327–341.
- 35 S. Le Grand, A. W. Götz and R. C. Walker, *Comput. Phys. Commun.*, 2013, **184**, 374–380.
- 36 R. Salomon-Ferrer, A. W. Götz, D. Poole, S. Le Grand and R. C. Walker, *J. Chem. Theory Comput.*, 2013, **9**, 3878–3888.
- 37 S. Metz, J. Kästner, A. A. Sokol, T. W. Keal and P. Sherwood, *Wiley Interdiscip. Rev.: Comput. Mol. Sci.*, 2014, **4**, 101–110.
- 38 P. Sherwood, A. H. de Vries, M. F. Guest, G. Schreckenbach, C. R. A. Catlow, S. A. French, A. A. Sokol, S. T. Bromley, W. Thiel, A. J. Turner, S. Billeter, F. Terstegen, S. Thiel, J. Kendrick, S. C. Rogers, J. Casci, M. Watson, F. King, E. Karlsen, M. Sjøvoll, A. Fahmi, A. Schäfer and C. Lennartz, *J. Mol. Struct.: THEOCHEM*, 2003, **632**, 1–28.
- 39 W. Smith and T. R. R. Forester, *J. Mol. Graphics*, 1996, **14**, 136–141.
- 40 D. Bakowies and W. Thiel, *J. Phys. Chem.*, 1996, **100**, 10580–10594.
- 41 H. M. Senn and W. Thiel, *Angew. Chem., Int. Ed.*, 2009, **48**, 1198–1229.
- 42 D. C. Liu and J. Nocedal, *Math. Program.*, 1989, **45**, 503–528.
- 43 W. Humphrey, A. Dalke and K. Schulten, *J. Mol. Graphics*, 1996, **14**, 33–38.



Electronic Supplementary Information

Unraveling how the Gly526Ser mutation arrests prostaglandin formation from arachidonic acid catalyzed by cyclooxygenase-2: A combined molecular dynamics and QM/MM study.

Adrián Suñer-Rubio,[†] Anna Cebrián-Prats,[†] Àngels González-Lafont^{†,‡} and José M. Lluch^{†,‡,*}

[†]Departament de Química and [‡]Institut de Biotecnologia i de Biomedicina (IBB),
Universitat Autònoma de Barcelona, 08193 Bellaterra, Barcelona, Spain

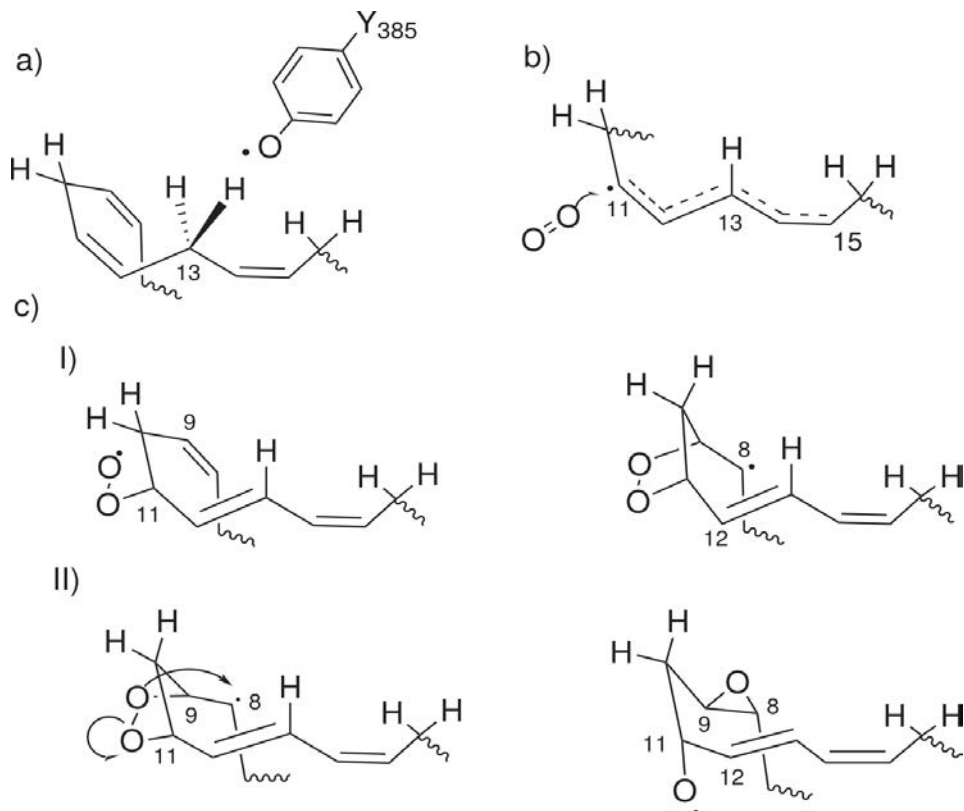


Figure S1. QM region of each particular reaction step. a) 38 atoms for the H-abstraction. b) 18 atoms for the O_2 addition at C_{11} . c) 25 atoms for: I) both cyclizations, the formation of the endoperoxide bridge and the cyclopentane ring and II) both epoxidations, the formation of 8,9-epoxide and 11,12-epoxide.

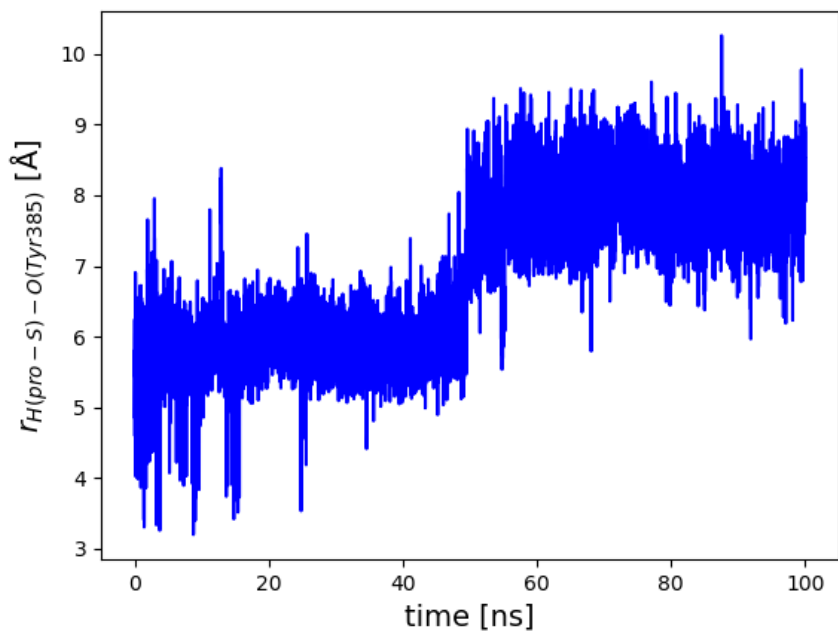


Figure S2. Evolution of the C₁₃ pro-S hydrogen – O(Tyr385) distance along the 100 ns of the first MD simulation of the Gly526Ser COX-2/AA Michaelis complex.

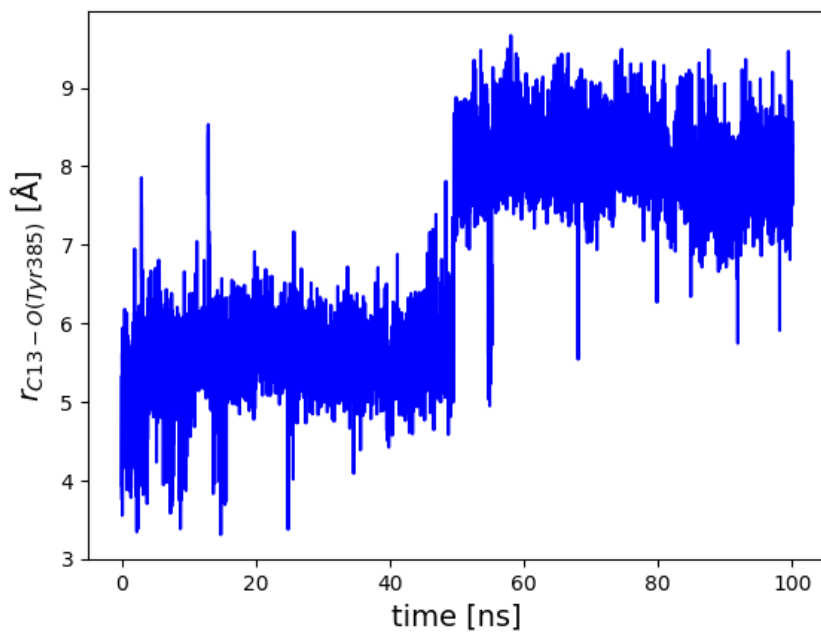


Figure S3. Evolution of the $C_{13} - O(\text{Tyr385})$ distance along the 100 ns of the first MD simulation of the Gly526Ser COX-2/AA Michaelis complex.

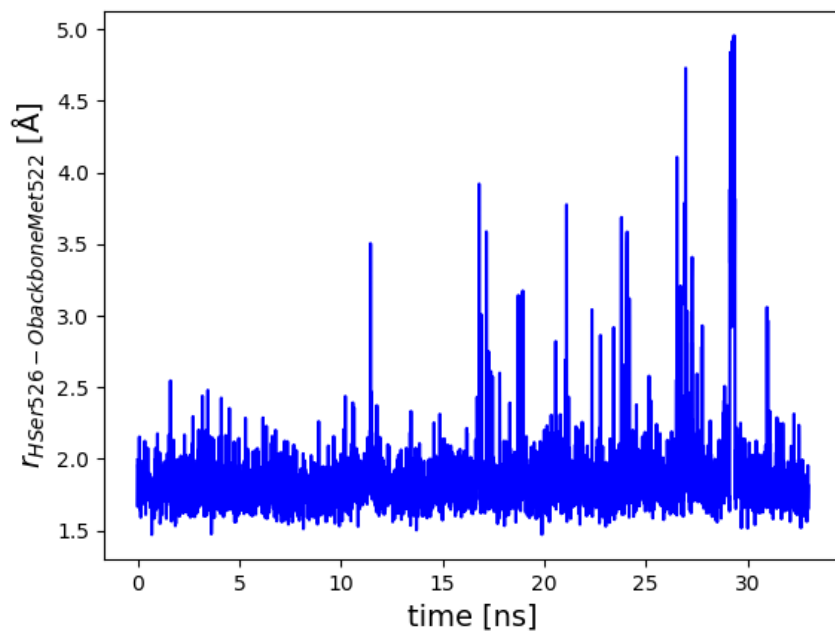


Figure S4. Distance between the hydrogen of the Ser526 OH group and the oxygen atom of the Met522 backbone along the 10 ns (equilibration) + 20 ns (production) MD simulation of the Gly526Ser COX-2 mutant enzyme without AA.

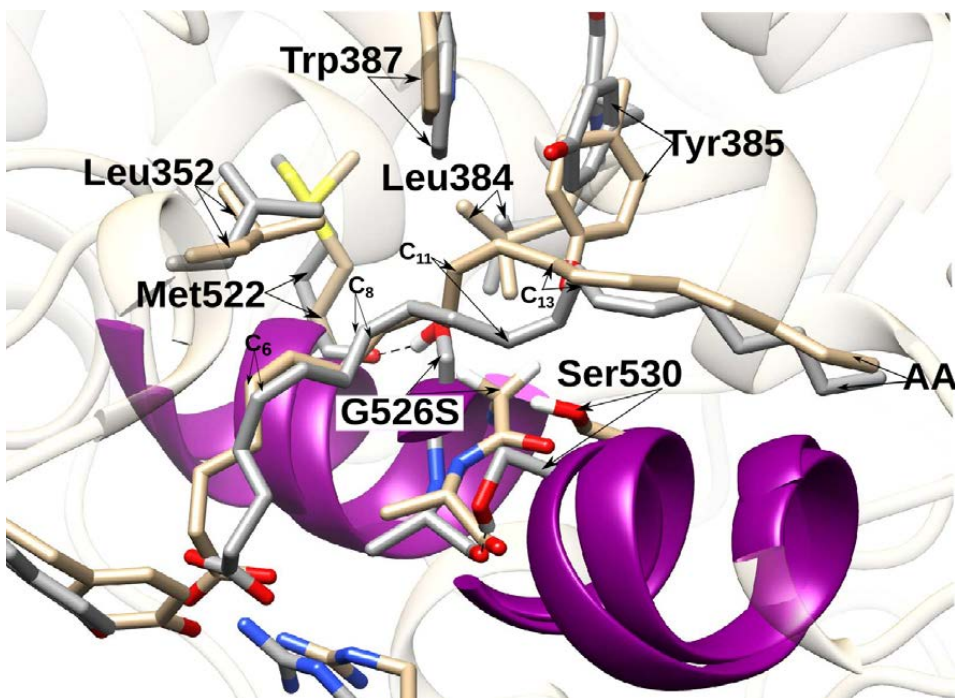


Figure S5. Comparison between the structure (in tan) corresponding to snapshot 1 extracted from the MD simulation of the COX-2/AA Michaelis complex (see reference 13) and the centroid snapshot (in grey) of the most populated cluster of the last MD simulation of the Gly526Ser COX-2/AA Michaelis complex shown in Figure 4. G526S stands for Gly or Ser for COX-2/AA or Gly526Ser COX-2/AA, respectively.

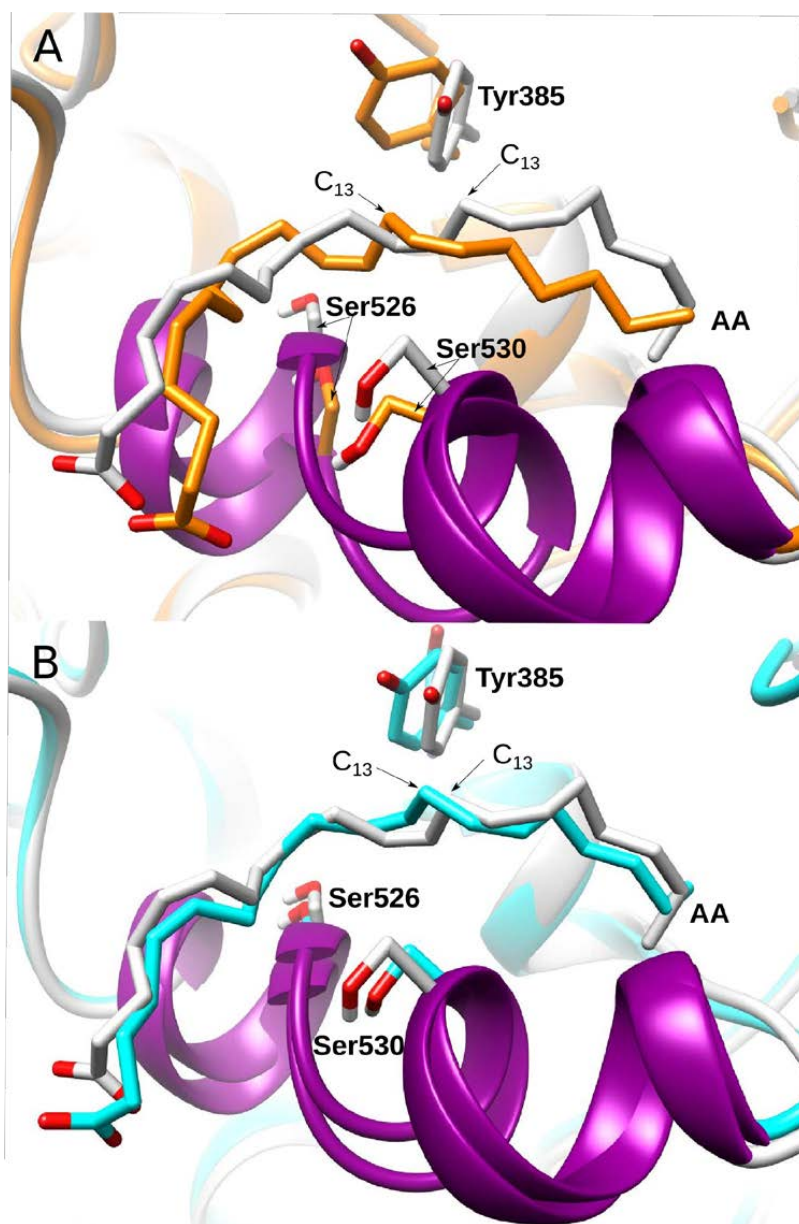


Figure S6. Comparison between the centroid of the most populated cluster (in grey) and A) the centroid of the second most populated cluster (in orange); B) the centroid of the third most populated cluster (in cyan).

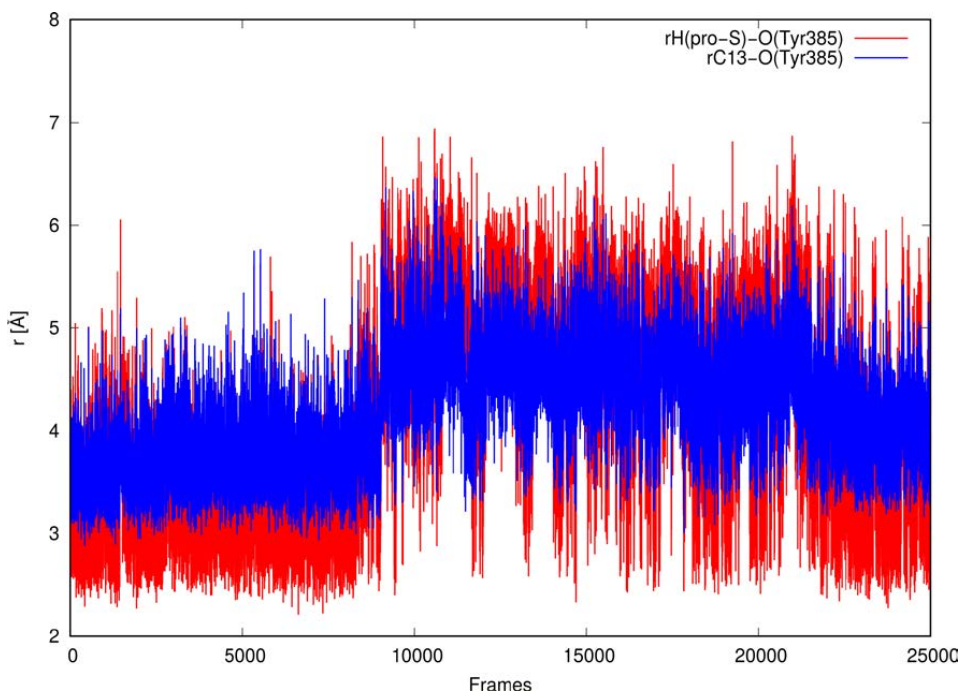


Figure S7. Evolution of the distances C_{13} pro-S hydrogen – O(Tyr385) (red line) and C_{13} – O(Tyr385) (blue line) along 250 ns of the last MD simulation of the Gly526Ser COX-2/AA Michaelis complex. The first 100 ns have already been pictured in Figure 3. A frame has been taken each 10 ps.

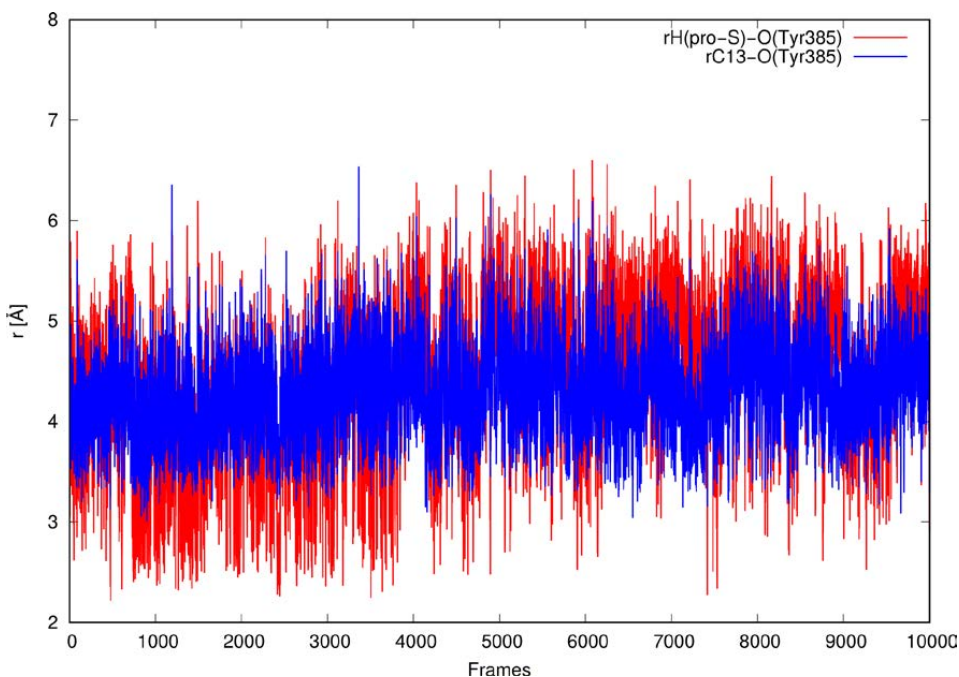


Figure S8. Evolution of the distances C_{13} pro-S hydrogen – O(Tyr385) (red line) and C_{13} – O(Tyr385) (blue line) along 100 ns MD simulation of the Gly526Ser COX-2/AA Michaelis complex. To carry out this MD simulation, we have selected at random one of the structures of the 20 ns MD simulation of the Gly526Ser COX-2 mutated enzyme, and after re-introducing AA in the cavity of the mutant as explained in section 3.1 of the main text, we have run the simulation. This new MD simulation is equivalent to the one shown in Figure 3, but starting from a different structure and different initial velocities. A frame has been taken each 10 ps.

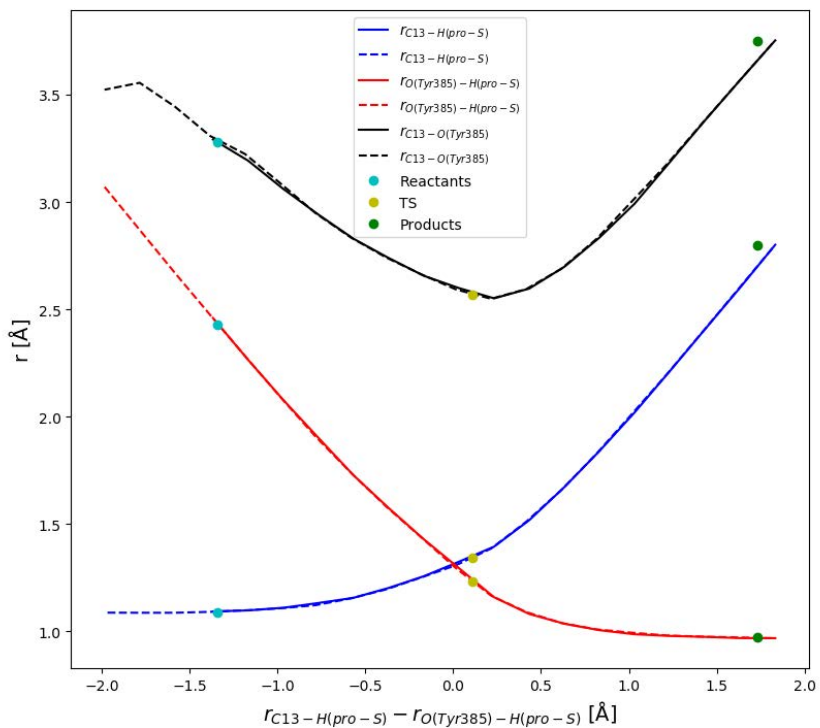


Figure S9. Evolution of the main distances along the C₁₃ pro-S hydrogen abstraction by the tyrosyl radical. The points indicate the location of the stationary points. The continuous and dashed lines correspond to the forward and backward potential energy profiles, respectively.

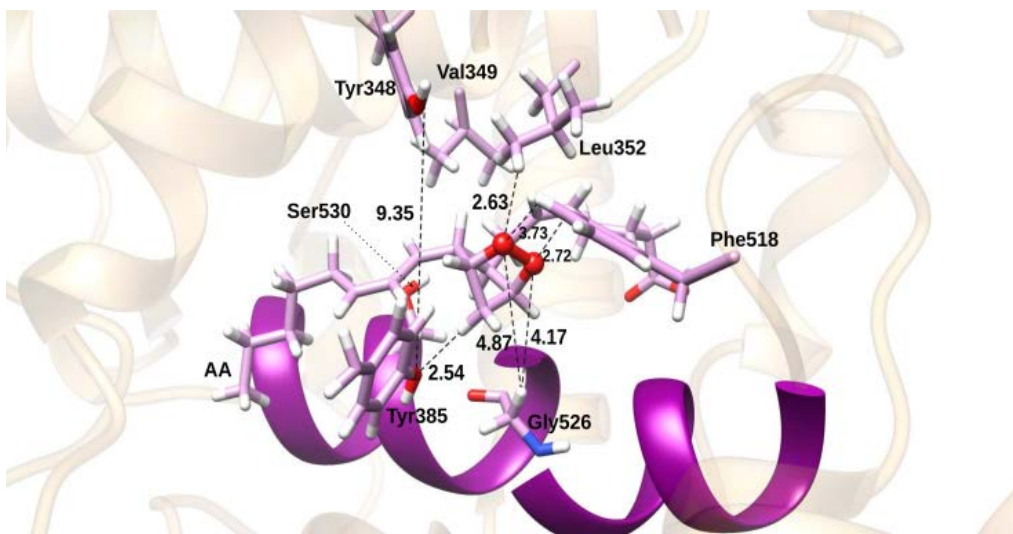


Figure S10. Structure obtained after the 8,12-cyclization to give a bicyclo endoperoxide that occurs in wild type COX-2.

Table S1. Distances (in Å) between side chain carbon atoms of selected residues of snapshot 1 extracted from the MD simulation of the COX-2/AA Michaelis complex (see reference 13) or the centroid snapshot of the most populated cluster of the last MD simulation of the Gly526Ser COX-2/AA Michaelis complex shown in Figure 4, and selected carbon atoms of arachidonic acid bound in the corresponding active site. G526S stands for Gly or Ser for COX-2/AA or Gly526Ser COX-2/AA, respectively.

Residue	C-atom	COX-2/AA				Gly526Ser COX-2/AA			
		C ₆	C ₈	C ₁₁	C ₁₃	C ₆	C ₈	C ₁₁	C ₁₃
G526S	C _A or	5.9	3.8	5.5	6.1	6.0	3.6	4.2	6.4
	C _B								
Ser530	C _B	7.7	6.4	5.1	4.1	5.4	5.5	3.6	5.0
Tyr385	C _Z ^a	7.8	5.4	4.3	3.7	8.7	7.0	5.2	3.7
Met522	C _G ^b	7.6	6.4	9.3	10.8	10.2	8.3	10.5	12.3
Trp387	CH ₂ ^c	7.2	5.8	4.5	5.6	7.3	5.2	5.6	5.7
	CZ ₂	7.1	5.5	5.0	6.2	7.8	5.5	6.1	6.5
Leu352	CD ₁ ^d	4.9	5.9	5.9	8.3	4.1	4.8	6.1	6.9
	CD ₂	4.3	4.7	3.6	5.9	5.3	5.8	8.2	8.9
Leu384	CD ₁ ^d	7.5	5.2	6.8	7.4	10.6	8.2	8.5	9.8
	CD ₂	7.6	5.4	6.8	7.7	9.8	7.3	7.4	8.2

^a C_Z is the 4'-carbon of the benzyl ring of Tyr.

^b C_G is the CH₂ carbon bonded to sulfur atom.

^c CH₂ and CZ₂ are carbons 5' and 4' of the indole side chain of Trp.

^d CD₁ and CD₂ are the terminal methyl carbons of the leucine side chain.

Table S2. Distances (Å) corresponding to the three atoms that directly participate in the breaking/forming bonds for the reactant, transition state structure and product ^a corresponding to the C₁₃ pro-S hydrogen abstraction by the tyrosyl radical.

d(C-H) _R	d(H-O) _R	d(C-O) _R	d(C-H) _{TS}	d(H-O) _{TS}	d(C-O) _{TS}	d(C-H) _P	d(H-O) _P	d(C-O) _P
1.09	2.43	3.28	1.34	1.23	2.57	2.78	0.97	3.74

^a C, H and O stand, respectively, for C₁₃, H_{pro-S}, and O of the Tyr385 radical

Article III

ACS Catal. 2020, 10, 138–153.

DOI: [10.1021/acscatal.9b04223](https://doi.org/10.1021/acscatal.9b04223)

